Design and Fabrication of Polymer Magnetic Actuators for Scanning

by

Olgaç Ergeneman

A Thesis Submitted to the
Graduate School of Engineering
in Partial Fulfillment of the Requirements for
the Degree of

Master of Science

in

Electrical and Computer Engineering

Koc University

October 2005

Koc University

Graduate School of Sciences and Engineering

This is to certify that I have examined this copy of a master's thesis by

Olgaç Ergeneman

and have found that it is complete and satisfactory in all respects,
and that any and all revisions required by the final
examining committee have been made.

Committee Members:

Hakan Urey, Ph. D. (Advisor)

Erdem Alaca, Ph. D.

Funda Yağcı, Ph. D.

Date: 24.10.2005

ABSTRACT

This thesis mainly deals with the design and development of resonant laser scanners with a simple and low-cost fabrication process using molded polymers and electroplated magnetic films. The polymer magnetic scanners described here are used in a prototype barcode reading system and the performance proved to be adequate for certain 1D and 2D imaging applications. Most important contributions of this work are (1) the development of a simple and low-cost fabrication process using polymers and electroplated magnetic materials, (2) the design and modeling of novel dynamic-actuation methods with magnetic materials for 1D and 2D laser scanning.

Two types of scanners were designed for this work: cantilever beam scanners and torsional scanners. Unlike micromachined scanners, the present process does not require clean room environment and photolithography steps. Polymers are molded or cut into desired shape and used as scanning mirrors. Different types of self-curing or UV-curing polymers are tested as structural material. Good results are obtained with UV-curing polymer, typically used for stereo-lithography, and the copper coated epoxy used in printed circuit boards (PCB). One side of the polymer is either coated with Aluminum (Al) or Al-coated Silicon mirror is attached to the scanner for high reflectivity and good mirror surface quality. Magnetism is introduced to the structural material in two different ways (1) mixing magnetic particles in powder form into the polymer, (2) electroplating permalloy ($Ni_{80}Fe_{20}$) magnetic film underneath the polymer. Resonant-mode dynamic actuation is obtained by applying a time-varying current to an external coil. For a given magnetic field, magnetic forces obtained with the electroplated scanners are higher than the forces obtained with the magnetic particles. Deposition of permalloy (80% nickel and 20% iron) magnetic thin films is performed in our plating facilities.

Another contribution of this work is in modeling and optimization of the magnetic actuation using electroplated thin films in both saturated and unsaturated modes of operation. This work focuses on small-angle rotations of the scanner. The effects of coil parameters on the material magnetization and the hysteresis of the magnetic force on the scanner dynamics are discussed. It is concluded that the radial and vertical components of the magnetic field and the shape anisotropy in thin magnetic films are important factors in determining the material magnetization direction and the magnetic forces. The prototype devices are tested using static and dynamic methods and the experimental results

validated our finite element modeling and theoretical results. Lastly a barcode reading system is demonstrated using the developed scanners and met all the performance requirements for typical 1D barcodes.

Özet

Bu tezde polimer kalıplama ve manyetik film elektrokaplama yöntemleri kullanılarak üretilen basit ve düşük maliyetli rezonans lazer taryıcıların tasarımı ve geliştirilmesi anlatılmaktadır. Burada anlatılan polimer manyetik tarayıcılar, prototip bir barkod okuyucu düzeneğinde kullanılmış ve elde edilen performansın çeşitli tek boyutlu ve iki boyutlu görüntüleme uygulamaları için yeterli olduğu kanıtlanmıştır. Bu çalışmanın en önemli katkıları (1) polimerler ve elektrokaplama ile elde edilmiş manyetik malzemeler kullanarak basit ve düşük maliyetli üretim metodunun geliştirilmesi (2) manyetik malzemeler kullanarak bir boyutlu ve iki boyutlu tarama işlemleri için dinamik tahrikleme metodlarının modellenmesi ve geliştirilmesi olarak sıralanabilir.

Bu çalışma için iki tür tarayıcı tasarlanmıştır: Yalniz bir ucu destekli olan bükülme ile çalışan tarayıcılar, iki ucu destekli burulma ile çalışan tarayıcılar. Geliştirdiğimiz metod, mikro teknoloji ile üretilen tarayıcılardan farklı olarak, temiz oda veya foto-litografi işlemleri gerektirmemektedir. Polimerler kalıplama ile yada kesilerek istenilen şekle getirilmiş, tarayıcı ayna olarak kullanılmışlardır. Değişik tip kendinden sertleşen yada morötesi ışıkla sertleşen polimerler yapısal malzeme olarak denenmişlerdir. Morötesi ışıkla sertleşen polimerle ve baskı devre üreticileri tarafından kullanılan üzeri bakır kaplı kartlarla iyi sonuçlar elde edilmiştir. Yüksek yansıtıcılık ve ayna yüzey kalitesi için polimerin bir yüzü ya Aluminyum kaplanmış yada Aluminyum kaplı Silikon bir ayna tarayıcıya iliştirilmiştir. Manyetik malzemenin yapısal malzemeyle birleştirilmesi iki türlü gerçekleştirilmiştir: (1) Toz halindeki manyetik parçacıkların polimerle karıştırılması, (2) polimerin altına nikel demir alaşım filmin elektrokaplanması. Rezonans modunda dinamik tahrikleme, dışarıdaki bir elektro-mıknatısa zamanla değişen bir akım uygulanmasıyla sağlanmıştır. Aynı manyetik alan için, elektrokaplama ile yapılmış tarayıcılardaki manyetik kuvvetin, manyetik parçacıklı tarayıcılarla elde edilen manyeti kuvvetten daha güçlü olduğu gözlenmiştir. Nikel demir alaşım filmlerin elektrokaplanması kaplama laboratuarımızda gerçekleştirilmiştir.

Bu çalışmanın katkılarından bir başkası da yumuşak manyetik malzeme kullanan tahrik mekanizmalarının doyma ve doğrusal modlarda modellenmesi ve optimizasyonu üzerine olmuştur. Bu çalışma, tarayıcının küçük açısal dönüşlerini incelemektedir. Elektro-mıknatıs parametrelerinin malzeme magnetizasyonu üzerindeki etkileri ve manyetik malzemenin ardıl izleminin tarayıcı dinamiği üzerindeki etkileri incelenmiştir. Manyetik alanın radyal ve dik bileşenlerinin ve ince

manyetik filmlerdeki şekilsel anizotropinin, malzeme magnetizasyonunu ve manyetik kuvvetleri belirleyen önemli faktörler olduğu anlaşılmıştır. Prototip cihazlar static ve dinamik methodlar kullanılarak test edilmiş, deneysel sonuçlar teorik ve sonlu eleman anlizi sonuçlarını doğrulamıştır. Son olarak, üretilen tarayıcılar kullanılarak bir barkod okuyucu sistemi gösterilmiş ve tipik bir boyutlu barkodlar için performans kriterleri yakalanmıştır.

ACKNOWLEDGEMENTS

First of all, I would like to express my gratitude to my supervisor Assoc. Prof. Hakan Ürey for providing me with the opportunity to do this Master's project. Being a member of the Optical Microsystems Laboratory (OML) had been a unique experience.

I would like to thank Dr. Arda Deniz Yalçınkaya for contributing to this project and for his advises throughout this work. The discussions with him and Prof. Ürey were invaluable.

I would like to thank Asst. Prof. Erdem Alaca and Asst. Prof. Funda Yağcı Acar not only for taking part in my thesis jury but also for their help and support throughout this work. Also I would like to thank Assoc. Prof. Levent Demirel and Prof. Mehmet Somer for their extensive help and support.

I acknowledge KÜMPEM, TÜBİTAK and Microvision for supporting this project. Also I appreciate Aselsan for providing samples and helping with the production of scanners. I acknowledge Koc University, College of Engineering for supporting me through travel grants that enabled me to participate in international conferences.

I would like to thank Özgür Kaya for taking me everywhere in Istanbul safely and for making the long hours spent in the OML fun. I had the privilege of working with Hamdi Torun. I would like to thank him and Ece Özlem Atikcan for their precious friendship and their team work. Special thanks go to permanent employee of the OML, Çağlar Ataman. Without him nothing will work in the lab. Also thanks to Volkan Kurt especially for the last days of this work.

I would like to thank Özlem Şardan for the EDS and SEM measurements, Burak Öztürk and Aydın Yetiştiren for helping me with preparing the molds; Melih Altun and Rıfat Türsen for building the barcode reading setup, Fatih Toy for helping with experimental work, Muharrem Güler for blowing glass and Dimitrios Ipsakis for helping me with preparing different materials. Special thanks to Garbis Bey and Hıraç Bey from Emin Metalize for their help and interest.

I was fortunate to come across Dr. Kamuran Altılar while wandering around Karaköy. He was generous to share his experience and contacts. I am grateful to him for giving me motivation and inspiration.

I would like to express my sincere gratitude to Burhan Öçal, Keith Jarrett, Tchaikovsky, Anouar Brahem, Kalan Müzik and many others for providing me motivation throughout this work.

Lastly, I would like to thank my mom, dad, grandma, Işın and Dicle. I appreciate their support and understanding. Without you this work would not be possible.

TABLE OF CONTENTS

LIST OF TABLES

LIST OF FIGURES

1 INTRODUCTION

Laser scanners have found many applications and penetrated into many consumer products for many years. Barcode readers used in supermarkets and projection systems are just two examples of many products that make use of scanners. A scanner is a reflective light steering element. Today, scanners offer effective solutions to different engineering problems. Some of the major application areas of scanners are optical communications, optical data storage, display and imaging systems, spectroscopy, lithography, medical systems and laser printing.

This thesis mainly deals with the design and development of resonant laser scanners with very simple and low-cost fabrication process using molded polymers and electroplated magnetic films for magnetic actuation. The scanner performance is adequate for barcode reading and various imaging applications. Section 1.1 gives an overview of scanners used in display and imaging applications and Section 1.2 gives an overview of different scanner actuation mechanisms. The main contributions of the thesis and the outline are discussed in Section 1.3.

1.1 Scanners for Display and Imaging Applications

Among all the application areas, the fundamental application field of scanners is the display and imaging systems. Fast scanning speeds and high scan angles achieved by the microscanner technologies make them a good candidate for this type of applications. There are a wide variety of display applications that utilize Micro Electro-Mechanical Systems (MEMS) scanners.

Retinal Scanning Display (RSD) is an example of a display product using micro scanners. This is a head mounted micro-display developed by Microvision, Inc. The device utilizes a single two dimensional MEMS scanner for scanning video data onto the retina of the user [1]. It is a see-through display that augments the displayed image onto what is actually seen by the user. Performance constraints for a scanner based high-resolution display system like RSD require a very careful design

of the scanner. The trade-offs and critical issues of scanner design for display systems are challenging, and have been the subject of several articles [2][3][4].

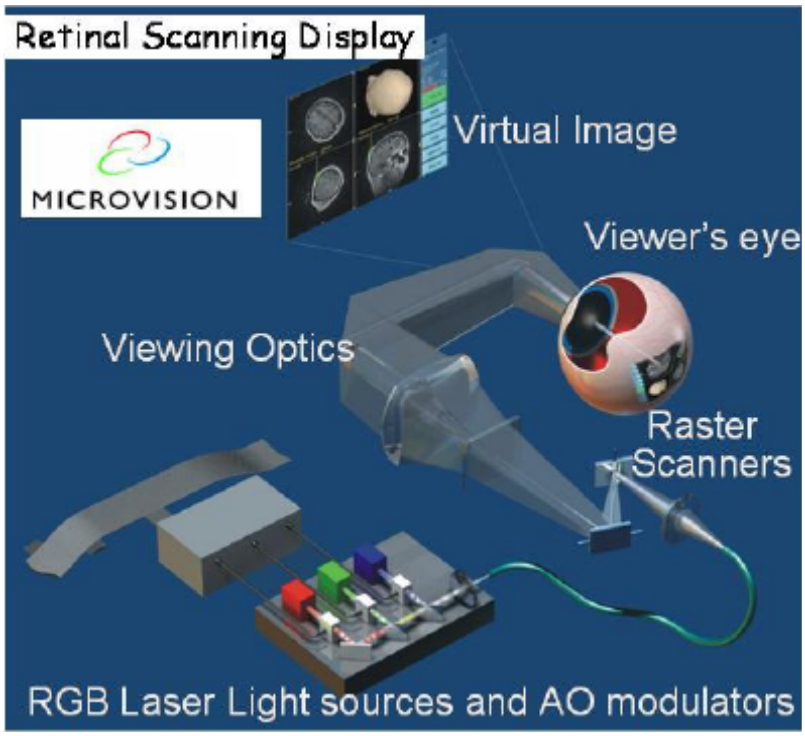

Figure 1-1 Retinal Scanning Display Technology of Microvision, Inc uses a 2D MEMS scanner. (Photo courtesy of Microvision, Inc)

As a second display system, Fraunhofer IPMS demonstrated a laser projection device using micro scanners [5]. The presented demonstrator uses special miniaturized projection module consisting of a laser diode, collimator optics, and a 2D micro scanner. Using micro scanners for steering of the laser beam in a projection device has many advantages. In particular, micro scanners, which operate resonantly in both directions, enable the development of systems with very small size. High deflection angles with low power consumption can be achieved. Applications of the projection device are displays, laser marking and laser exposure.

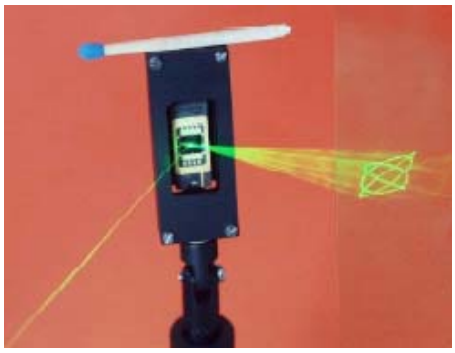

Figure 1-2 A laser projection device concept incorporating a 2D MEMS scanner (Photo courtesy of Fraunhofer IPMS)

In addition to the mentioned display applications, scanner technologies are also utilized in imaging systems. Barcode reading is probably the most important imaging application of today's scanner technologies. They offer effective solutions for reading both regular 1D and 2D barcodes. Higher scanning frequency and lower power consumption of scanners compared to conventional technologies make scanners an attractive choice for compact, hand-held barcode readers [6].

One major issue about barcode scanners may be the mechanical reliability, since a handheld device may experience high shocks due to dropping, hitting, etc. There are various other MEMS scanners geared for display and imaging applications [7][8][9][10][11].

Figure 1-3 A hand-held laser scanning barcode reader (Photo courtesy of Microvision, Inc)

1.1.1 *Barcode Reading Applications*

A barcode reader is a system used to extract the information that is optically encoded in a special symbol and convert it into a digital electrical signal to be processed in a computer. It generally consists of a light source, a scanner, optics needed to focus the laser beam onto the barcode surface and a photo diode to collect and translate the optical impulses from scattered light emanating from the barcode surface into electrical pulses. Additionally, nearly all barcode readers currently produced contain a decoder analyzing the barcode's image data provided by the photo diode and sending the barcode's content to the scanner's output port. The decoder consists of an A/D converter and a processor. Among various scanning mechanisms for barcode reading systems, scanning mirrors referred to as scanners throughout this thesis- provide the most effective solution as they need little operator skill and that they benefit from a large number of scanning attempts in a short period of time. Their relative low cost is another major advantage [12][13].

Different from other display and imaging applications, scanners for barcode reading applications do not require demanding specifications. A scanner that is 1 mm or larger and a mechanical angle of ± 5 degrees is sufficient to read barcodes. As illustrated in Figure 1-4 optical angle is twice the mechanical angle, so this makes ± 10 degrees optical angle.

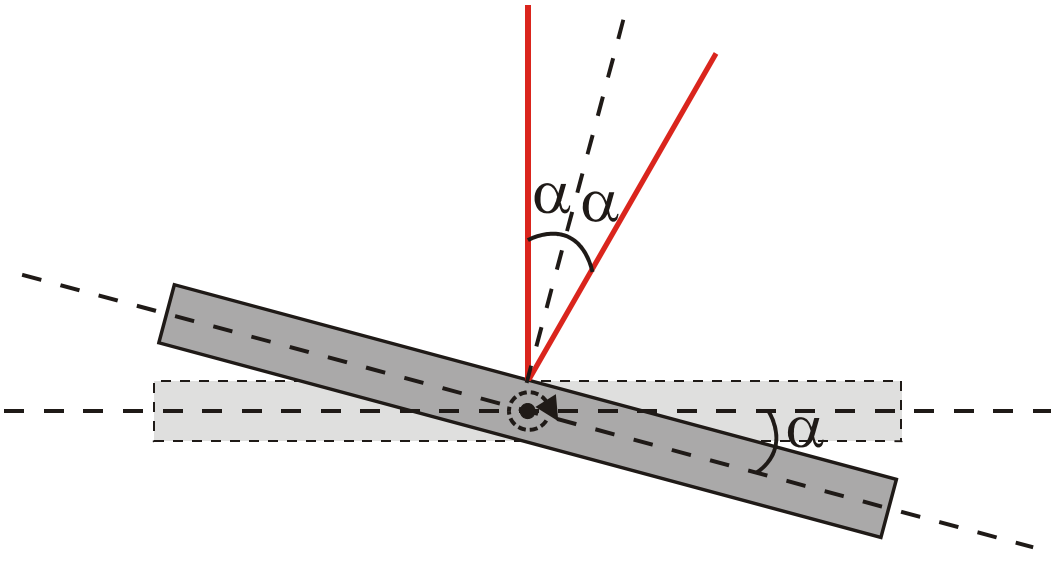

Figure 1-4 Optical scan angle is twice the mechanical tilt angle, α.

Barcode readers do not need high scanning frequencies. Several scanning attempts per second are sufficient to read and control a barcode. Furthermore, devices operating at low frequencies eliminate the need for fast electronics for signal processing.

Development of polymer scanners is driven by the need for inexpensive, simple, compact and easily fabricated scanners for barcode reading and other imaging applications. An electromagnet and a polymer scanner with magnetic material can be utilized to achieve a system with the desired properties. Using polymers as the structural material enables devices with low resonant frequencies due to their mechanical properties. Furthermore mold shaping of polymers reduce the fabrication costs yielding low cost scanners.

1.2 Actuation Mechanisms

Microscanners are generally categorized based on their actuation mechanism. There are many different actuation mechanisms that exploit different physical principles such as electrostatic, electromagnetic, thermal and piezoelectric. Electrostatic and electromagnetic are the most commonly used actuation methods for scanners based on fabrication, the force produced and power consumption.

1.2.1 *Electrostatic Actuation*

Electrostatic actuation is the most popular actuation mechanism for microscanners, since they are compatible with integrated circuit fabrication process and they are capable of generating relatively large forces over small gaps with low power. There are microscanners actuated with parallel plate [14][15][16] or comb-drive [17][18] electrostatic actuators. The main drawbacks for electrostatic actuation are high voltage requirements which is generally limited by either the dielectric breakdown of air or insulator used to isolate different potentials or by the integrated circuit used in the system. Furthermore, the magnitude of electrostatic force decreases rapidly as the gap between electrodes increases. Electrostatic actuation therefore cannot generally provide large forces over long range of

displacement. Electrostatic actuators can draw dust particles out of the air onto the device if they are used in an unprotected environment. Also, they cannot be used in conductive fluids.

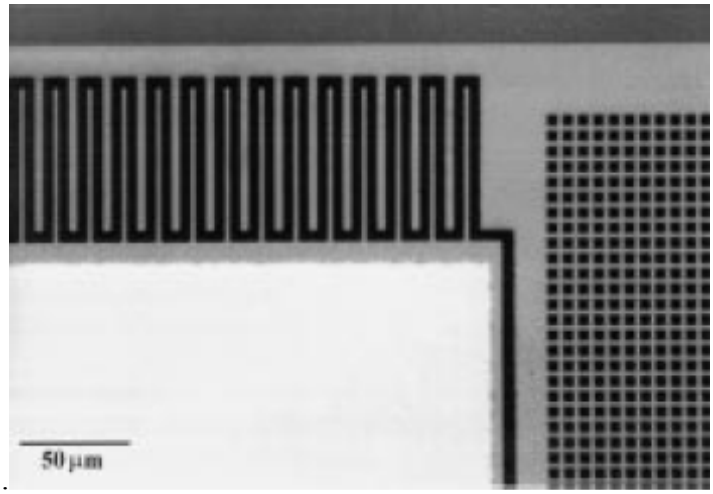

Figure 1-5 Comb drive capacitive actuators on a silicon micromirror. Comb drives increase the force produced by electrostatic actuators by increasing the effective electrostatic interaction area (photo courtesy of Fraunhofer, IPMS).

1.2.2 *Electromagnetic Actuation*

Magnetically actuated scanners can make use of the Lorentz forces, magnetostatic forces, or magnetic anisotropy torques [19]. Magnetic actuators can be classified as moving coil actuators [2][20] and moving magnetic material actuators. The moving magnetic material actuators can be further classified as hard magnetic material [21][22] and soft magnetic material actuators [23][24][25]. More details about the magnetic torques and forces and detailed analysis of different kinds of magnetic actuators can be found in Chapter 3.

Magnetic actuators are attractive because they can achieve large forces. They can operate in conductive fluids and do not attract dust particles as electrostatic actuators do. Magnetic actuators need relatively high currents to generate large forces. Magnetic forces and torques can be increased

by the help of ferromagnetic materials, but these materials require non IC fabrication processes and equipment [19].

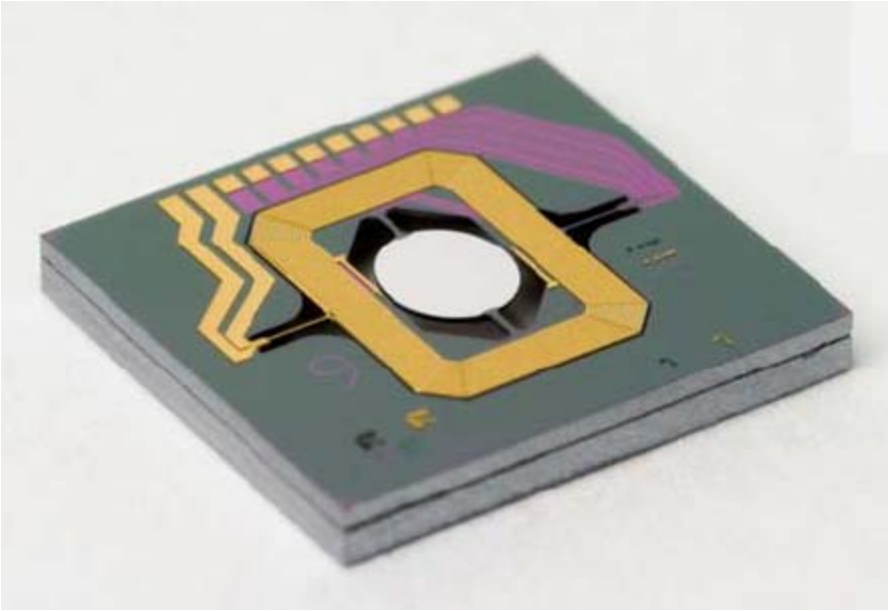

Figure 1-6 A moving coil magnetic scanner produced by Microvision Inc. It makes use of the Lorentz force applied to the current carrying coil that is placed in an external DC magnetic field. (Photo courtesy of Microvision, Inc)

1.2.3 *Other Actuation Mechanisms*

In addition to electrostatic and electromagnetic actuation other actuation principles are also possible like thermal and piezoelectric actuation. Thermally actuated microscanners take advantage of the different thermal coefficients of two or more layers. Most important design challenge for such a structure is to maximize the thermal coefficient mismatch between the two materials of the bimorph structure. This requires a good material selection in the design phase. Actuation based on thermal expansion typically suffers from high energy consumption, sensitivity of thermal noise and slow time response [26][27].

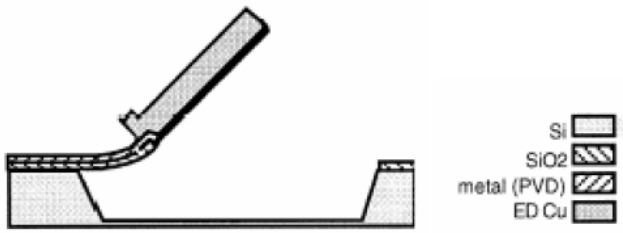

Figure 1-7 Cross section of a thermally actuated microscanner. The cantilever beam holding the mirror is bimorph consisting of two materials with different thermal expansion coefficients [26]. Heating and cooling of the device bends the cantilever beam and actuates the mirror.

In the case of piezoelectric actuation, the bending of a bimorph beam or plate is induced by an electric field. With proper mechanical design this transducer effect can be utilized for microscanner design [28][29]. Piezoelectric actuators provide high precision motion, however they require very high potentials for small deflection amounts. The energy-coupling coefficient and the maximum strain of existing materials are still small. The compatibility of existing piezoelectric films with conventional IC fabrication processes remains an active and challenging research topic [30].

1.3 Main Contributions and Outline

Main contributions of this thesis can be summarized as:

- Modeling and optimization of the magnetic actuation using electroplated thin films in both saturated and unsaturated modes of operation.
- Development of the process for lithography-free fabrication using polymers as the structural material.
- Performance comparison of electroplated magnetic films with magnetic particles mixed in the polymer substrate.
- Application of such actuators to laser scanning and barcode readers.

Chapter 2 gives an overview of scanner mechanics. The mechanics of beams are described and cantilever beam type and torsional type scanners are investigated. Their static deflection

characteristics, natural frequencies and mode shapes are analyzed using theoretical calculations and finite element modeling. Lastly the second order system dynamics is reviewed. Chapter 3 focuses on magnetic actuation by describing the fundamentals of magnetism and magnetic materials. The modeling of an electromagnet is also presented by giving the related mathematical equations and finite element modeling analysis. In chapter 4 fabrication of the scanners and magnetic material characterization are described. Molding of polymers, preparation of polymers with magnetic particles, fabrication of scanners using conventional machining and methods of depositing magnetic materials are described. A setup used for magnetic material characterization is investigated. Chapter 5 describes two prototype polymer magnetic scanners: a cantilever beam scanner and a torsional scanner. Complete models of the performance at small angular displacements of each prototype are developed and compared with experiments. A barcode reading system using these scanners is presented as an application for these scanners. Chapter 6 discusses the conclusions, the future research opportunities and possible application areas for polymer magnetic scanners described in this thesis.

2 SCANNER MECHANICS

In this chapter mechanics of cantilever beam scanners and torsional scanners are examined. In 2.1 the general structure of the scanners are presented. Section 2.2 presents analytical and finite element modeling (FEM) results for deflection of the cantilever scanner structure. Due to resonant mode operation, dynamics of the structure is important. Section 2.3 investigates the natural frequency and the mode shapes of the scanners for resonant mode operation and Section 2.4 reviews the second order linear system dynamics.

2.1 General Structures of the Scanners

Mechanical behavior of structural elements is well-known and the details of this can be found in a number of references [31][32][34]. Of particular interest in this work is the behavior of cantilever beams and torsional bars. Their cross-sectional moments of inertia and how they are supported are the factors that determine the mechanical behavior. Moment of inertia of the area A with a cross section in y-z plane with respect to z axis is given by [31]:

$$I_z = \int_A y^2 dA \tag{2-1}$$

In simple cases moment of inertia can be calculated analytically. Moment of inertia for different cross sections can be found in [32]. Moment of inertia of a rectangular cross section with width w and height h with respect to z axis (height direction) is given by

$$I_z = \frac{hw^3}{12} \tag{2-2}$$

2.1.1 *Cantilever Beam Scanner*

Figure 2-1 shows the general structure of the cantilever beam scanner. It consists of a narrow cantilever beam supporting a rectangular mirror. The cantilever beam is anchored at one end. Table 2-1 shows the material properties and dimensions of the supporting beam and mirror for one of the prototypes. The dimensions of the other prototype devices can be found in APPENDIX A.

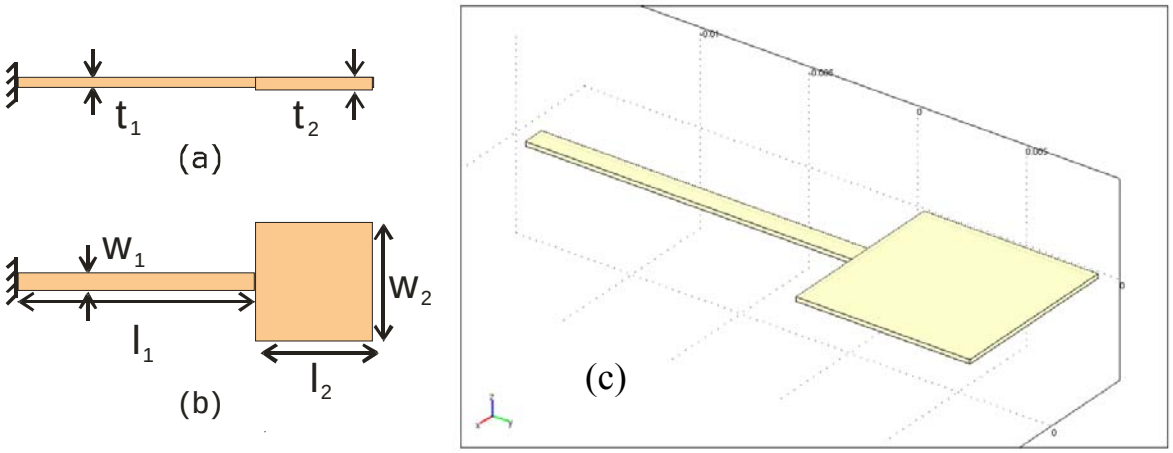

Figure 2-1 General structure of the cantilever beam scanner: (a) Side view, (b) top view and (c) 3-D view. The narrow supporting beam is anchored from the end.

Width of the Suspension	w_1	1 mm
Width of the Mirror	w_2	8 mm
Length of the Suspension	l_1	15 mm
Length of the Mirror	l_2	8 mm
Thickness of the Suspension	t_1	0.5 mm
Thickness of the Mirror	t_2	0.5 mm
Young's Modulus	E	1.628×10^9 Pa
Density	ρ	1200 kg/m^3

Table 2-1 The material properties and dimensions of the supporting beam and the mirror for one of the prototypes.

2.1.2 *Torsional Scanner*

Figure 2-1 shows the general structure of the torsional scanner. It consists of a rectangular mirror anchored at both ends by narrow torsion bars. Table 2-1 shows the material properties and dimensions of the mirror and the supporting torsion bars for one of the prototypes. The dimensions of the other prototype devices can be found in APPENDIX A.

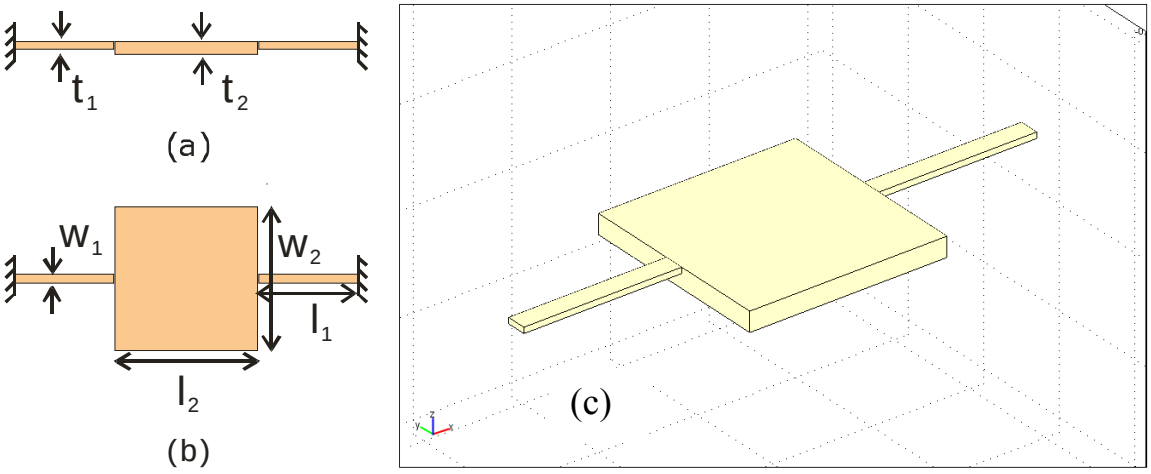

Figure 2-2 General structure of the torsional scanner: (a) Side view, (b) top view and (c) 3-D view. The rectangular mirror is anchored at both ends by narrow torsion bars.

Width of the Torsion Bar	w_1	1 mm
Width of the Mirror	w_2	10 mm
Length of the Torsion Bar	l_1	7 mm
Length of the Mirror	l_2	10 mm
Thickness of the Torsion Bar	t_1	0.3 mm
Thickness of the Mirror	t_2	1 mm
Young's Modulus	E	1.628×10^9 Pa
Density	ρ	1200 kg/m^3

Table 2-2 The material properties and dimensions of the supporting beam and mirror for one of the prototypes.

2.2 Static Deflection of the Beam

2.2.1 *Theoretical Analysis*

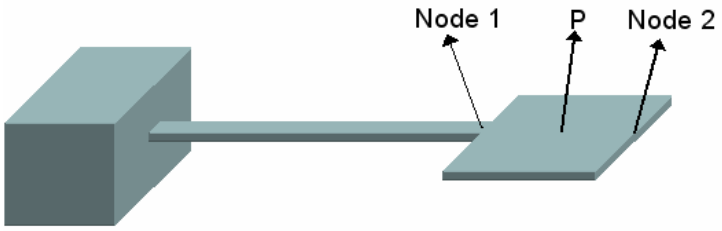

Figure 2-3 Geometry of the cantilever beam scanner and the nodes.

This section gives the static response of the actuator to an applied pressure. The geometry of the analyzed actuator is shown in Figure 2-3. A pressure F_P is applied to the rectangular area at the end of the beam. The block on the left is the anchor and the rectangular area at the right is the mirror. For analytical calculations we assumed a concentrated force $F = F_P \cdot A$ is applied at the center of the mirror (at P). A is the area of the mirror ($A = l_2 \, x \, w_2$). To find the deflection at node 1, we need the equivalent force and moment at node 1. The force at P generates a force F_1 and moment M_1 at node 1.

$$F_1 = F \tag{2-3}$$

$$M_1 = F \cdot \frac{l_2}{2} \tag{2-4}$$

where l_2 is the length of the mirror. The static deflection at node 1 is given by [31],

$$\delta_1 = \delta_{1F} + \delta_{1M} = \frac{F_1 \cdot l_1^3}{3 \cdot E \cdot I_1} + \frac{M_1 \cdot l_1^2}{2 \cdot E \cdot I_1} \tag{2-5}$$

where δ_{1F} is the deflection due to force F_1, δ_{1M} is the deflection due to moment M_1, E is the Young's Modulus of the material, l_1 is the length of the suspension beam, I_1 is the moment of inertia of the

suspension beam. Moment of inertia of the suspension beam, I_1 and moment of inertia of the mirror, I_2 are given by,

$$I_1 = \frac{w_1 \cdot t_1^3}{12} \tag{2-6}$$

$$I_2 = \frac{w_2 \cdot t_2^3}{12} \tag{2-7}$$

Substituting (2-6) into (2-5) gives,

$$\delta_1 = \frac{4 \cdot F_1 \cdot l_1^3}{E \cdot w_1 \cdot t_1^3} + \frac{6 \cdot M_1 \cdot l_1^2}{E \cdot w_1 \cdot t_1^3} \tag{2-8}$$

The angle of deflection at node 1 can be calculated as [31],

$$\theta_1 = \theta_{1F} + \theta_{1M} = \frac{F_1 \cdot l_1^2}{2 \cdot E \cdot I_1} + \frac{M_1 \cdot l_1}{E \cdot I_1} \tag{2-9}$$

The static deflection at the tip of the mirror can be calculated with,

$$\delta_{CM} = \delta_1 + \delta_2 + \theta_1 \cdot l_2 \tag{2-10}$$

where l_2 is the length of the mirror, δ_2 is the deflection of the mirror relative to node 1 (bending of the mirror) and the last term is the deflection of the mirror due to θ_1. δ_2 is given by [32],

$$\delta_2 = \frac{5 \cdot F_1 \cdot l_2^3}{48 \cdot E \cdot I_2} \tag{2-11}$$

The maximum stress for a deflected cantilever beam is given by [34],

$$\sigma_{\max} = \frac{6 \cdot l_1 \cdot F_{eqv}}{t_1^2 w_1} \tag{2-12}$$

where F_{eqv} is the force applied at the tip of the cantilever beam. Since the mirror is rigid compared to the supporting beam we can neglect the mirror part for the stress analysis. The force that will cause a deflection of δ_1 at node 1 (assuming moment is zero in (2-5)) is given by,

$$F_{eqv} = \frac{3 \cdot \delta_1 \cdot E \cdot I_1}{l_1^3} \tag{2-13}$$

The mechanical stiffness k_x and the angular mechanical stiffness k_ϕ can respectively be defined as the ratio of the force (F) to displacement (x) and the ratio of the torque (T) to rotation angle (ϕ) as

$$k_x = \frac{F}{x} = \frac{E \cdot w_1 \cdot t_1^3}{4 \cdot l_1^3 + 3 \cdot l_2 \cdot l_1^2} \tag{2-14}$$

$$k_\phi = \frac{T}{\phi} = \frac{E \cdot w_1 \cdot t_1^3}{6 \cdot l_1^2} \tag{2-15}$$

2.2.2 *FEM Analysis*

FEM analysis was done using FEMLAB 3.0 . The dimensions and material properties given in Table 2-1 were used to build the model. For boundary conditions, fixed displacement at the suspension end is used and the force is applied on the mirror. For an applied force of 20 mN, FEM analysis shows a tip deflection of 1,685 mm and a maximum stress of 4.57 Mpa. The analytical model shows a tip deflection of 1.69 mm and a maximum stress of 4.32Mpa.

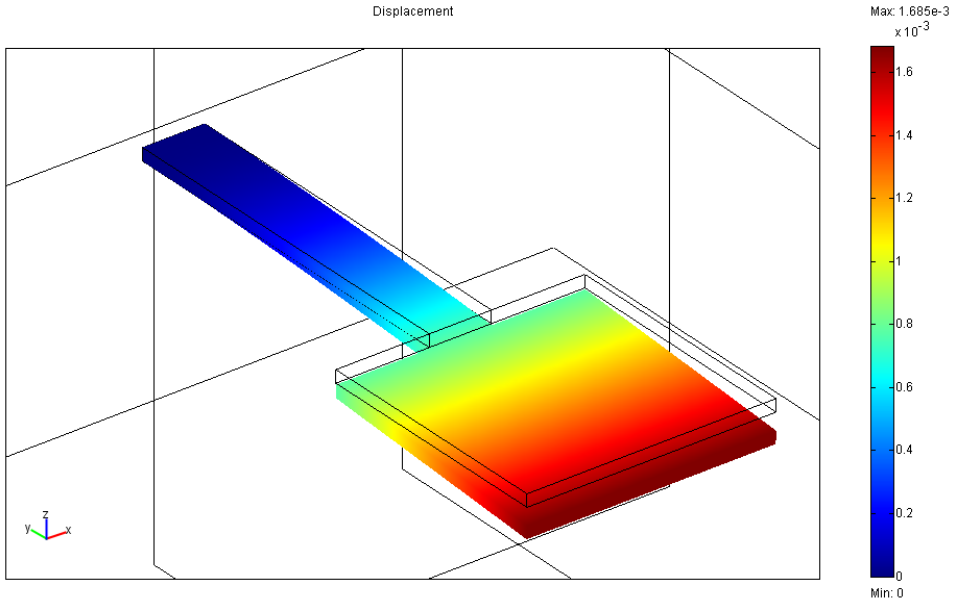

Figure 2-4 Simulated displacement of the actuator by FEM.

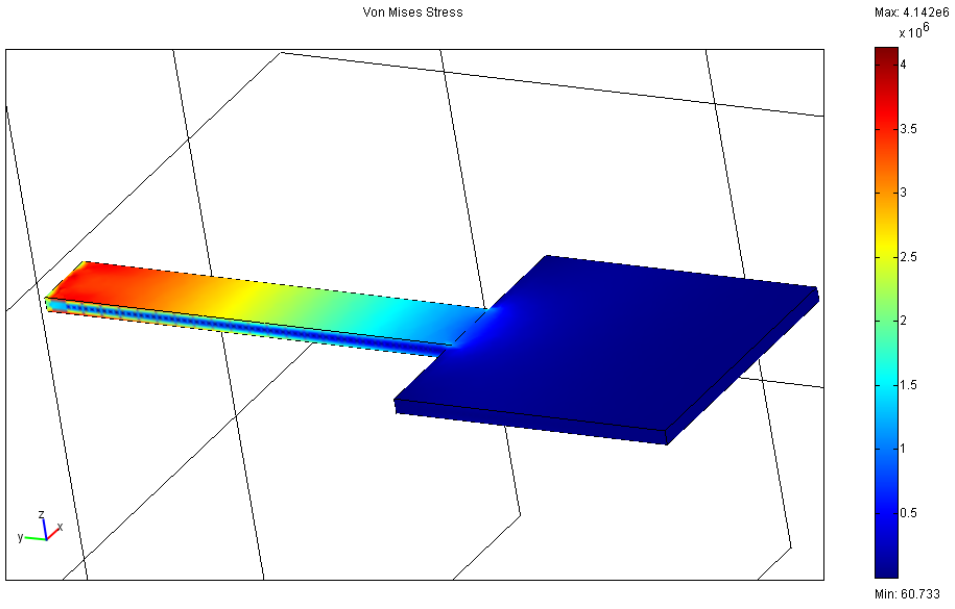

Figure 2-5 Simulated stress distribution of the actuator by FEM.

Force was applied in two different ways to check the validity of the analytical model. In the first analysis a distributed force was applied to the entire volume of the mirror as a force density (F/V). In the second analysis a point force was applied to the center of the mirror. The results clearly show that applying F at a single point in the analytical computations does not significantly affect the results. The analytical results are in good agreement with FEM model.

A similar analysis can be carried out for the torsional scanner. If a pure moment without a translational force is applied to the torsional scanner, it rotates the scanner through an angle ϕ. The torsional stiffness k_ϕ can be expressed as [14]

$$k_\phi = \frac{2 \cdot G \cdot K}{l_2} \tag{2-16}$$

$$K \approx (a \cdot b^3)\left(5.33 - 3.36 \cdot \frac{b}{a}\left(1 - \frac{b^4}{12 \cdot a^4}\right)\right) \tag{2-17}$$

$$G = \frac{E}{(2(1+\nu))} \tag{2-18}$$

where G is the torsional modulus, K is a shape factor for rectangular flexures, E is the Young's modulus, υ is the Poisson's ratio, $2a = \max(w_1, t_1)$ and $2b = \min(w_1, t_1)$.

2.3 Natural Frequency and Mode Shapes

2.3.1 *Theoretical Analysis*

It is possible to estimate the resonant frequencies of the scanners by Rayleigh-Ritz methods [34]. When the structure deforms, the displacement changes with position. The kinetic energy is a function of the displacement and varies across the structure. Under sinusoidal excitation we can estimate the displacement of a differential element on the actuator as,

$$\varpi(x,t) = \varpi(x)\cos(\omega t) \tag{2-19}$$

We can use energy methods to calculate the elastic strain energy W_e and the corresponding total potential energy PE using the maximum deflection of the scanner. When $t = \pi/2\omega$, the deflection is zero everywhere, but the velocity is maximum. The maximum kinetic energy is attained at that time and given by

$$\left.\frac{\partial \varpi(x,t)}{\partial t}\right|_{t=\pi/2\omega} = -\omega\varpi(x) \tag{2-20}$$

The kinetic energy of a differential element is,

$$\widetilde{W}_k = \frac{\omega^2}{2}\rho_m(x)\varpi(x)^2 \tag{2-21}$$

where $\rho_m(x)$ is the mass density of the actuator at position x. To find the total maximum kinetic energy, $\widetilde{W}_k$ must be integrated over the volume of the beam. As the velocity and volume of the mirror is much larger than velocity and volume of the suspension, we can neglect the suspension part in the integration.

$$W_k = \frac{\omega^2}{2}\int_{volume}\rho_m(x)\varpi(x)^2\,dxdydz \tag{2-22}$$

If the damping is ignored the maximum kinetic energy is equal to the maximum potential energy, (W_e) at resonance. Thus the resonant frequency, ω_0 can be calculated as:

$$\omega_0^2 = \frac{W_e}{\int_{volume}\frac{1}{2}\rho_m(x)\varpi(x)^2\,dxdydz} \tag{2-23}$$

If we call the denominator of the above equation W_k'' then,

$$W_k'' = \frac{W_k}{\omega_0^2} \tag{2-24}$$

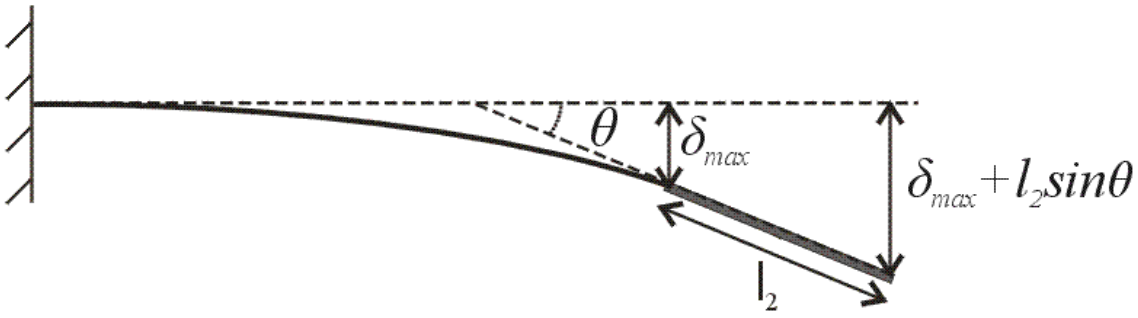

Figure 2-6 Cantilever beam scanner deflection.

W_k'' can be calculated for the cantilever beam scanner as,

$$W_k'' = \tfrac{1}{2}\int_0^{l_2} \rho w_2 t_2 (\delta_{\max} + l\sin\theta)^2 \, dl$$
$$W_k'' = \frac{\rho w_2 t_2}{2}\left[\delta_{\max}^2 l_2 + l_2^2 \delta_{\max}\sin\theta + \frac{l_2^3 \sin^2\theta}{3}\right] \tag{2-25}$$

where is shown in Figure 2-6 and δ_{max} is the maximum deflection at node 1. If we use small angle approximation, (2-25) is simplified as,

$$W_k'' = \frac{\rho w_2 h_2}{2}\left[\delta_{\max}^2 l_2 + l_2^2 \delta_{\max}\theta + \frac{l_2^3 \theta^2}{3}\right] \tag{2-26}$$

The elastic strain energy, W_e can be calculated with [31],

$$W_e = \frac{E}{2}\int_{volume} \varepsilon^2 dxdydz \tag{2-27}$$

where ε is the strain and E is the Young's modulus. We can neglect the strain on the mirror as it is very small compared to the strain on the suspension. So the integration for W_e can be carried out just on the suspension and the equivalent force, F_{eqv} given by (2-13) will be used to calculate the strain. The stress on a beam bent by the force, F_{eqv} is given by,

$$\sigma = \frac{-My}{I_1} \tag{2-28}$$

where M is the bending moment, y is the distance from the neutral axis and I_1 is the moment of inertia given by (2-5).

$$M = (l_1 - x)\cdot F_{eqv} \tag{2-29}$$

$$\sigma = \frac{(l_1 - x)\cdot F_{eqv}\cdot y}{I_1} \tag{2-30}$$

The strain is given by,

$$\varepsilon = \frac{\sigma}{E} = \frac{(l_1 - x)\cdot F_{eqv}\cdot y}{E\cdot I_1} \tag{2-31}$$

Putting (2-31) into (2-27) for the cantilever beam scanner gives,

$$W_e = \frac{E}{2}\int_0^{l_1}\int_{-h_1/2}^{h_1/2} w_1 \cdot \left[\frac{(l_1 - x)\cdot F_{eqv}\cdot y}{E\cdot I_1}\right]^2 dydx \tag{2-32}$$

Evaluating the integration W_e becomes,

$$W_e = \frac{F_{eqv}^2 \cdot h_1^3 \cdot l_1^3 \cdot w_1}{72 \cdot I_1^2 \cdot E} \tag{2-33}$$

and substituting I_1 given by (2-6) into (2-33) gives,

$$W_e = \frac{2 \cdot F_{eqv}^2 \cdot l_1^3}{w_1 \cdot h_1^3 \cdot E} \tag{2-34}$$

Using (2-26) and (2-33), the resonant frequency can be calculated:

$$\omega_0 = \sqrt{\frac{W_e}{W_k''}} \tag{2-35}$$

A similar derivation can be performed for the torsional scanner geometry. The first resonance frequency is given by

$$\omega_0 = 2\pi f = \sqrt{k_\phi / J_{eff}} \tag{2-36}$$

where k_ϕ is the torsional stiffness given by (2-16) and J_{eff} is the effective mass moment of inertia given by

$$J_{eff} = J_{m,xx} + (2/3)\cdot J_{f,xx} \tag{2-37}$$

$$J_{f,xx} = \tfrac{1}{3} M_f (a^2 + b^2) \tag{2-38}$$

$$M_f = \rho \cdot w_1 \cdot t_1 \cdot l_1 \tag{2-39}$$

$$J_{m,xx} = \frac{\rho \cdot w_2 \cdot l_2 \cdot t_2}{12} (w_2^2 + t_2^2) \tag{2-40}$$

where $2a = \max(w_1, t_1)$ and $2b = \min(w_1, t_1)$, ρ is the density of the material, $J_{m,xx}$ is the mass moment of inertia of the mirror, M_f is the mass of the flexures, $J_{f,xx}$ is the mass moment of inertia of the flexures [33].

2.3.2 *FEM Analysis*

The calculated resonant frequency using the dimensions and material properties given in Table 2-1 is 79.45 Hz. The modal analysis with FEMLAB shows the first resonant frequency is at 79.72 Hz, which is in very good agreement with the analytical model. Eigenfrequencies for the first six modes and the mode shapes are illustrated in Figure 2-7.

Figure 2-8 shows the first six mode shapes and frequencies for the torsional scanner with dimension given in Table 2-2. The resonance frequency is found as 184.56 Hz from the FEM analysis and 184.45 Hz from the theoretical analysis.

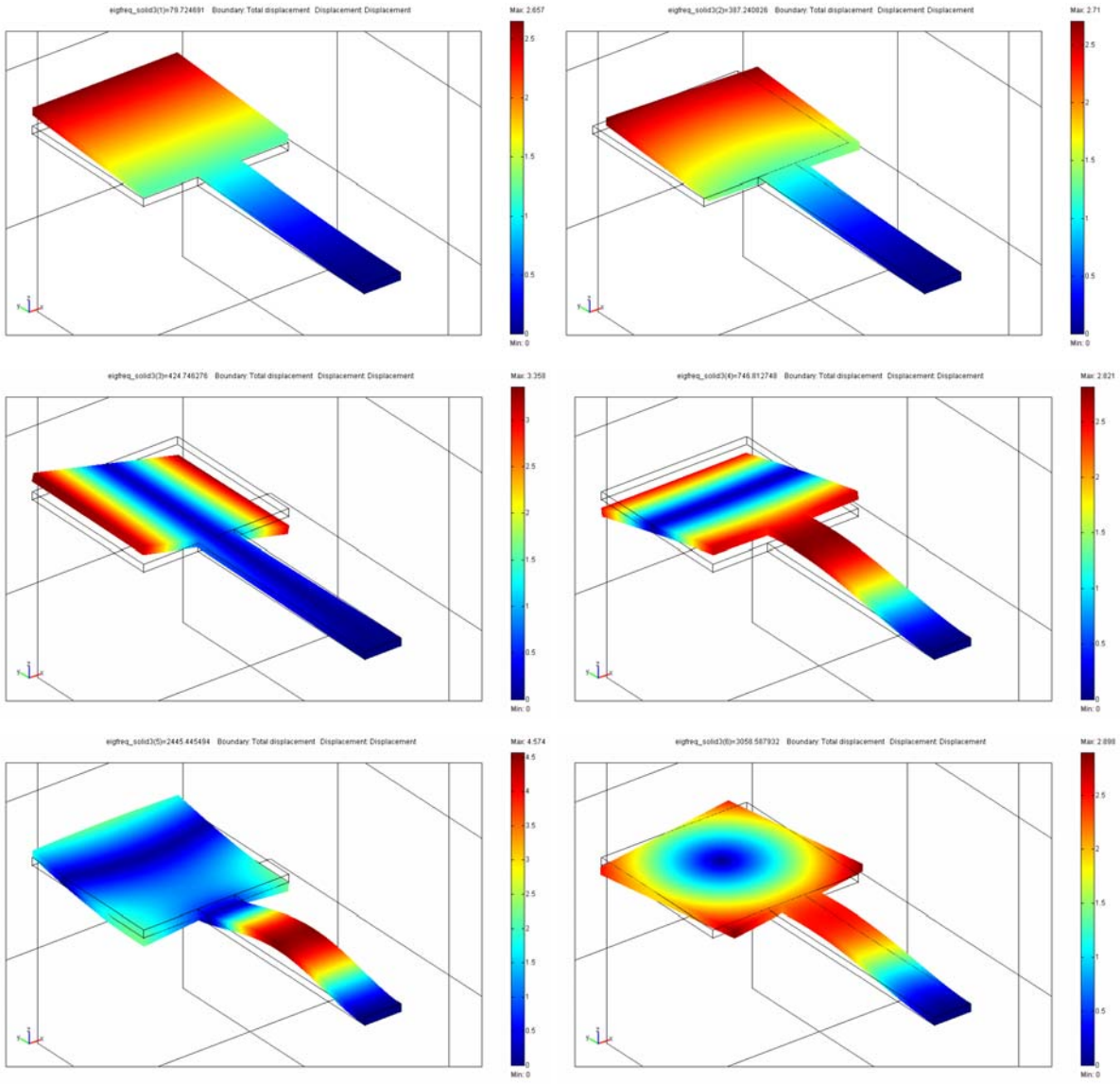

Figure 2-7 The first six eigenfrequencies and corresponding mode shapes of the cantilever beam scanner. (f_1 = 79,72 Hz, f_2 = 387,24, f_3 =424,75 Hz, f_4 = 746,81 Hz, f_5 = 2445,45 Hz, f_6 = 3058,59 Hz)

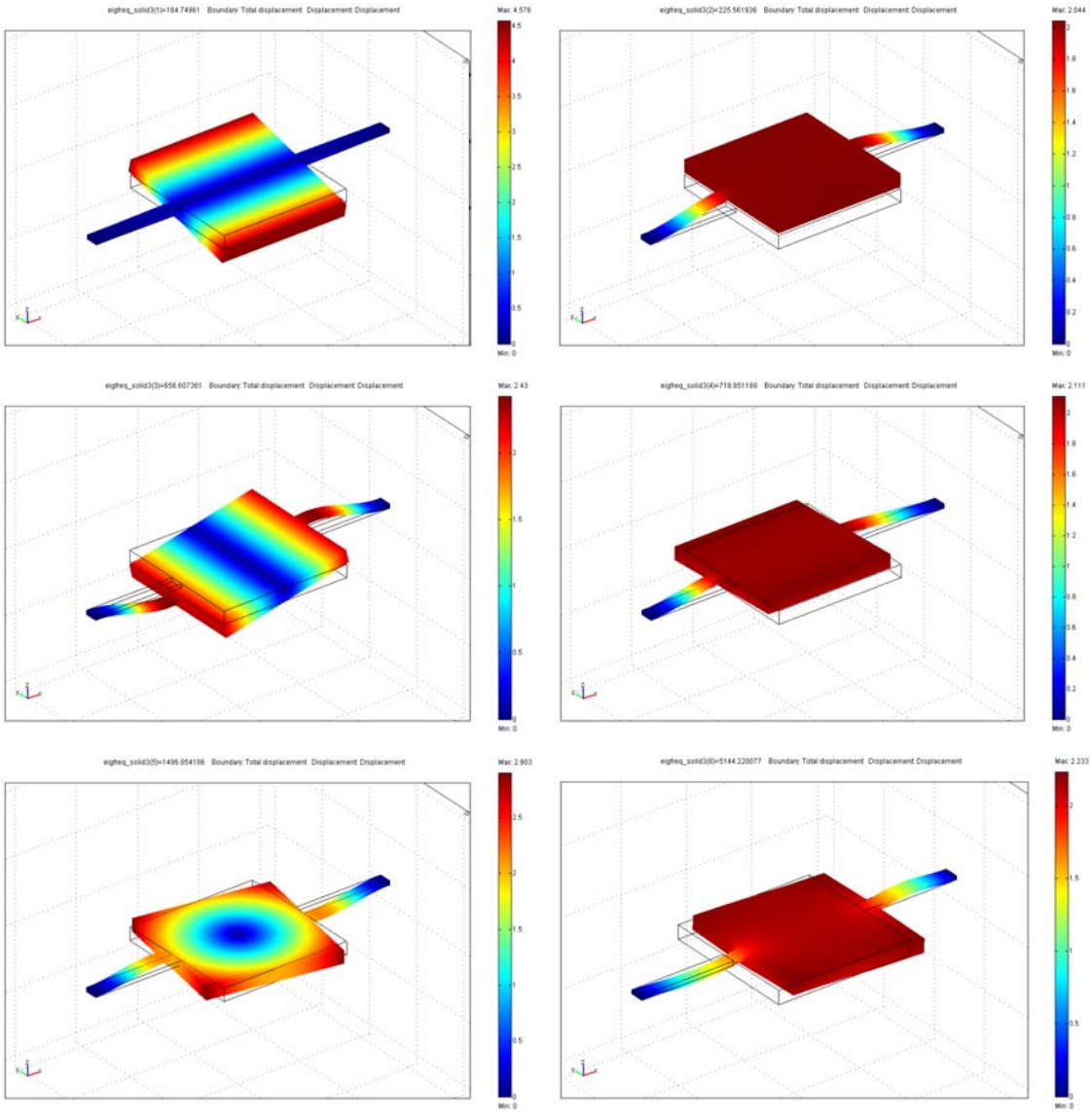

Figure 2-8 The first six eigenfrequencies and corresponding mode shapes of the torsional scanner.

(f_1 = 184.56 Hz, f_2 = 225.49,24, f_3 =656.34 Hz, f_4 = 718.89 Hz, f_5 = 1496.91 Hz, f_6 = 5144.22 Hz)

2.4 Second Order System Dynamics

The dynamic response of the scanner can be modeled by a simple linear oscillator. The equation of motion (EOM) is described by

$$m\ddot{x} + b\dot{x} + kx = F(t) \tag{2-41}$$

where m is the mass, b is the damping, k is the stiffness, x is the position and F is the force. Similarly, the EOM for a rotational system is described by

$$J\ddot{\phi} + b_{\phi}\dot{\phi} + k_{\phi}\phi = T(t) \tag{2-42}$$

where J is the polar moment of inertia, b_{ϕ} is the angular damping, k_{ϕ} is the angular stiffness, ϕ is the angular position and T is the driving torque.

For the torsional scanner, J is given by (2-37); k_{ϕ} is given by (2-16) and b_{ϕ} is given by

$$b_{\phi} = \sqrt{J \cdot k_{\phi} / Q} \tag{2-43}$$

where Q is the quality factor of the scanner. For the torsional scanner with the dimensions and the material properties given in Table 2-2, $k_{\phi} = 1.36 \times 10^{-3}$ N·m/rad, $J = 1.01 \times 10^{-9}$ kg·m^2 and $b_{\phi} = 1.17 \times 10^{-7}$ N·m/rad^2 at a Q value of 100. Figure 2-9 shows the frequency response of the scanner, *at* Q values of $Q = 0.7$, $Q = 3$, $Q = 10$, $Q = 100$. It is evident from the figure that quality factor defines the sharpness of the resonance peak.

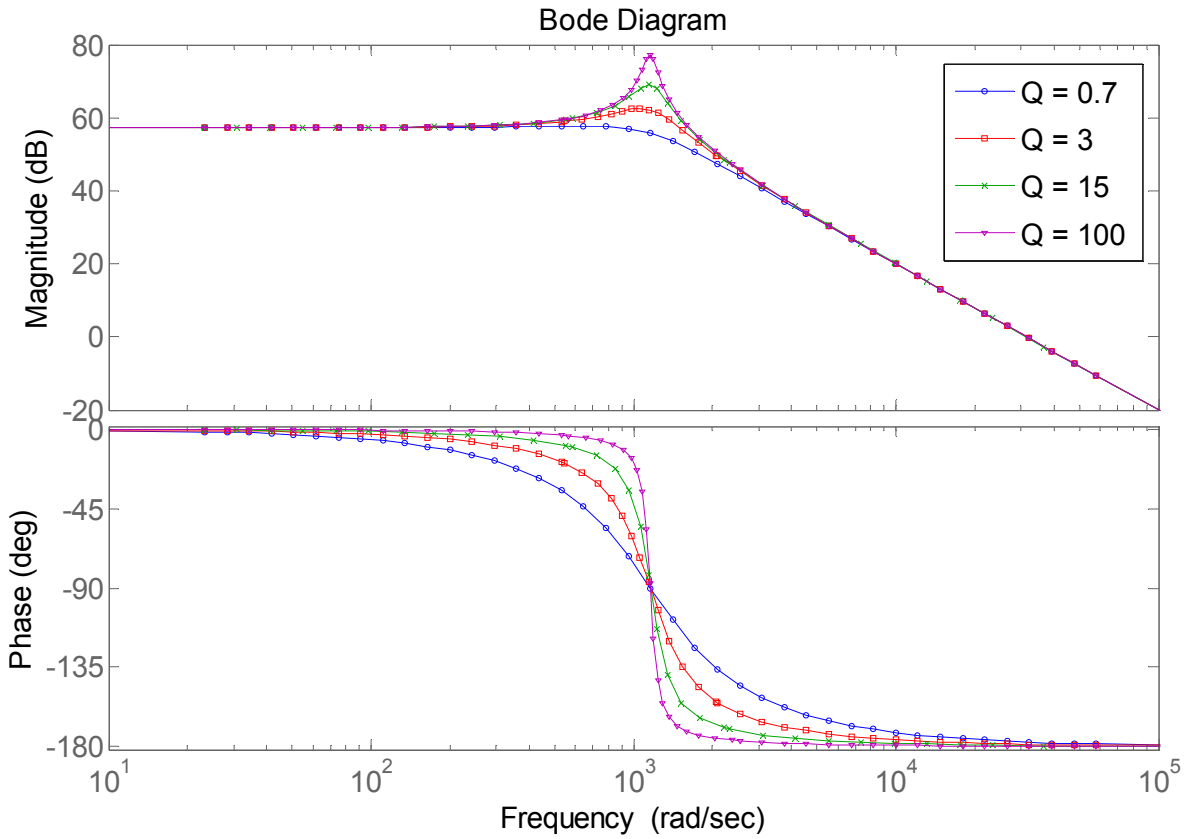

Figure 2-9 The frequency response of the torsional scanner *at Q = 0.7, Q = 3, Q = 15, Q = 100.*

3 MAGNETIC ACTUATION

This chapter discusses the magnetic materials and magnetic actuation methods. To understand the basics of magnetic actuation, magnetic materials must be studied first. The magnetization of matter is reviewed in 3.1. Section 3.2 focuses on magnetic materials and describes hard and soft magnetic materials and reviews their basic properties. Magnetic actuation is treated in detail in 3.3. Magnetic force and torque equations are derived assuming a magnetic field generated by an electromagnet. In 3.4 analytical modeling of a single turn coil and FEM of a multi turn coil is presented. Lastly the finite element magnetic field simulations are compared to the experimental magnetic field measurements.

3.1 Review of Magnetization of Matter

All materials are made up of atoms according to the elementary atomic model of matter. Each atom contains a positively charged nucleus and a number of negatively charged orbiting electrons. Circulating currents are generated by the orbiting electrons forming microscopic magnetic dipoles. In addition to this, spinning positively charged nucleus and negatively charged electrons form magnetic dipole moments [35].

In the absence of a magnetic field, the magnetic dipoles of the atoms have random orientation (except hard magnetic materials) resulting in no net magnetic moment. When an external magnetic field, H is applied to the material, the response of the material is called magnetic induction or magnetic flux density, B. The relationship between B and H is a property of the material and caused by the alignment of the magnetic moments of the spinning electrons and a change in orbital motion of electrons. The equation relating B and H is

$$B = \mu_0 (H + M) \tag{3-1}$$

where $\mu_0 = 4\pi \times 10^{-7}$ is the permeability of free space and M is the magnetization. The units of M and H are *A/m*, B is *Tesla* and those of μ_0 is *Weber/A·m*, also known as *Henry/m*. In some materials and in free space, B is a linear function of H; in some others B is not a single valued function of H. The magnetization is defined to be the magnetic moment per unit volume.

$$M = m/V \tag{3-2}$$

where m is the magnetic moment and V is the volume of the material. M is a property of the material and it depends on both the magnetic moments of atoms, ions, molecules making up the material and their interaction with each other [36][37]. The magnetization, M is related to the magnetic field intensity, H by

$$M = \chi H \tag{3-3}$$

where χ is the susceptibility. Substituting (3-3) in (3-1) gives the following relation

$$B = \mu_0(1+\chi)H = \mu_0\mu_r H = \mu H \tag{3-4}$$

where

$$\mu_r = 1 + \chi \tag{3-5}$$

known as the relative permeability of the material. A material is classified as:

- Diamagnetic, if $\mu_r \sim< 1$
- Paramagnetic, if $\mu_r \sim> 1$
- Ferromagnetic, if $\mu_r >> 1$.

The B-H curves of paramagnetic and diamagnetic materials are linear. For paramagnets relative permeability is slightly greater than unity and for diamagnets relative permeability is slightly less than

unity. Ferromagnets have a different B-H curve showing a phenomenon called hysteresis. They are treated in detail in the next section.

3.2 Review of Ferromagnetic Materials

The magnetization of a ferromagnetic material can be many orders of magnitude greater than that of paramagnetic materials. Secondly, the magnetization saturates above a certain magnetic field. Susceptibility, χ and relative permeability, μ_r are large and positive and they are functions of the applied field. Furthermore, the magnetization does not go to zero when the applied field goes to zero. These phenomenas of magnetization are known as the hysteresis. The graph of *B* versus *H* is called the hysteresis loop or the *B*-*H* loop.

Figure 3-1 shows a typical hysteresis loop for a ferromagnet.

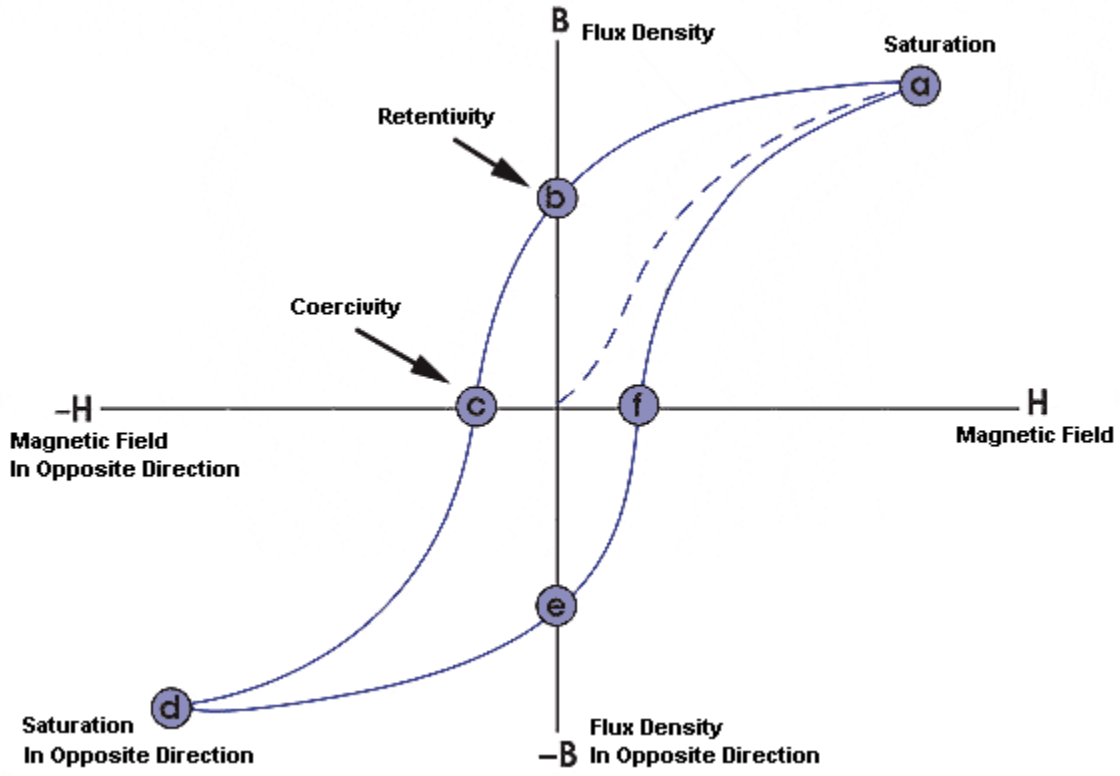

Figure 3-1 Hysteresis loop for a ferromagnet.

The magnetic material starts from an unmagnetized state at the origin. When the applied field is increased in the positive direction it follows the dashed curve till the saturation, (point a). The value of B at saturation is called saturation magnetic flux density, B_s. At this point magnetization saturates but magnetic flux density continues to increase with the increasing applied magnetic field, as evident from Eq. (3-1).

If the applied field, H is reduced to zero after saturation, B goes to B_r, residual induction or retentivity (point b). The inverse magnetic field needed to reduce the magnetic flux density to zero is called coercivity, H_c (point c). Depending on their coercivity, magnetic materials can be classified as hard and soft magnetic materials. When the magnetic field is increased further in the reverse direction, it reaches saturation in the reverse direction (point d). Then it shows the same effects in the reverse direction as the magnetic field is decreased and increased in the initial direction again (points e and f). When the magnetic field is swept like this, the hysteresis loop is obtained. The origins of hysteresis can be found in references [35][36][38][37].

3.2.1 *Hard Magnetic Materials*

Hard magnetic materials can not be magnetized and demagnetized easily. In other ways of saying, they have broad hysteresis loops (Figure 3-2). They have large coercivity values, so demagnetizing them requires very high magnetic fields. They are useful as permanent magnets. They remain in one persistent direction until a large field is applied in the other direction. The energy stored per unit volume in the external magnetic field should be as large as possible since this is the energy to do work. This energy corresponds to the maximum value of the product of B and H in the second quadrant of the hysteresis loop which is denoted as $(BH)_{max}$. Some actuation schemes can make use of the properties of hard magnetic materials.

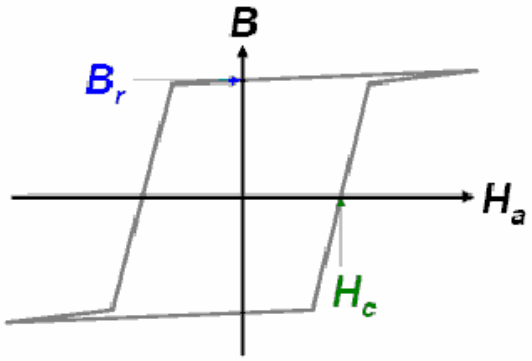

Figure 3-2 Hysteresis loop of a hard magnetic material.

3.2.2 *Soft Magnetic Materials*

Soft magnetic materials can be magnetized and demagnetized easily. Hence, they need relatively low magnetic fields. In other ways of saying, they have narrow hysteresis loops (Figure 3-3). The hysteresis loop of soft magnetic materials has small area. So they are suitable for applications where repeated cycles of magnetization and demagnetization occur as in electric motors, inductors, transformers. Some actuation schemes can make use of the properties of soft magnetic materials. $Ni_{80}Fe_{20}$ is chosen in this work because of its low coercivity, narrow hysteresis loop, very large permeability and relatively large saturation magnetization. Another important advantage of $Ni_{80}Fe_{20}$ is that it can be deposited easily onto the structures.

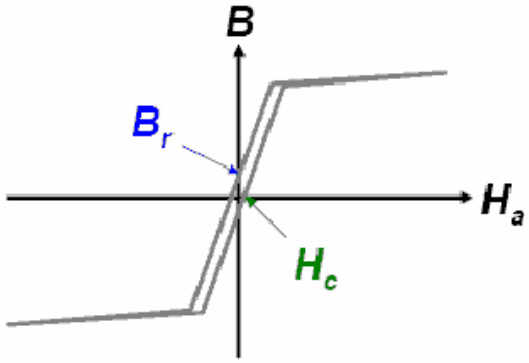

Figure 3-3 Hysteresis loop of a soft magnetic material.

3.2.3 *Magnetic Anisotropy*

The magnetic properties of a sample depend on the direction in which they are measured. This is a result of the magnetic anisotropy. Magnetic anisotropy is an important factor in determining the suitability of a material in a particular application.

In both hard and soft magnetic materials, there are certain directions along which the magnetization prefers to orient itself or tries to avoid. The preferred direction is called *easy axis* and the avoided direction is called *hard axis*. The magnitude of the magnetic field required to reach saturation along the hard axis is much larger than the magnitude of the magnetic field required to reach saturation along the easy axis. Figure 3-4 shows the hysteresis loop of a magnetic sample along the easy and hard axes. The directions of the easy and hard axes are determined by the magnetic anisotropy of a sample.

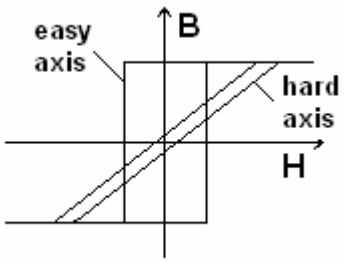

Figure 3-4 Hysteresis loop of a magnetic sample along the easy and hard axes.

In an ideal hard magnetic material the magnetization vector does not change in magnitude and it does not rotate away from the easy axis. But in an actual magnetic material the magnetization vector can rotate away from its initial preferred position. The rotation angle of the magnetization vector is determined by the magnetic anisotropy energy. Magnetic anisotropy energy which is minimum at the easy axis depends on the material properties and sample geometry.

The magnetic anisotropy energy is zero when the magnetization vector lies at the easy axis. Moving away from the easy axis, magnetic anisotropy energy increases till it is 90 degrees away from the easy axis reaching a maximum value at the hard axis. This explanation is valid for a uniaxial magnetic sample. In real life magnetic samples may have more than one easy axis. Going away from

the hard axis magnetic anisotropy energy starts to decrease, reaching zero at the easy axis pointing at the other direction. Magnetic anisotropy energy is given by

$$U_a = VK \sin^2 \theta \tag{3-6}$$

where U_a is the magnetic anisotropy energy, V is the volume of the sample, K is the magnetic anisotropy constant, and θ is the rotation angle of the magnetization vector [19].

There are different sources of magnetic anisotropy. Crystalline anisotropy, induced anisotropy, stress anisotropy and shape anisotropy are the most important ones:

- Crystalline anisotropy:

  Crystalline anisotropy is the tendency of the magnetization to align itself along a preferred crystallographic direction.

- Induced anisotropy:

  Induced anisotropy is not intrinsic to the material. It is produced by a treatment such as annealing which has directional characteristics. Using such treatments material properties can be engineered and magnitude of anisotropy and the easy axis can be altered considerably.

- Stress anisotropy:

  Stress anisotropy is the change in magnetization when there is change in mechanical strain of the magnetic material. Through magnetostriction, the stress in a magnetic material induces a magnetic anisotropy.

- Shape anisotropy:

  Along all the sources of magnetic anisotropy, shape anisotropy is the easiest to control and it can be orders of magnitude larger than the others. It is the tendency of the magnetization to align itself along the longest axis. In order to understand the origin of the shape anisotropy the demagnetizing field must be introduced.

Demagnetizing Field and Shape Anisotropy:

To understand the demagnetizing field, let's assume that a magnetic field, H_a is applied to a magnetic sample like shown in Figure 3-5; so the sample is magnetized from left to right, in the direction of the field. By definition, magnetic field lines radiate from the north pole (from right end) to the south pole (to left end) of the sample. Inside of the material the magnetic field lines radiate from the north pole to the right pole as well, opposing the applied magnetic field. This internal magnetic field tends to decrease the magnetization, demagnetizing the material. So this field is called the demagnetizing field.

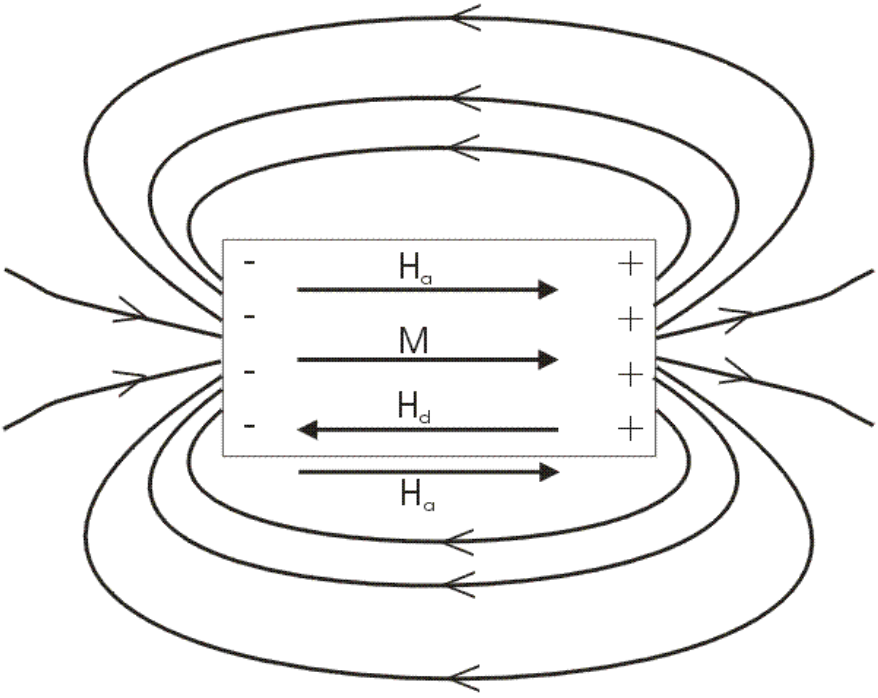

Figure 3-5 A sample magnetized by an applied field.

The demagnetizing field is formed by the magnetization so demagnetizing field along a particular axis $H_{dx,y,z}$ is proportional to the magnetization parallel to that axis $M_{x,y,z}$.

$$H_{d_{x,y,z}} = -\frac{N_{d_{x,y,z}}}{\mu_0} M_{x,y,z} \tag{3-7}$$

where $N_{dx,y,z}$ is the demagnetizing factor along a particular axis and it depends on the shape of the sample.

For elongated samples N_d is smallest along the long axis and largest along the short axis. The anisotropy increases with the increasing aspect ratio. Furthermore, the total field inside of the material is the sum of the applied magnetic field and demagnetizing field. As demagnetizing field opposes the applied field it must be subtracted from the applied field.

$$H_i = H_a - H_d \tag{3-8}$$

Along the long axis H_i is close to H_a as the demagnetizing field is low (N_d is low → H_d is low). Along the short axis the demagnetizing field is large (N_d is large → H_d is large) so most of the applied field goes into overcoming the demagnetizing field. So it is easier to magnetize the sample along the long axis.

The demagnetizing factor (coefficient) along a particular axis, $N_{dx,y,z}$ can only be meaningfully defined for an ellipsoid with semi axes a, b and c. An ellipsoid has three shape coefficients: N_a, N_a, N_c. The sum of them is always unity. The calculation of these shape coefficients can be found in [19]. The plots of the results are given in APPENDIX C. The magnetostatic energy density related to the demagnetizing field of a sample is given by

$$u_{ms} = -\tfrac{1}{2} H_d M = \tfrac{1}{2} \frac{N_d M^2}{\mu_0} \tag{3-9}$$

If the magnetization, M of the ellipsoid makes an angle α with the a semi axis, β with the b semi axis, γ with the c semi axis, considering the component of M along each axis; the magnetostatic energy density and the overall shape anisotropy coefficient of the sample in the direction of M can be given by

$$u_{ms} = \tfrac{1}{2}\frac{M^2}{\mu_0} N_d = \tfrac{1}{2}\frac{M^2}{\mu_0}(N_a \cos^2\alpha + N_b \cos^2\beta + N_c \cos^2\gamma) \tag{3-10}$$

$$N_{d_M} = N_a \cos^2\alpha + N_b \cos^2\beta + N_c \cos^2\gamma \tag{3-11}$$

and the demagnetizing field in the direction of M can be found by

$$H_{d_m} = -\frac{M}{\mu_0} N_{d_M} = -\frac{M}{\mu_0}(N_a \cos^2\alpha + N_b \cos^2\beta + N_c \cos^2\gamma) \tag{3-12}$$

If the magnetic field is constrained in the x-y plane the magneto static energy density becomes

$$u_{ms(x,y)} = \tfrac{1}{2}\frac{M^2}{\mu_0}(N_a \cos^2\alpha + N_b \sin^2\alpha) \tag{3-13}$$

where $\gamma = \pi/2$ and $\cos\beta = \sin\alpha$. By substituting $\cos^2\alpha$ with $(1-\sin^2\alpha)$

$$u_{ms(x,y)} = \tfrac{1}{2}\frac{M^2}{\mu_0} N_a + \tfrac{1}{2}\frac{M^2}{\mu_0}(N_b - N_a)\sin^2\alpha \tag{3-14}$$

neglecting the constant term in (3-14) and renaming $\theta = \alpha$ gives

$$u_{ms(x,y)} = \tfrac{1}{2}\frac{M^2}{\mu_0}(N_b - N_a)\sin^2\theta = K_{a(shape)} \sin^2\theta \tag{3-15}$$

which is consistent with (3-6). The magnetic shape-anisotropy constans K is then given by

$$K_{a(shape)} = \frac{1}{2}\frac{M^2}{\mu_0}(N_b - N_a) \tag{3-16}$$

For the samples used in this work, shape anisotropy is the dominant anisoropy because of the high aspect ratio of the structures.

3.3 Magnetic Force and Actuation Methods

Magnetic actuators can be classified as moving coil actuators and moving magnetic material actuators depending on their moving parts. Moving magnetic material actuators can further be classified as moving hard magnetic material actuators and moving soft magnetic material actuator. In this section first magnetic torques and forces are discussed and then different actuation mechanisms are described.

3.3.1 *Magnetic Torques and Forces*

Forces and Torques on Magnetic Charges

There are pairs of complementary magnetic charges bound to magnetized materials that act as sources of *H* and *M* [19]. The existence of these magnetic charges can be derived from the Maxwell's equations.

$$\nabla \cdot B = \nabla \cdot (\mu_0 H + M) = \mu_0 \nabla \cdot H + \nabla \cdot M = 0 \tag{3-17}$$

$$-\nabla \cdot M = \mu_0 \nabla \cdot H = \eta_m \tag{3-18}$$

where η_m is the magnetic charge density. The total magnetic charge, φ can be calculated integrating η_m over volume *v*.

$$\varphi = \int_v \eta_m dv = MS \tag{3-19}$$

where S is the pole surface and M is the magnetization.

When a magnetic field is applied on a magnetic pole, a force F is induced on the magnetic pole given by

$$F = \varphi H = MSH \tag{3-20}$$

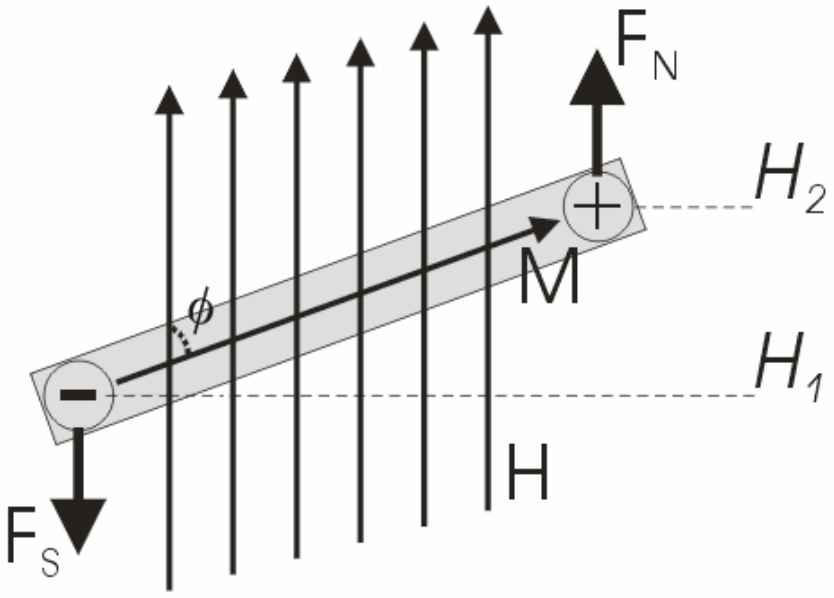

Figure 3-6 If the magnetic material is placed at an angle, ϕ to the magnetic field; a torque, T is generated.

When a magnetic material with constant magnetization is placed inside a uniform magnetic field (i.e., $H_1 = H_2$), the poles experience equal forces but in opposite directions. So they cancel out each other resulting in no net force. Likewise if the material is parallel to (i.e. aligned with) the magnetic

field lines, the torque is zero. If the magnetic material is placed at an angle, ϕ to the magnetic field (Figure 3-6); a torque, T is generated given by

$$T = \varphi Hl \sin\phi = MHV \sin\phi \tag{3-21}$$

where l is the length and V is the volume of the sample. The corresponding magnetostatic energy is given by

$$U_{ms} = -VH \cdot M = -VHM \cos\phi \tag{3-22}$$

Thus, when the torque is minimum magnetostatic energy is maximum and vice versa. The torque T, can be found by taking the derivative of the magnetostatic energy with respect to the angular variable, ϕ.

$$T = -\frac{dU_{ms}}{d\phi} = VHM \sin\phi \tag{3–23}$$

Magnetic Anisotropy Torque

The magnetic anisotropy energy, given in (3-16), increases as the magnetization vector moves away from the easy axis. A magnetic restoring torque is generated as a result and tries to realign the magnetization vector with the easy axis:

$$T = -\frac{dU_a}{d\theta} = -2VK \sin\theta\cos\theta = -VK \sin 2\theta \tag{3-25}$$

From (3-25) we see that the restoring torque is maximum at $\theta = \pm\pi/4$.

Lorentz Force

A conductor of length l in a magnetic field density, B experiences a force called the Lorentz force when a current I flows through it. This force is given by

$$F=I(l\times B) \tag{3-26}$$

This force is maximum when the applied field is perpendicular to the conductor through which the current flows.

3.3.2 *Moving Coil Actuators*

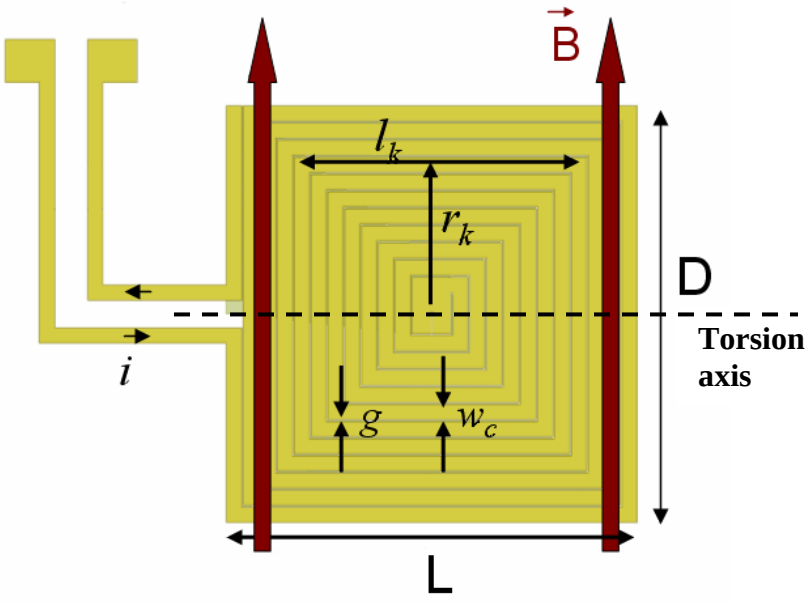

Figure 3-7 A moving coil actuator. For simplicity the torsion bars are not shown.

A moving coil magnetic actuator uses Lorentz forces for actuation [4]. Figure 3-7 illustrates a magnetic torsional actuator used as a microscanner. This kind of devices requires the guiding of the

current lines on the actuator. Lorentz force causes the springs to move in the magnetic field of an external source such as a magnet. The force acting on a single coil is given by

$$F = B_{\perp} I l_k \tag{3-27}$$

where $B\perp$ is the perpendicular component of magnetic flux density to the coil, I is the current passing through the coil and l_k is the length of the k^{th} coil. The torque is found by multiplying the force with the distance of the coil from the torsional axis, r_k. To find the total torque the torque of every coil must be summed.

$$T_{total} = 2\sum_{k=1}^{n} B_{\perp} I l_k r_k \tag{3-28}$$

where n is the number of coils.

The current on the moving coils may cause thermally induced problems such as bending or buckling of the thin structures. Moreover, in order to obtain a high magnetic field, large magnets are needed. Their size, long-term durability and environmental sensitivity (magnetization, Curie temperature) could be the problems associated with this kind of actuators.

3.3.3 *Moving Hard Magnetic Material Actuators*

The magnetization vector of a hard magnetic material does not change in magnitude or direction under the operating conditions. These materials can make use of the forces and torques as described in 3.3.1 . If the magnetization vector is not aligned with the magnetic field, a torque given by (3-21) is generated as in Figure 3-6.

On the other hand translational forces are also possible with this kind of actuators. If the magnetic field has a rate of change with respect to a displacement, the magnetic force is given by [21][22][41]

$$F_{x,y,z} = M_{x,y,z} \int \frac{d}{d(x,y,z)} H_{x,y,z} dv \tag{3-29}$$

where $M_{x,y,z}$ is the magnetization along the axis x or y or z and $H_{x,y,z}$ is the applied field along the same axis. The derivative is taken with respect to the same displacement variable and integration is performed over the entire volume. (Figure 3-8)

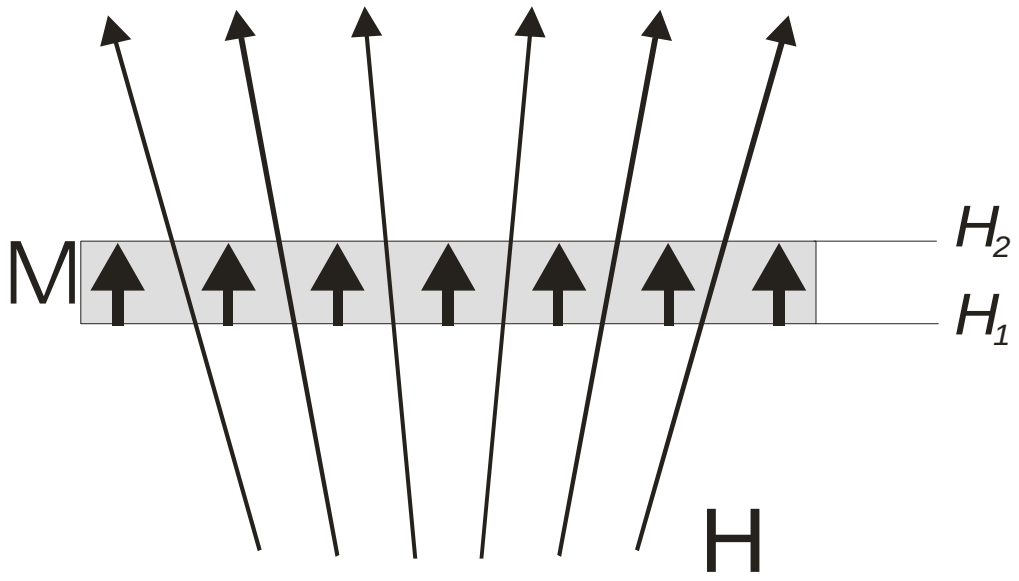

Figure 3-8 Moving hard magnetic material actuator. If the magnetic field has a rate of change with respect to a displacement (i.e., H_2 is not equal to H_1), a magnetic force is produced. The direction of magnetization is normal to the surface and it does not change with the applied magnetic field. If $H_2 > H_1$ F is upwards and vice versa.

This force can be bidirectional since the magnetization vector does not rotate. By changing the direction of the applied field the direction of the force can be altered. An important thing to point out is that the force is not maximum where the magnitude of the applied field is maximum. The force reaches maximum at the point the gradient of the magnetic field is maximum. This is usually different than the location of the maximum magnetic field.

3.3.4 *Moving Soft Magnetic Material Actuators*

Let's assume a uniform magnetic field, H_a is applied to a magnetic sample with magnetization M and magnetic anisotropy K. The initial angle between the applied field and the easy axis of the magnetic sample is γ. The applied field exerts a torque, T_{field} on the magnetization vector given by (3-30) and the anisotropy opposes this with a restoring torque, T_{anis} given by (3-31).

$$T_{field} = VHM \sin(\gamma - \theta - \phi) \tag{3-30}$$

$$T_{anis} = -VK \sin 2\theta \tag{3-31}$$

where θ is the angle between the magnetization vector and the easy axis and ϕ is the angle of deflection of the material.

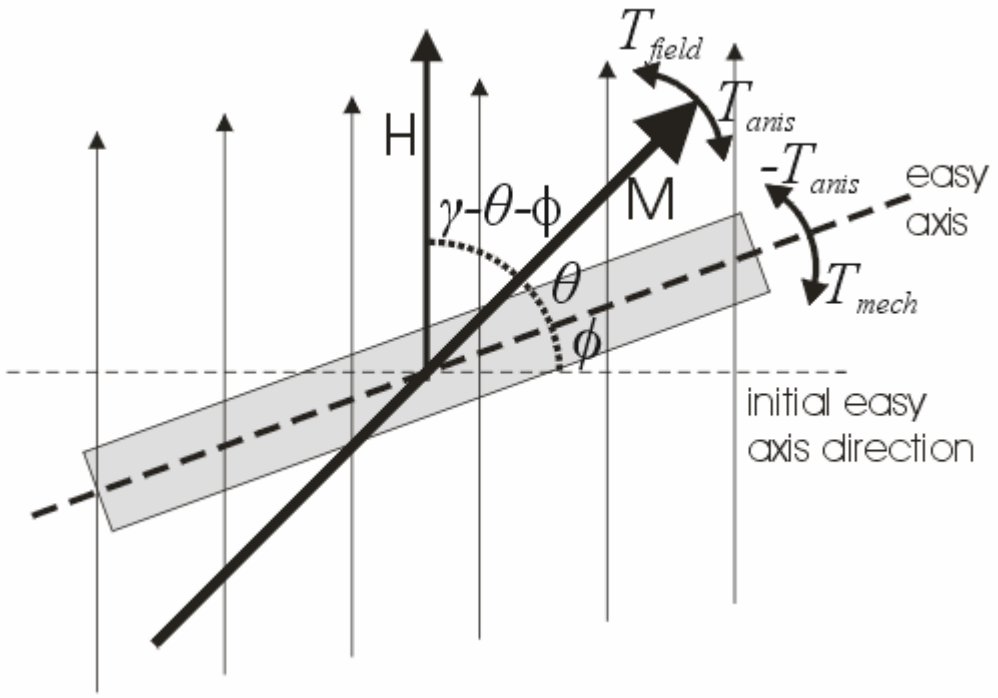

Figure 3-9 Moving soft magnetic material actuator.

The magnetic sample starts to deflect because of the restoring anisotropy torque, T_{anis}. A mechanical torque, T_{mech} this time oppose this torque.

$$T_{mech} = -k_{\phi}\phi \tag{3-32}$$

where ϕ is the angle of deflection and k_{ϕ} is the angular stiffness calculated in 2.2. In equilibrium the net torque on the magnetization vector and the net torque on the magnetic sample is zero.

$$T_{field} + T_{anis} = 0 \tag{3-33}$$

$$-T_{anis} + T_{mech} = 0 \tag{3-34}$$

This implies that the magnitude of T_{field}, T_{anis} *and* T_{mech} are all equal. Using equations (3-31), (3-32) and (3-34) angular mechanical deflection, ϕ can be solved.

$$\phi = \left(\frac{VK}{k_{\phi}}\right)\sin(2\theta) \tag{3-35}$$

Substituting (3-35) in (3-30) gives

$$T_{field} = VHM\sin\left(\gamma - \theta - \left(\frac{VK}{k_{\phi}}\right)\sin(2\theta)\right) \tag{3-36}$$

And substituting (3-36) and (3-31) in (3-33) gives

$$VK\sin(2\theta) = VHM\sin\left(\gamma - \theta - \left(\frac{VK}{k_{\phi}}\right)\sin(2\theta)\right) \tag{3-37}$$

(3-37) can be solved iteratively to obtain the angular mechanical deflection, ϕ and angular magnetization deflection, θ.

In reference [19] it was shown that for a magnetic sample with a length to thickness ratio of 4 the magnetization vector does not deflect very far from the easy axis ($\theta<2\ deg$). It is concluded that the calculated mechanical deflections of soft magnetic structures with large length to thickness ratios are very similar to the calculated mechanical deflections of structures modeled as ideal hard magnetic materials. So the structures with high length to thickness ratios can be modeled as ideal hard magnetic materials.

The soft magnetic material used for the structure given by Table 2-1 has dimensions of $l = 8\ mm$, $w = 8\ mm$ and $t = 28\ \mu m$. It has a length to thickness ratio of 285. Thus, for the scanners used in this work the dominant anisotropy is the shape anisotropy and the other sources of anisotropy can be neglected.

For all practical purposes we can assume that the magnetization vector of the structures used in this work does not deflect from the easy axis because of high shape anisotropy. In this case the magnetic torque, T_{field} can be simplified to

$$T_{field} = VMH\sin(\gamma - \phi) \tag{3-38}$$

and the mechanical restoring torque, T_{mech} is given by (3-32). As $T_{field} + T_{mech} = 0$, the equilibrium angular mechanical deflection can be found by

$$\phi = \left(\frac{VMH}{k_\phi}\right)\sin(\gamma - \phi) \tag{3-39}$$

3.4 Electromagnet Modeling

Magnetic actuators require external magnetic fields to function. Most of the actuators are excited with the help of electromagnets as they provide control of the applied field. An external permanent magnet can be used with moving coil actuator as the torque can be controlled by the coil current. For

moving magnet approaches (i.e, soft and hard magnetic material placed on the moving structure) an external electromagnet is needed to control the torque. This section focuses on the electromagnet modeling. All the scanners used in this work are actuated by external electromagnets.

3.4.1 *Single-Turn Coil Theory*

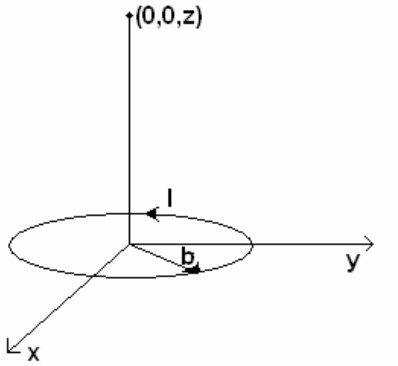

Figure 3-10 Circular coil carrying current, *I*.

The magnetic field generated by a circular coil can be calculated from the Biot-Savart law [35]. In Figure 3-10 the vertical (z) component of the magnetic field intensity at a point on the axis of a circular loop of radius b that carries a current I is given by

$$H(z) = \hat{a}_z \frac{I \cdot b^2}{2 \cdot \left(z^2 + b^2\right)^{\frac{3}{2}}} \tag{3-38}$$

To obtain the magnetic field of a coil with n turns, the contribution of each turn must be summed. General formulas giving the magnetic field at any point in space can be found in electromagnetic textbooks such as [35].

3.4.2 *FEM Analysis*

Theoretical calculations are useful for calculating magnetic fields of two dimensional coils (one or few layers) such as microfabricated coils on silicon wafers or coils on printed circuit boards. Analytical calculations are difficult to deal with for three dimensional coils winded on a core, such as the coils used in relay circuits and the coils used in this work. Finite element modeling provides easier and more effective results.

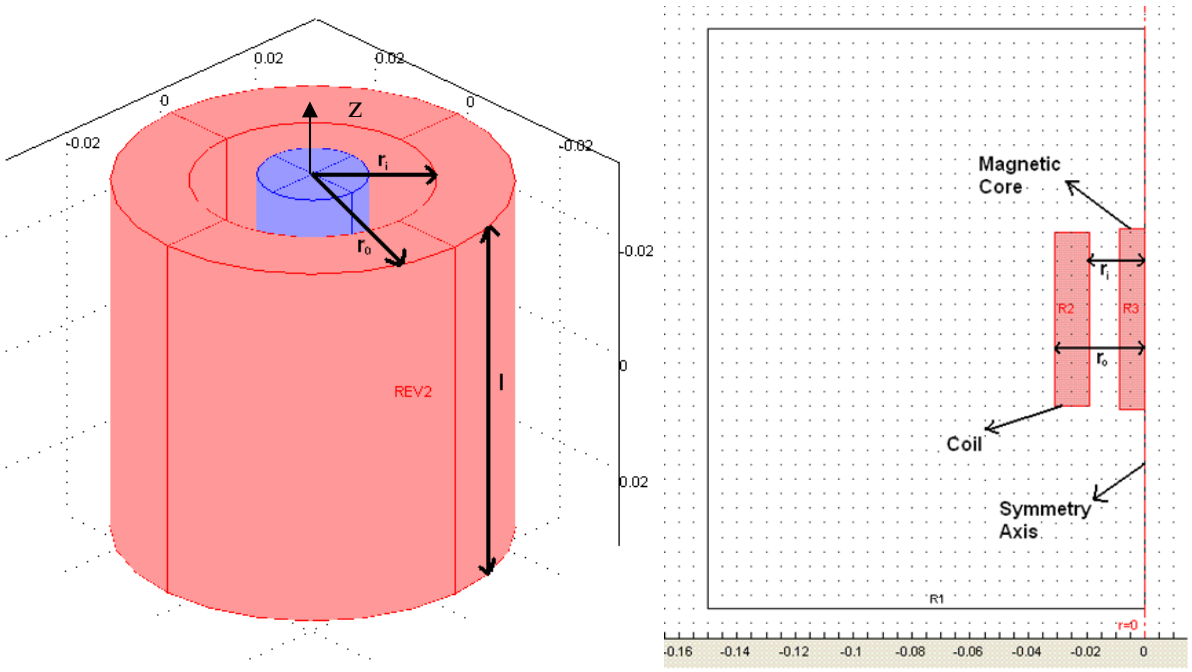

(a) (b)

Figure 3-11 The coil is modeled by an area penetrated by the current, *I* times the number of turns, *N*. A 2-D model with rotational symmetry is used. (a) 3-D representation of the model, and (b) 2-D model with rotational symmetry is shown.

Figure 3-11 illustrates an N turn coil with an inner radius of r_i , an outer radius of r_o, a length of l, and a magnetic core at its centre. The electromagnet is modeled using FEMLAB 3.1. Due to the computation time and number of element limitations of the software, a two dimensional model with

rotational symmetry is used. The coil is represented by an area penetrated by the current *I* times the number of turns *N*.

Static magnetic analysis is performed and the magnetic fields and flux densities generated by the coils are simulated for the different coils used throughout this work. Both the radial and the vertical components of the magnetic field are important as the generated torque depends on both. The radial component magnetizes the sample and the vertical component generates the torque on this magnetization. In Figure 3-12, the arrows show the magnetic flux density and the streamline shows the magnetic field when 0.5 Amperes were applied to the coil with the dimensions and properties given in Table 3-1.

Figure 3-13 shows the magnetic flux density generated by the coil when 0.5 Amperes were applied to the coil. The maximum magnetic flux density appears inside the core because of its high relative permeability. On the outside, the maximum magnetic flux density is obtained at the corners of the core. The blue line that is 1.5 mm above the core shows the line of points where magnetic measurements are taken and compared with the FEM simulations in the next section.

Inner radius	r_i	*18,75 mm*
Outer radius	r_o	*30,75 mm*
Radius of the core	r_{core}	*8,5 mm*
Length of the coil	l	*60 mm*
Length of the core	l_{core}	*62 mm*
Relative permeability	m_{ur}	*5000*
Number of turns	N	*1600*

Table 3-1 The material properties and dimensions of the coil with the magnetic core.

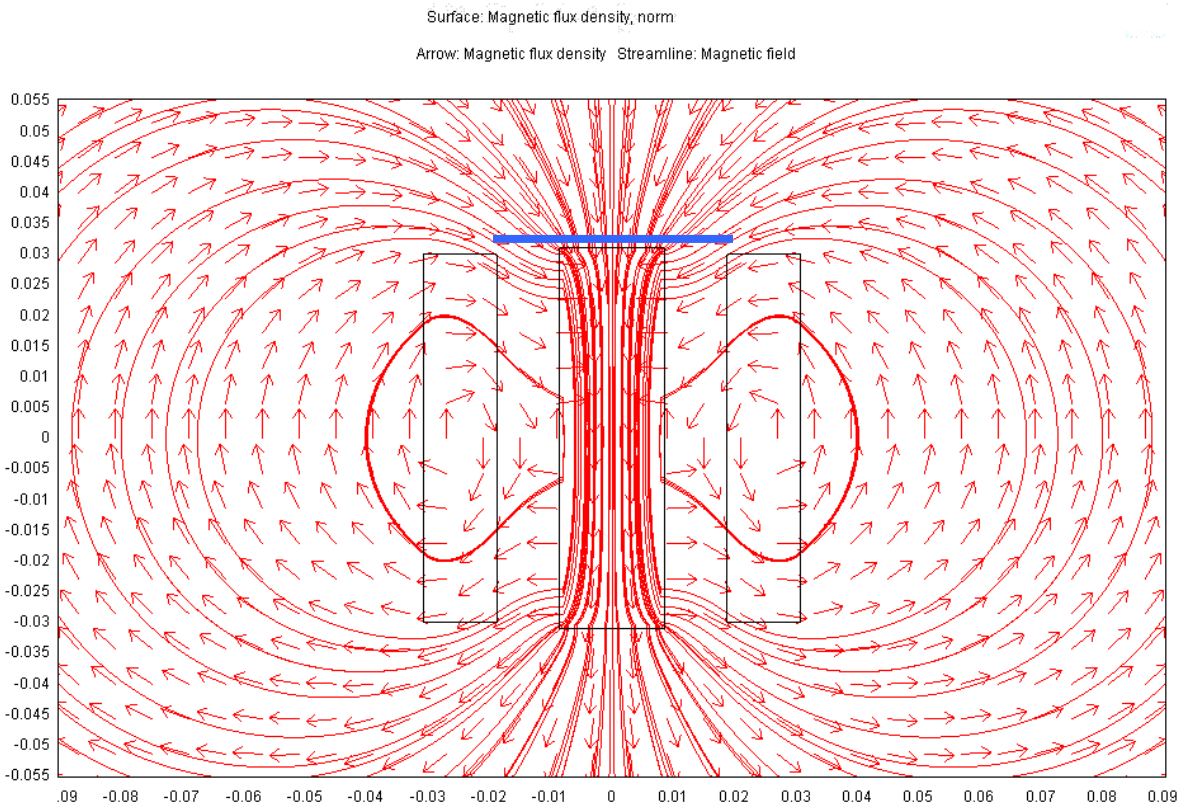

Figure 3-12 Cross section of the coil with the magnetic core. Magnetic field and magnetic flux density generated by the coil whose dimensions and properties are given in Table 3-1 are simulated. The arrows show the magnetic flux density and the streamline shows the magnetic field when 0.5 Amperes were applied to the coil.

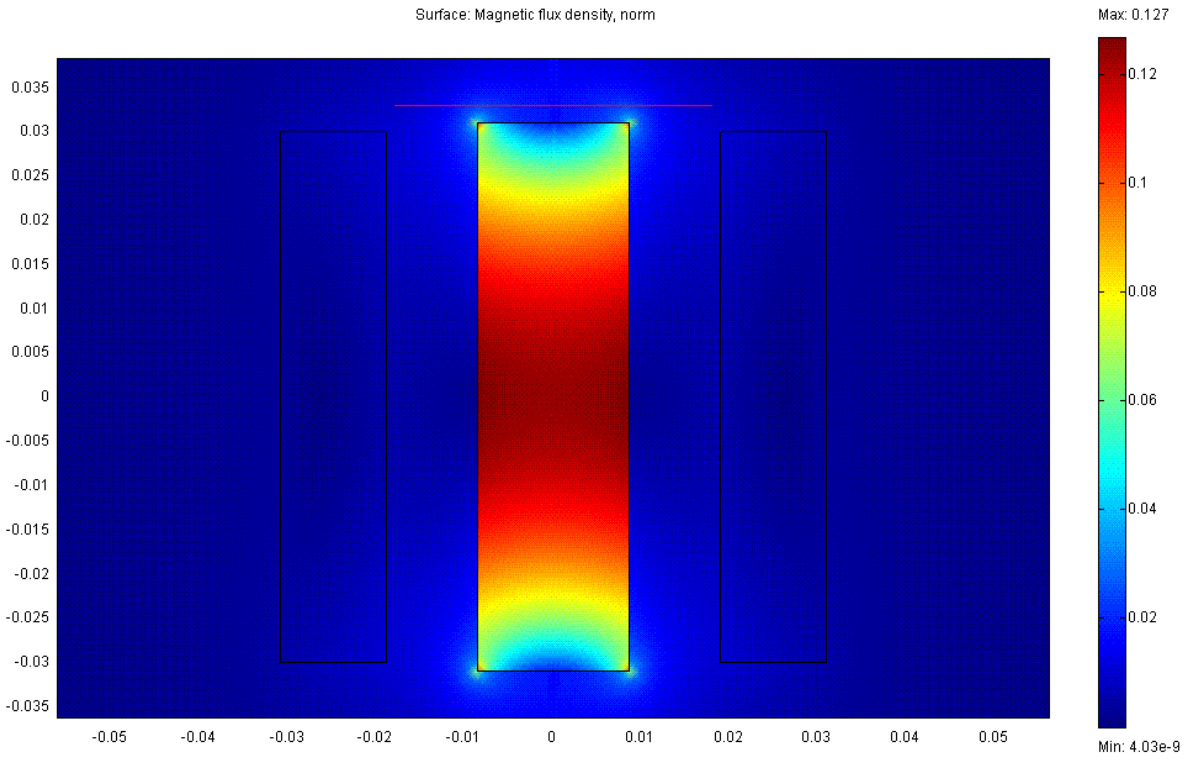

Figure 3-13 Cross section of the coil with the magnetic core. Magnetic flux density generated by the coil whose dimensions and properties are given in Table 3-1 is simulated. The maximum magnetic flux density appears inside the core because of its high relative permeability. Outside of the coil the maximum magnetic flux density is obtained at the corners of the core. The red line above the core shows the line of points where magnetic measurements are taken and compared with the FEM simulations.

3.4.3 *Experimental Results*

FEM results of 3.4.2 are confirmed experimentally using a Bell Probe to measure both the vertical and the radial components of the magnetic flux density. Measurements are taken at 1.5 mm away from the top surface of the coil along the line illustrated in Figure 3-13 with 0.25mm increments. Figure 3-14 and Figure 3-15 show the experimental and FEM simulation results for the vertical and the radial components of the magnetic flux density (B_z and B_r), respectively. The simulation and experimental results are in good agreement. Note that the maximum values of B_z and B_r are attained near the top of the coil wires but not exactly at the same position. Other coil geometries are also modeled using FEM in a similar way and the electromagnetic force and torque are computed using the equations developed throughout this chapter.

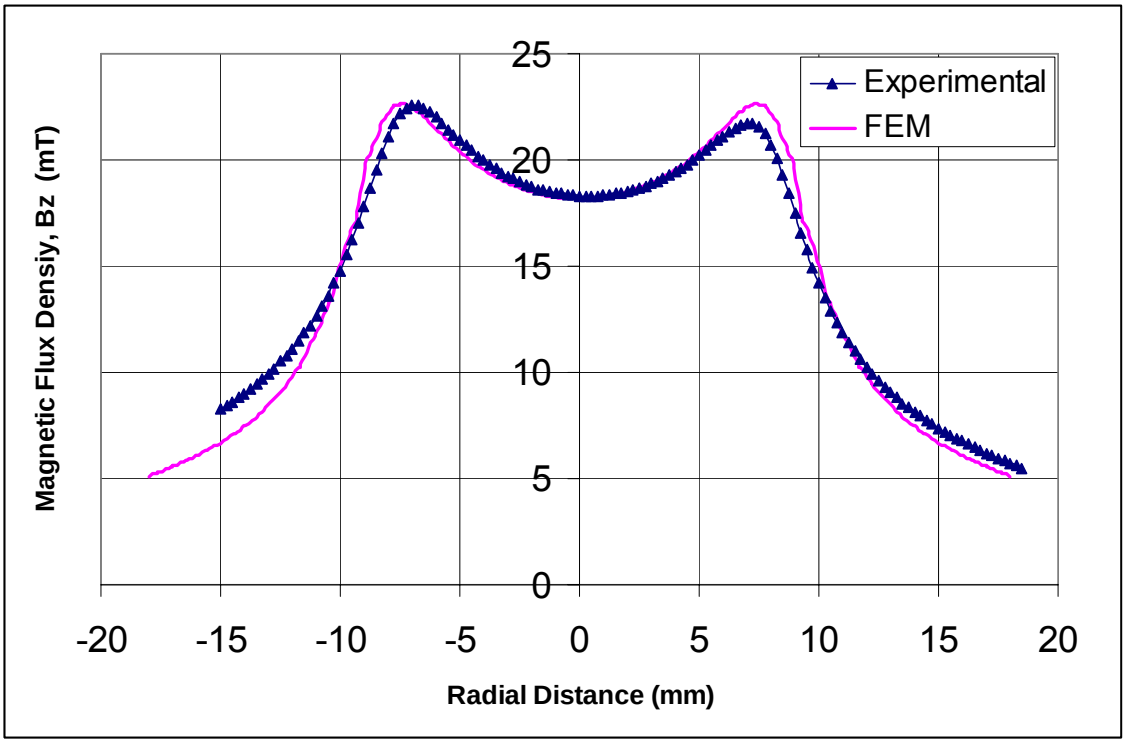

Figure 3-14 The experimental results and FEM simulation results for the vertical component of the magnetic flux density, B_z at different radial distances.

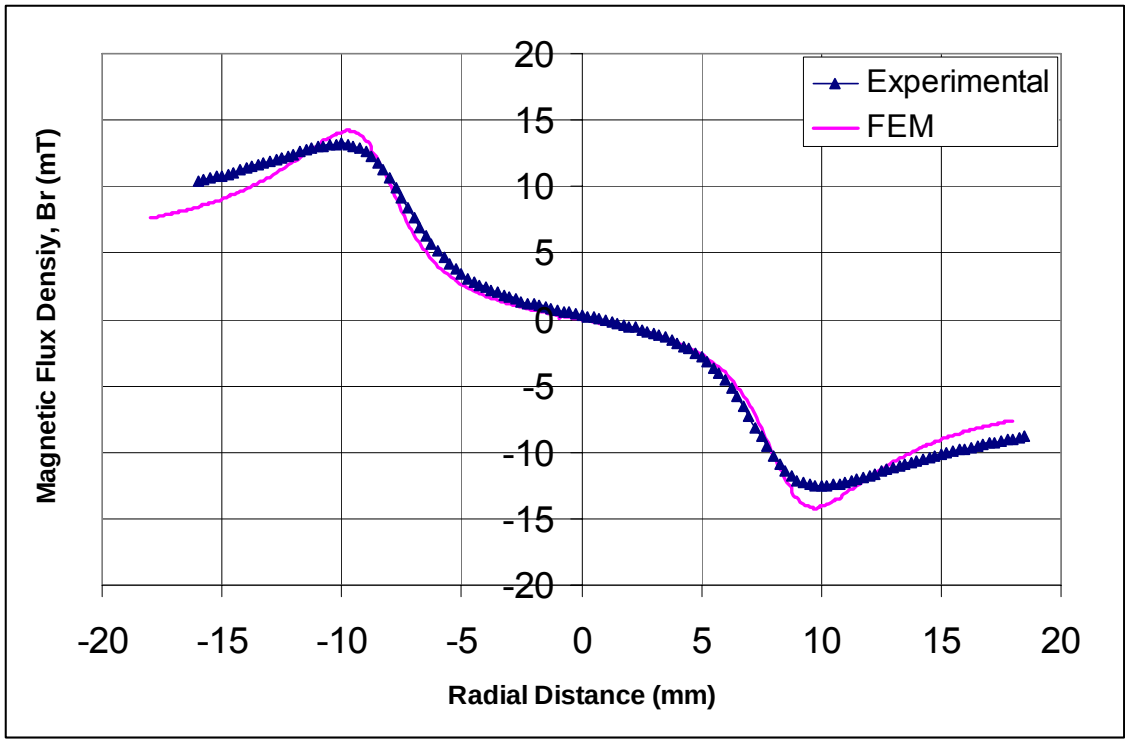

Figure 3-15 The experimental results and FEM simulation results for the radial component of the magnetic flux density, B_r at different radial distances.

4 FABRICATION AND MATERIAL CHARACTERIZATION

In this chapter the fabrication steps of the magnetic scanners are described in detail. As explained in the first chapter, one of the objectives of this work is developing simple and low cost scanners. In the scanner system, polymers are used as the structural material, magnetic powders mixed in the polymer and electroplated permalloy films are used together with external coils for magnetic force generation, and Aluminum (Al) coating layer or Al-coated Silicon mirrors embedded in the polymer are used to make the surface highly reflective.

Polymers are widely used in passive micro-optical elements and lend themselves to high-volume low-cost manufacturing and replication technologies such as molding. In this research we use polymers as a structural material in active mechanical scanning structures. The process developed is not only simple and well-known for many years but also does not require any lithography steps that complicate the fabrication. The molding procedure is explained in details in 4.1.

For the magnetic material, permalloy and some magnet powders were used. Permalloy was chosen because of its good magnetic properties and the easiness of producing thick layers of permalloy by electrodeposition. Adding magnetic powder to the polymer, i.e., making a polymer magnet does not require additional fabrication steps. This work does not focus on producing good quality polymer magnets but it shows that adding of magnetic powders is completely compatible with the molding process described here. Several authors showed that producing polymer magnets with good magnetic properties is possible [39][40][41].

In 4.2 another simple method for producing scanners is introduced. It involves using widely available epoxy–glass fiber composite boards and shaping them with conventional machinery. In 4.3 nickel iron electroplating process is described in detail and in 4.4 magnetic material characterization methods are discussed.

4.1 Molding

Figure 4-16 shows the basic fabrication steps for the photo sensitive polymers such as RenShape SL5195, which is used in stereo-lithography for rapid prototyping. The basic procedure does not change for other materials except some minor differences. RenShape SL5195 is a UV sensitive polymer, meaning that the liquid material becomes solid when it is exposed to UV light. The material properties of RenShape SL5195 are as given in APPENDIX A.

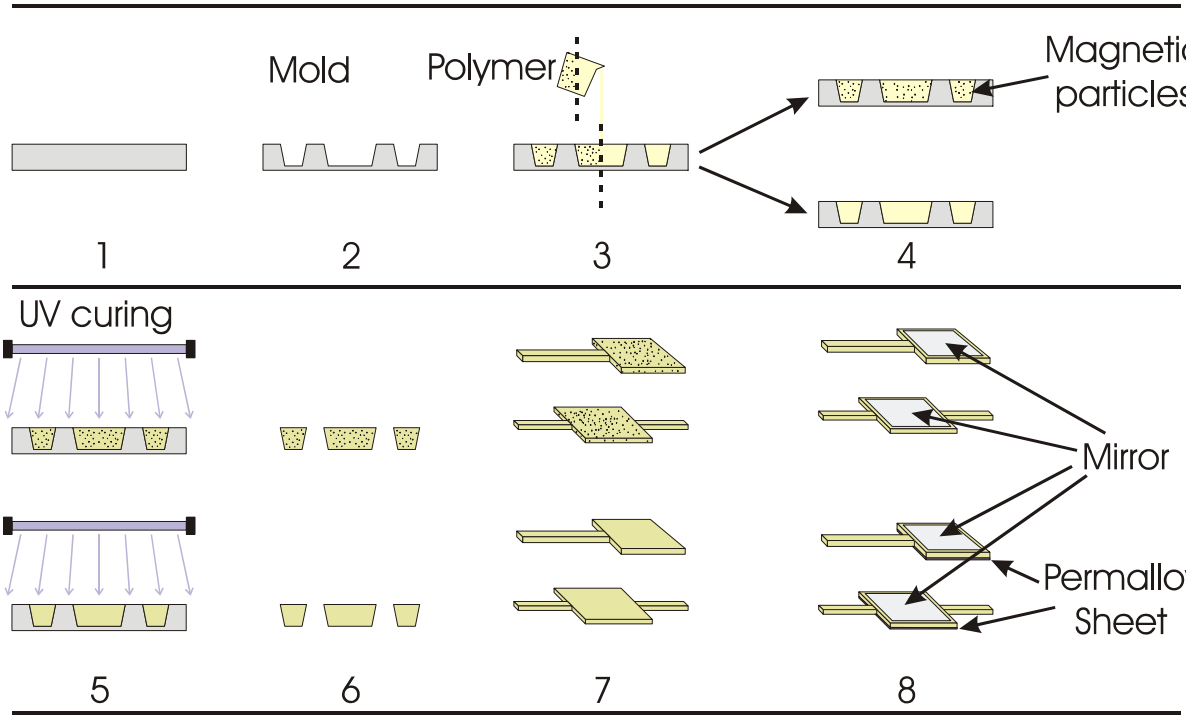

Figure 4-16 Basic fabrication steps for RenShape SL 5195 and other photo sensitive polymers.

Steps 1, 2 Preparation of the mold:

The first step involves the preparation of the mold, which is used repeatedly for replicating devices. Fabrication of the mold can involve conventional machining or lithography process depending on the desired tolerances.

For the prototypes, the mold is made out of an aluminum block. The designed shapes are realized by a CNC (Computer Numerical Control) machine. This process has few microns of sensitivity but the smallest feature size was limited to about 500 μm.

Figure 4-17 shows the aluminum mold prepared by the CNC machine. In future designs, silicon wafers can also be used as the mold. With anisotropic etching of silicon wafers, molds for smaller sized structures can be prepared.

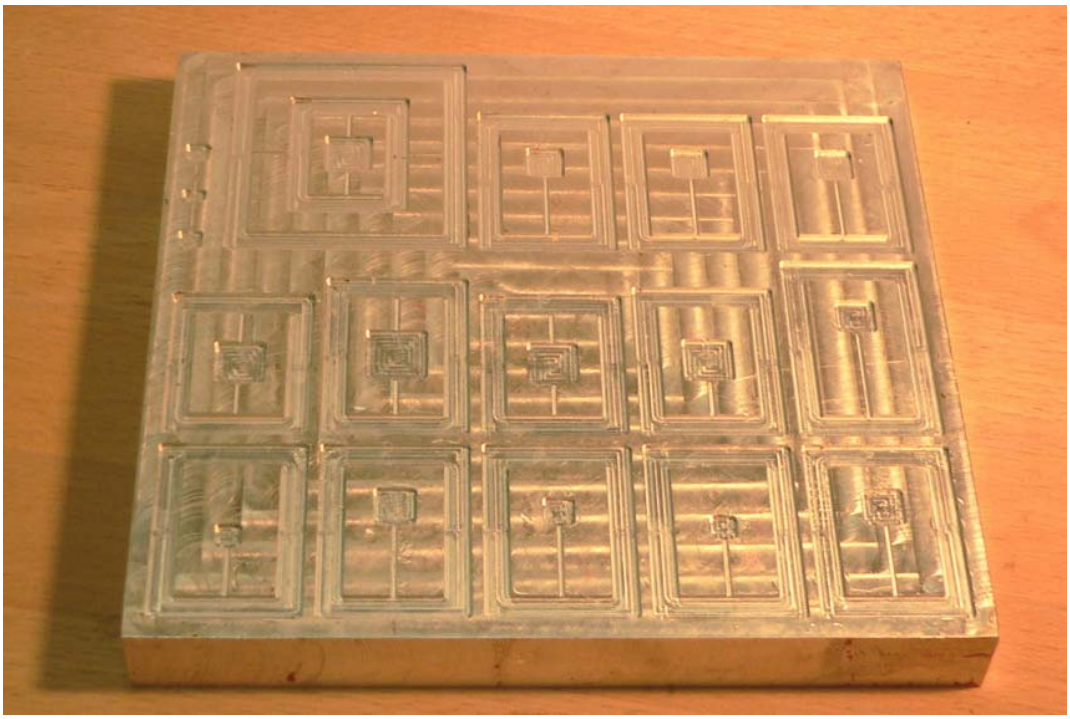

Figure 4-17 The mold used for the prototypes. It is made by CNC machining of an aluminum block.

Steps 3, 4 Injection of the liquid material to the mold:

In this step magnetic powder is mixed with the polymer and the mixture is injected to the mold. For the scanners with electroplated permalloy the polymer is injected to the mold without adding any magnetic powder.

Step 5 UV curing:

The liquid polymer or polymer - magnetic powder mixture is exposed to UV light until it is completely cured and becomes solid. Curing of the polymer magnetic powder mixture takes longer time as the powder decrease the transparency of the polymer. Curing the material that is at the bottom of the mold is more difficult, thus the thickness of the device and the magnetic powder concentration in the photo sensitive polymer is limited. Forming the device out of several layers put on each other or using a polymer with a different curing method can be solutions to this problem. Some polymers can be cured with addition of catalyzes, those can have higher density of magnetic material but takes longer to cure. The challenge with this process is maintaining the thickness of the device precisely and the prevention of air bubbles in the polymer while curing. The thickness is better controlled by placing a top cover glass and the bubble problem is eliminated by performing the curing in an enclosure while pumping dry nitrogen into the medium. A simple UV oven was built for the purpose using a picnic cooler that is covered with Aluminum foil for high reflectivity. A hole was opened to let Nitrogen into the cooler. The sample and the UV lamp are placed in the cooler during curing.

Steps 6, 7 Removing the devices out of the mold:

Before the last step the devices are removed out of the mold. Stiction was a major problem of this step. Some chemicals (fluorine and silicon based sprays) are used to avoid stiction. Before injection of the polymer, a thin layer of these chemicals are applied to the base of the mold and cleaning of the mold with acetone might be required.

Step 8 Attaching the mirror:

As the last step, a small mirror is attached to the scanner. The mirrors are prepared by evaporating aluminum onto a thin polished silicon wafer to make it highly reflective. Then, the wafer is diced into pieces with the desired dimensions to use as mirrors. The mirror can be covered with a protective tape or layer and placed at the bottom of the mold before the polymer is dispersed. Alternatively, it can be

glued on top of the polymer afterwards. At this step permalloy is also added to the scanner. The details of combining polymer with the permalloy is described in 4.1.2.

4.1.1 *Scanners with Magnetic Powder*

Different magnetic powders are used in prototype designs. Commercially available spherical magnetic powder (Magnequench MQP-S-9-8), nano sized Fe_2O_3 particles and high energy embedding powders (Hoosier Magnetics HEEP HM 180) are the powders used in the prototypes. The powders are mixed with RenShape SL5195 and other polymers. Mixtures are prepared in different concentrations with the help of an ultrasonic stirrer. The high energy embedding powder showed the best performance. As explained before when the concentration of the powder in the polymer is increased, the transparency of the UV sensitive polymer decreased. This caused problems in the curing step. To cope with this problem other polymers are also tried. Thermosetting polyester, which has a different curing method performed well in the experiments. The curing of polyester involves adding chemicals to the liquid polyester. In general, polyesters have extremely good mechanical properties and are extremely heat resistant. They allow for adding large concentrations of powder without any difficulty. These reasons make them a good candidate for the scanner. Other than polyester; polyimide, epoxy and polymethyl methacrylate (PMMA) are the materials suitable for this process. We did not focus on optimization of the polymer – magnetic powder mixture. But the compatibility of such mixtures with our proposed process was shown. Eventually, scanners with electroplated permalloy performed better at the experiments. But improving the quality of polymer - magnetic powder mixture may end up with better performing devices.

4.1.2 *Scanners with Electroplated Permalloy*

For the scanners with electroplated permalloy, the mixing of magnetic powder with polymer is omitted in the fabrication process. An electroplated permalloy is glued to the scanner along with the mirror. We tried electroplating permalloy directly on the polymer using a conductive seed layer. Copper was tried as a seed layer using the process developed for depositing copper on epoxy boards

for printed circuit boards (PCB). The adhesion of copper to the polymers tried was not good enough for our devices. However, the effort was still helpful and we developed another fabrication method using epoxy – glass fiber composite boards as described in 4.2.

Another method tried was plating on Silicon wafers and using diced Silicon pieces with Al mirror on one side and permalloy film on the other side. Using silicon microscanners with this method is another research project in our laboratory. However, we can place diced Silicon pieces in polymer to make molded microscanners. Silicon wafers have Titanium/Gold seed layers for permalloy film electrodeposition. The details of electrodeposition of permalloy is described in 4.3. Furthermore in some prototypes thin sheets of permalloy released from their base materials due to stress are also attached to the scanner.

4.2 Epoxy – Glass Fiber Composite Scanners

An alternative to molding for fabricating scanners is by shaping epoxy-glass fiber boards by conventional machining. Epoxy – glass fiber composite boards are widely used by printed circuit board (PCB) manufacturers. Boards with copper on its top and bottom surface are commercially available in a variety of thicknesses. The copper layer on the surface can be used as a seed layer for electrodeposition, making the fabrication process easier and simpler. Prototypes with thicknesses varying from 0.13 mm to 1 mm were prepared. They are cut by a computer controlled machine, forming the desired geometries. The limit of this method is that it does not allow thickness variations in the device. Cutting is done in 2-D allowing fixed thickness throughout the device.

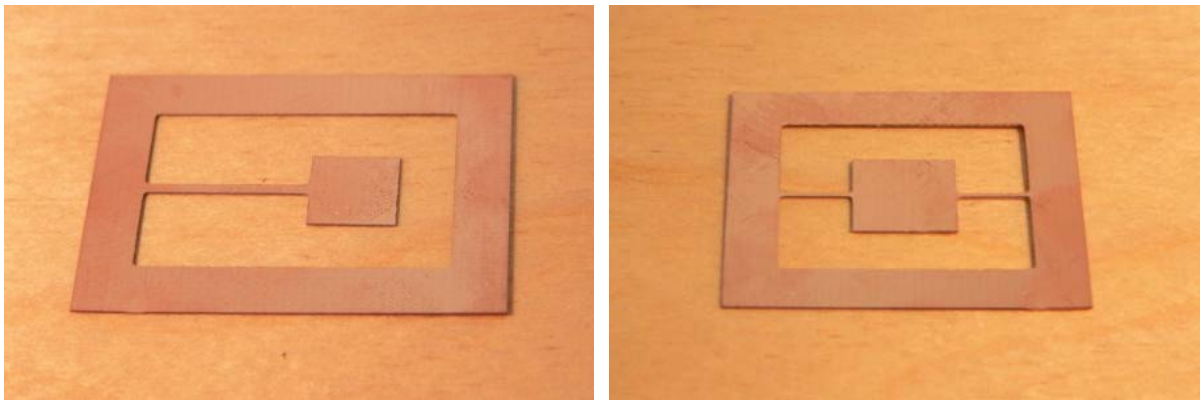

Figure 4-18 Epoxy – glass fiber scanners coated with copper are cut into desired shape by computer controlled machinery.

4.3 Electroplating

In section 4.1.1 preparation of the scanners with magnetic powder is described. The magnetic material (permalloy) for the second type of scanners is formed by electroplating. Magnetic materials can be deposited in a variety of ways. Thermal evaporation, sputtering and electroplating are the most important and frequently used methods. Among them electroplating is the only method that can be used to deposit thick films (> 10 μm). Electroplating of magnetic materials has been done for a long period of time. Maintaining a well-controlled plating bath and process requires not only good recipes but also a lot of expertise.

A typical electroplating bath consists of an aqueous metal solution, an anode, a cathode and a power supply (Figure 4-19). For NiFe electroplating the anode is made of nickel and the cathode is made of another conductive material where the deposition occurs. The aqueous solution contains nickel (Ni^{2+}) and iron (Fe^{2+}), hydrogen (H^{+}) and sulfate (SO_4^{2-}) ions. When a voltage is applied between the anode and cathode, the positively charged ions are attracted by the negatively charged cathode. The Ni and Fe ions reaching the cathode gain electrons and they become plated onto the cathode. At the same time the anode releases Ni ions to the aqueous solution that supply electrons to the power supply. There is no source for the Fe ions so after a while they are depleted. This is why the

bath has a limited life time. Hydrogen ions are also attracted by the cathode. When they reach the cathode they gain electrons and form H_2 bubbles. To avoid the formation of H_2 bubbles, the cathode is periodically removed from the solution for a short time [44].

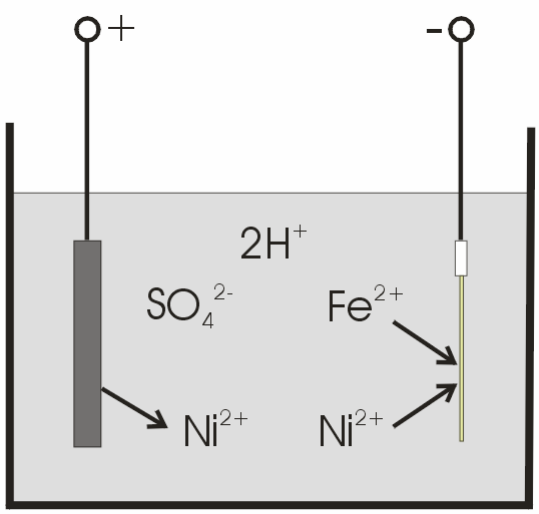

Figure 4-19 Typical electroplating bath

To deposit magnetic material, a conductive plating base or seed layer is needed as a cathode. As described in section 4.1.2 the attachment of magnetic material to the scanner is accomplished in two ways. For the epoxy – glass fiber composite scanners Cu, which is already found on the surface of the board, is used as a seed layer. A thick layer of photoresist is coated to the desired areas to define the shape of the plated material (Figure 4-24). After the electroplating process the photoresist is stripped. For the scanners with an attached silicon wafer, an adhesion layer of titanium and an electroplating seed layer of gold are deposited by evaporating onto the silicon wafer. No mask is used for the silicon wafers. They are diced into pieces with the desired dimensions after electroplating.

NiFe electroplating is done using a standard recipe and procedure described by several authors [19][42][43]. The bath composition used in this work is given in Table 4-2. The volume of the electroplating bath used in this work is approximately 2 liters with an interelectrode distance of 10 cm. Different current densities were applied at room temperature without stirring.

Composition of Nickel-Iron Electroplating Solution		
Material		**Quantity**
Nickel Sulfate	$NiSO_4 \cdot 6H_2O$	200 g / l
Ferrous Sulfate	$FeSO_4 \cdot 7H_2O$	8 g / l
Boric Acid	H_3BO_3	25 g / l
Nickel Chloride	$NiCl_2 \cdot 6H_2O$	5 g / l
Saccharin	$C_7H_4NO_3S \cdot Na \cdot 2H_2O$	3 g / l

Table 4-2 Composition of nickel – iron electroplating solution. The temperature = 23° C .

The total plating area, the total current, plating efficiency, uniformity of the current density and shape of the plating area are the factors that affect the deposition rate, composition and uniformity. Plating efficiency is the fraction of current used to deposit material instead of evolving hydrogen. The residual stress is another important thing that limits the plated film thickness.

To characterize and condition the bath several samples are electroplated (Figure 4-20). At the initial trials saccharin was omitted from the electroplating solution. Electroplating attempts were made with different current densities ranging from 8 mA/cm^2 to 18.5 mA/cm^2. It is found that best results were obtained at a current density of 16 mA/cm^2 and EDS (Energy Dispersive Spectrometry) measurements show that the films consist of 13.28 % iron and 86.72 % nickel. The target value for permalloy, which has good magnetic properties is 20% iron 80% nickel. Other attempts with different current densities suffered from high residual stress. When the thickness reaches several microns, the permalloy sheet is peeled from the sides. Figure 4-21 shows the electroplated permalloy at different current densities.

Figure 4-20 Some of the early attempts of electroplating. Most of them suffered from high residual stresses and peeled from the sides.

Later on saccharin was added to the electroplating solution and better results were obtained. The samples displayed a smooth and bright surface at all current densities (Figure 4-22, Figure 4-23, Figure 4-24). For a current density variation in the range of 8 mA/cm^2 to 17.6 mA/cm^2, the nickel composition varied from 82.44 % to 91.65 %.

An inhomogeneous surface film composition was observed by the help of EDS. The growth mechanisms induce a composition variation with the deposition rate. The edge effect -crowding of current at the edges-, introduces a large variation of the composition. The mean film composition also varies with the current density.

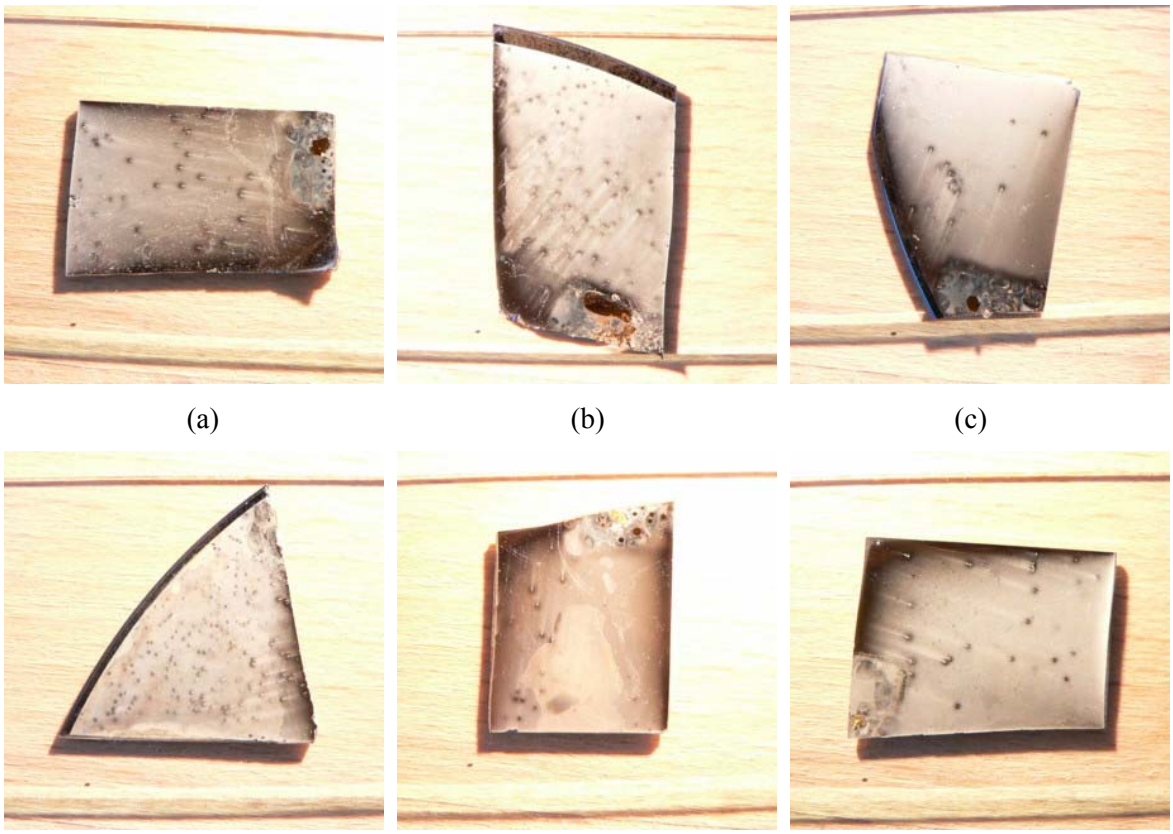

(a) (b) (c)

(d) (e) (f)

Figure 4-21 Electroplated permalloy before adding saccharin to the electroplating solution at different current densities: (a) 15 mA/cm^2, (b) 14.8 mA/cm^2, (c) 13.8 mA/cm^2, (d) 11.75 mA/cm^2, (e) 16.5 mA/cm^2, (f) 13.7 mA/cm^2. Best results were obtained at a current density of 16 mA/cm^2 (e) and EDS measurements show that the sample consists of 13.28 % iron and 86.72 % nickel.

The average thicknesses of the permalloy films were calculated by weighting the samples before and after the deposition. The thickness can vary throughout the sample because of the edge effect. Thickness inhomogenity can reach 150 % in the corners of the sample. The deposition rate is calculated from the average thickness of the sample. Iron plates more readily than nickel because of its lower reduction potential. As the current density increases the Fe composition fraction decreases

because the limit current is reached for iron, but the nickel current is not yet limited by the mass transport [44].

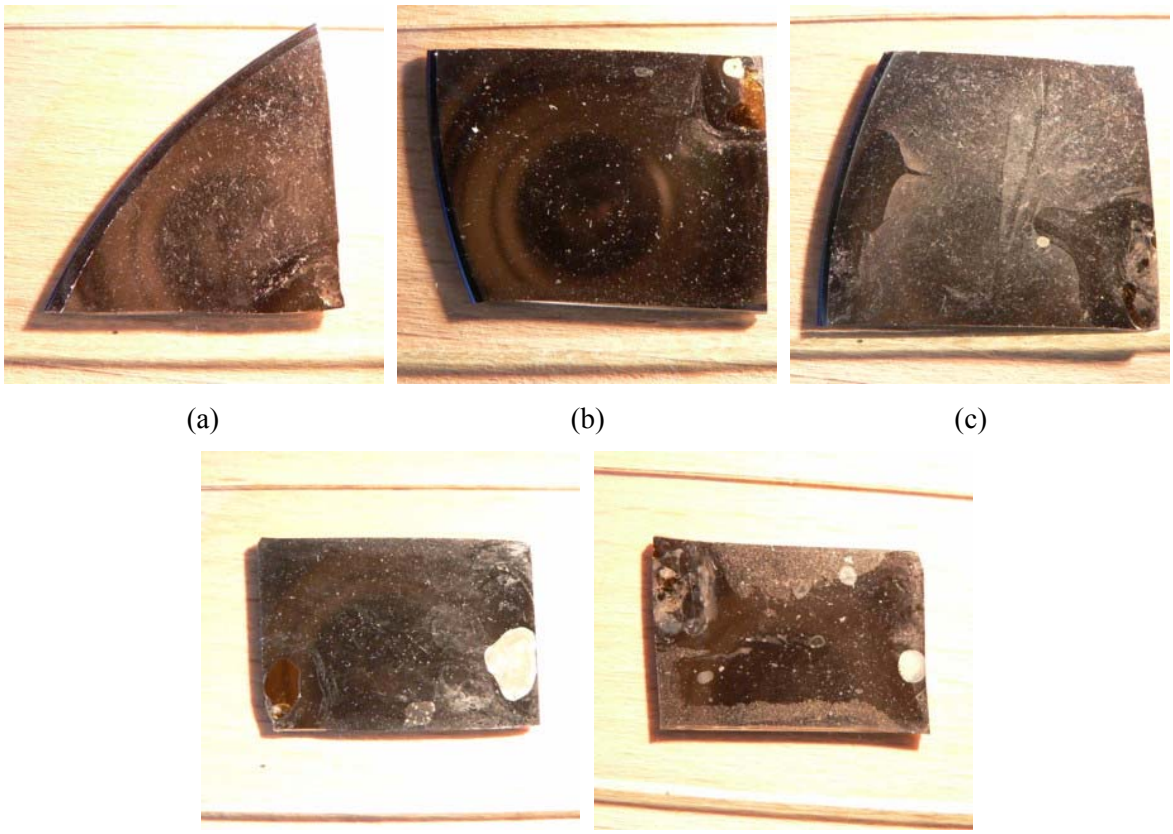

(a) (b) (c)

(d) (e)

Figure 4-22 Electroplated permalloy after adding saccharin to the electroplating solution at different current densities: (a) 12.8 mA/cm^2, (b) 7 mA/cm^2, (c) 10.2 mA/cm^2, (d) 15 mA/cm^2, (e) 16.5 mA/cm^2, (f) 17.6 mA/cm^2. For a current density variation in the range of 8 mA/cm^2 to 17.6 mA/cm^2, the nickel composition varied from 82.44 % to 91.65 %. With lower current densities electrodeposits closer to the aimed composition of Ni 80 % Fe 20 % were obtained.

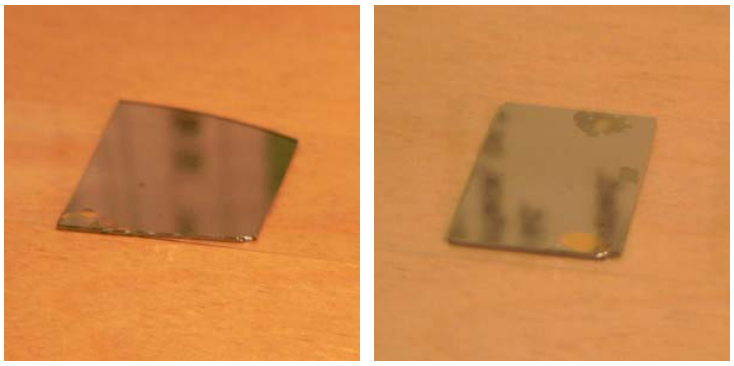

(a) (b)

Figure 4-23 After adding saccharin to the electroplating solution, the magnetic films displayed a smooth and bright surface at all current densities.

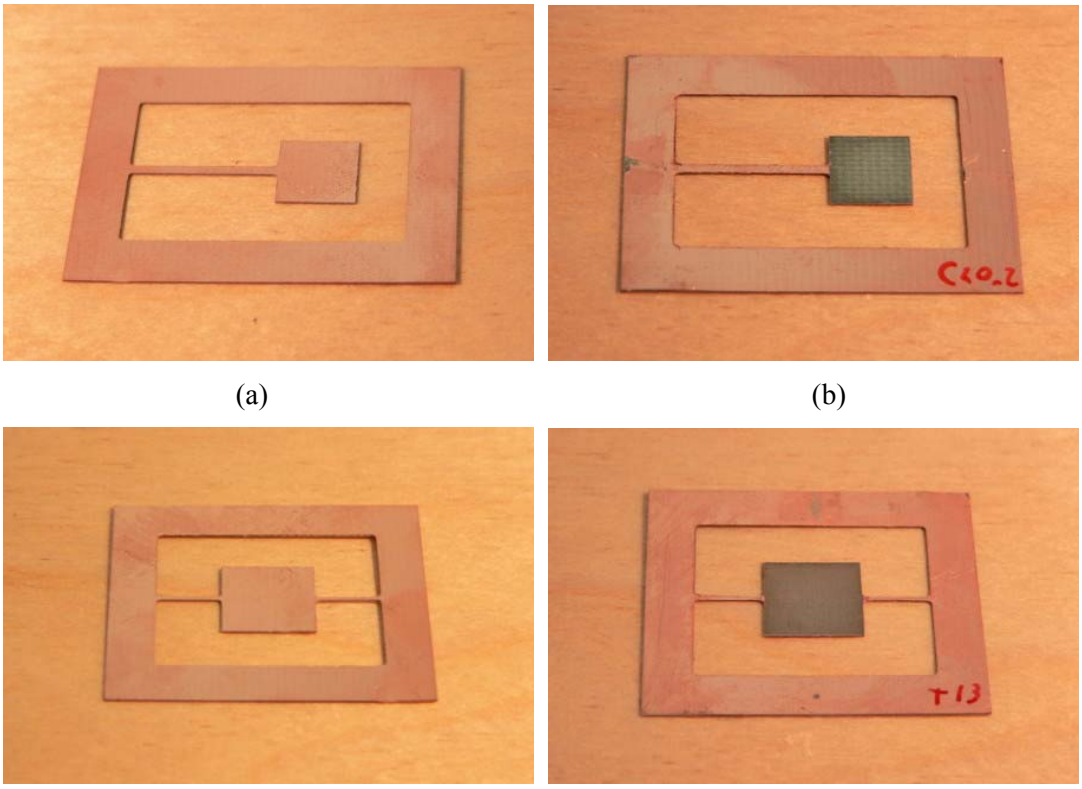

(a) (b)

(c) (d)

Figure 4-24 Cantilever type scanners before (a) and after (b) electrodeposition. Torsional scanners before (c) and after (d) electrodeposition.

Figure 4-25, Figure 4-26, Figure 4-27, and Figure 4-28 show SEM (Scanning Electron Microscope) images taken at different locations of the electrodeposits shown in Figure 4-24. In Figure 4-25 a hole formed by an H_2 bubble is clearly seen. At high current densities H_2 bubbles are formed more rapidly, causing lower surface quality. This is why removing the samples out of the solution is important in order to avoid the formation of H_2 bubbles.

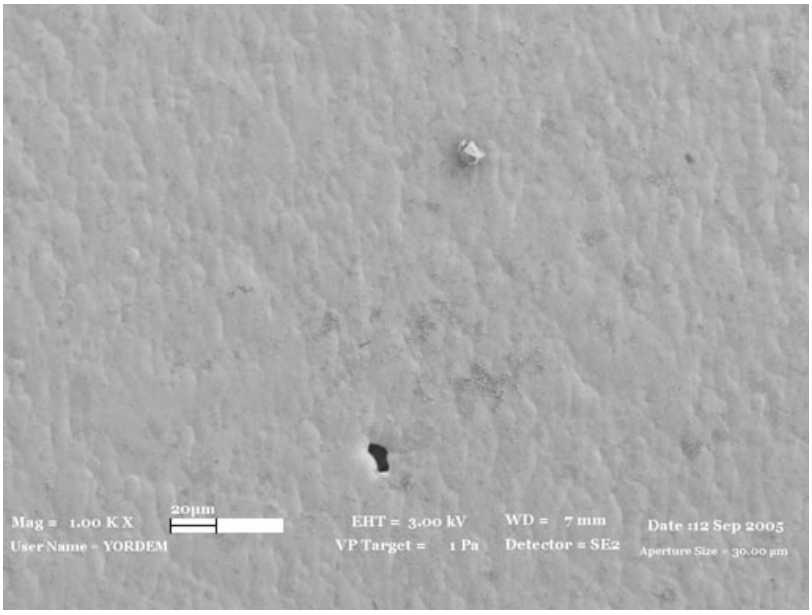

Figure 4-25 SEM image of the scanner shown in Figure 4-24 (d). The hole in the middle is formed by a H_2 bubble.

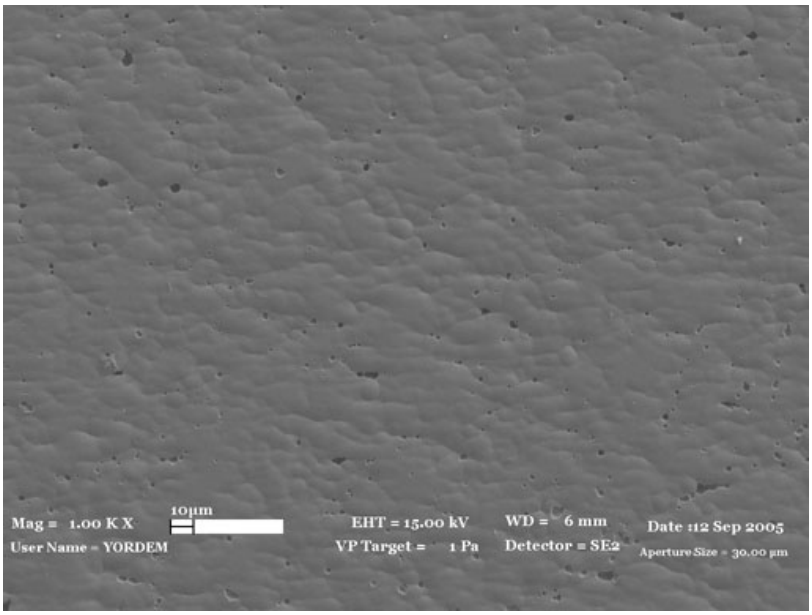

Figure 4-26 SEM image of the scanner shown in Figure 4-24 (d).

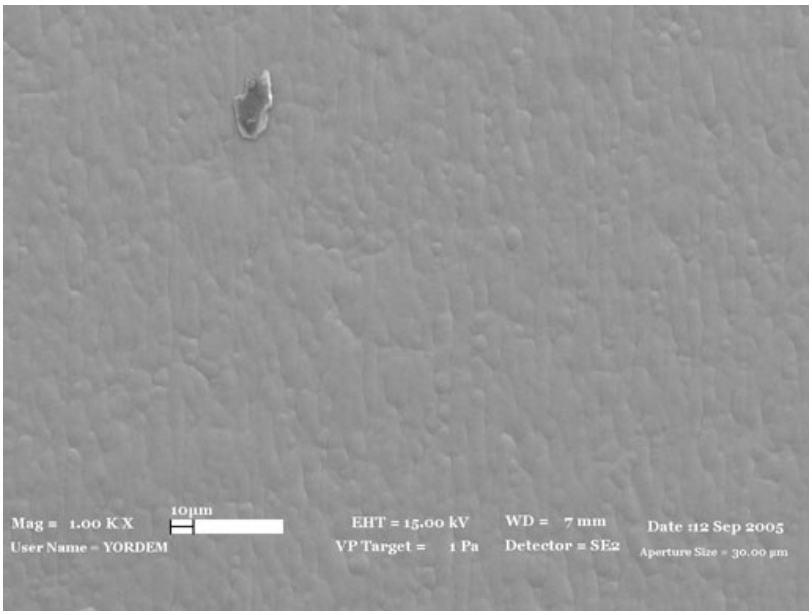

Figure 4-27 SEM image of the scanner shown in Figure 4-24 (b).

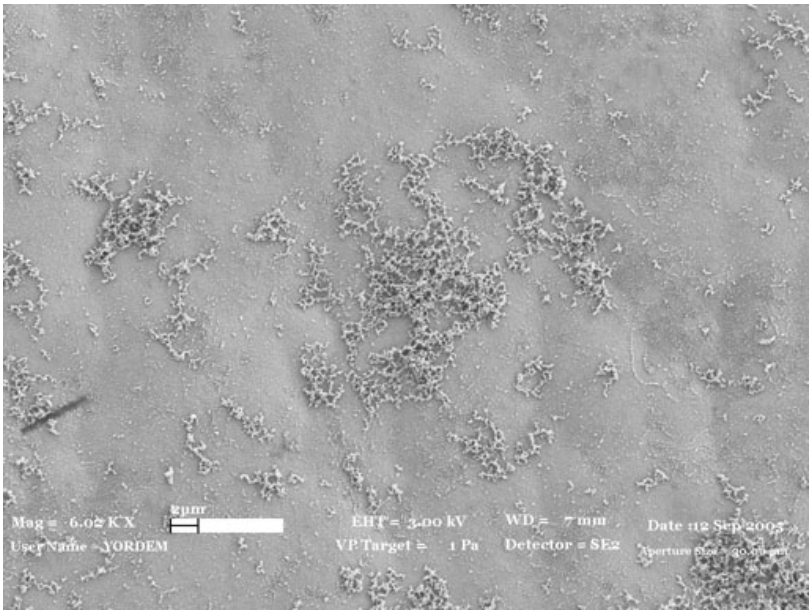

Figure 4-28 SEM image of the scanner shown in Figure 4-24 (b).

4.4 Magnetic Material Characterization

There are many different methods of measuring the magnetic properties of a material. Saturation magnetization, coercivity and the residual induction are the common quantities of interest. These quantities can be obtained from the hysteresis loop (BH loop) of the material.

The vibrating sample magnetometer (VSM) is one of the standard equipment for the magnetic characterization of powder, small samples and thin magnetic films. The sample is magnetized by a dc field and it is vibrated inside of a pick-up coil, thus its flux lines cut the windings of the coil generating a voltage. By measuring this voltage the magnetization of the sample is measured. Figure 4-29 shows the magnetic properties of electroplated permalloy found by VSM measurements at the University of Washington, Seattle, USA.

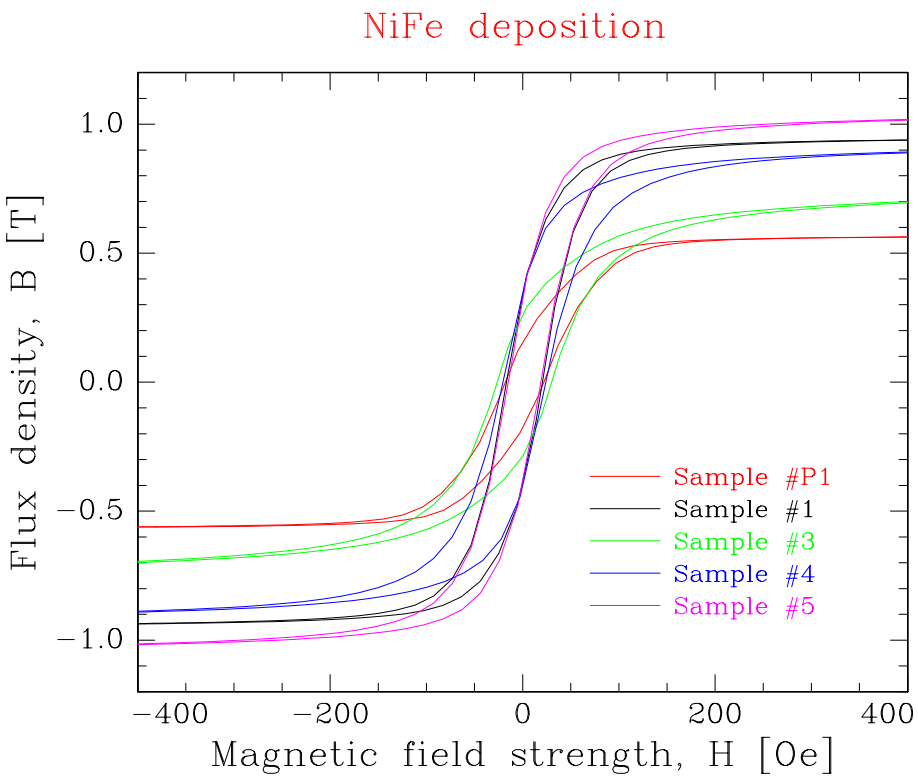

Figure 4-29 Hysteresis loops of different NiFe samples measured by VSM.

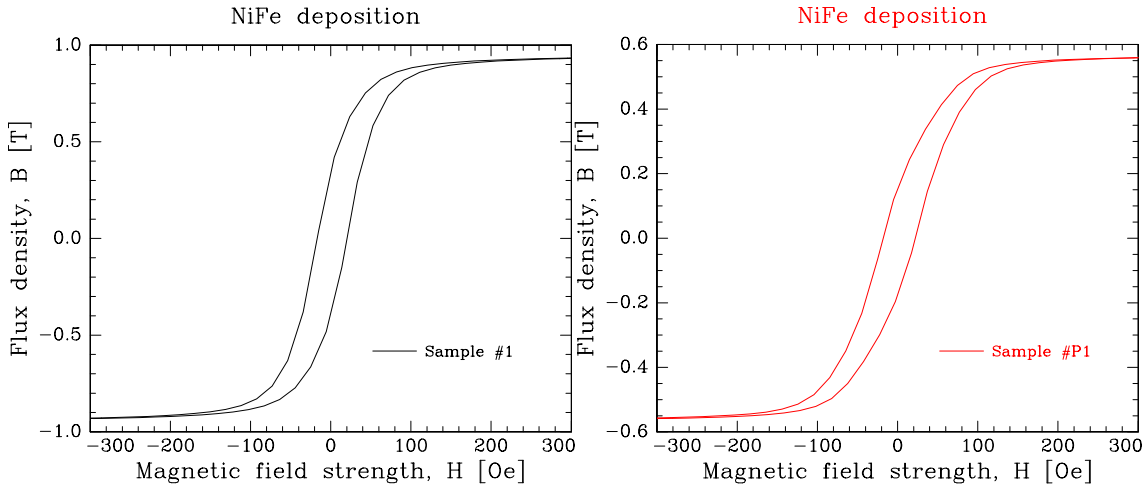

Figure 4-30 Hysteresis loops of a NiFe sample electroplated without saccharin (left) and with saccharin (right) in the plating bath.

Another means of displaying the hysteresis loop is through the use of alternating current. Two pick-up coils are placed in a spatially uniform time varying field. The sample is placed inside of one of the pick-up coils. The flux density inside of the magnetic material (sample) can be determined by taking the difference of the induced voltages on each coil and integrating the output over time. The setup described here is shown in Figure 4-31.

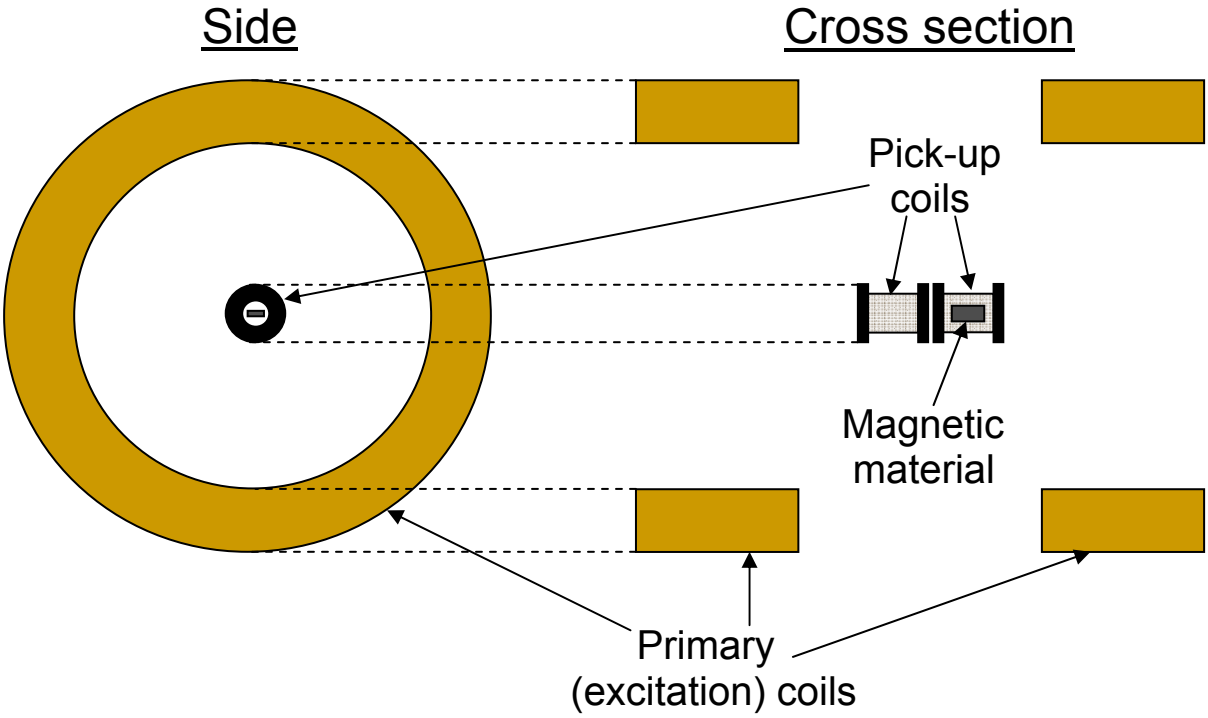

Figure 4-31 The setup to obtain the hysteresis loop of magnetic materials.

A Helmholtz coil can be used to generate the spatially uniform magnetic field. Finite element simulations were carried out to design a coil that generates a spatially uniform magnetic field at the position of the pick-up coils. Figure 4-32 (a) and (b) show the 3-D finite element simulation of the magnetic field and magnetic field as a function of position respectively.

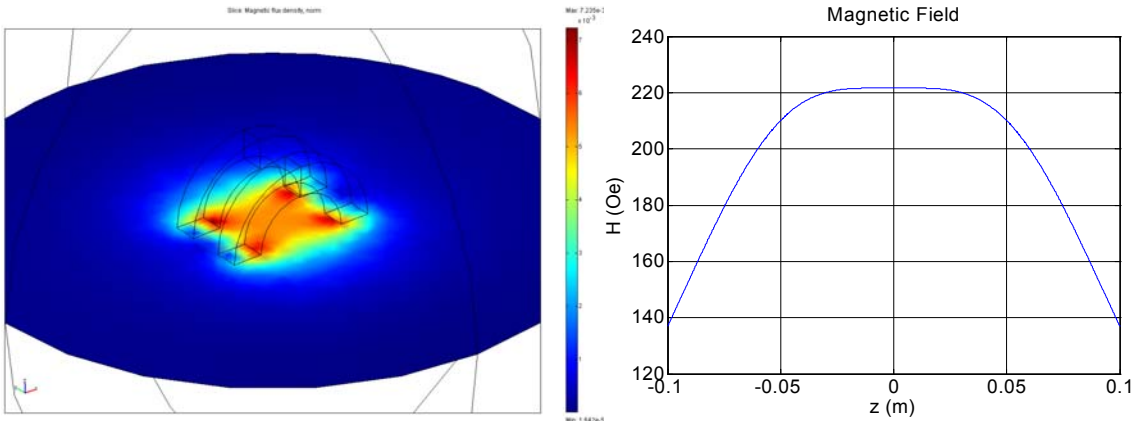

(a) (b)

Figure 4-32 (a) 3-D finite element simulation of the magnetic field, (b) magnetic field as a function of position. z = 0 is the middle of two coils.

The input ac current determining the applied magnetic field, H_s is sent through a resistor so it can be read directly in volts and is connected to the x-axis of an oscilloscope. H_s is proportional to the input current, I_1 times the number of turns, n_1 (4-1). The induced secondary voltage is sent through an integrator and the integrated voltage which is proportional to the magnetic flux density is connected to the y-axis of the oscilloscope. In the x-y mode of the oscilloscope, the hysteresis (BH) loop of the material is displayed on the screen. The induced voltage ε is given in equation (4-2) and magnetic flux density of sample, B_s is given by equation (4-3). n_2 is the number of turns of the pick-up coil and V_s is the volume of the sample. With the necessary scaling the desired parameters can be determined. The block diagram of this characterization setup is shown in Figure 4-33 and the photo of the setup built in Optical Microsystems Laboratory is shown in Figure 4-34.

$$H_s \propto n_1 I_1 \tag{4-1}$$

$$\varepsilon = -n_2 V_s \frac{dB_s}{dt} \tag{4-2}$$

$$B_s = -\frac{1}{n_2 V_s} \int_0^t \varepsilon \cdot dt \tag{4-3}$$

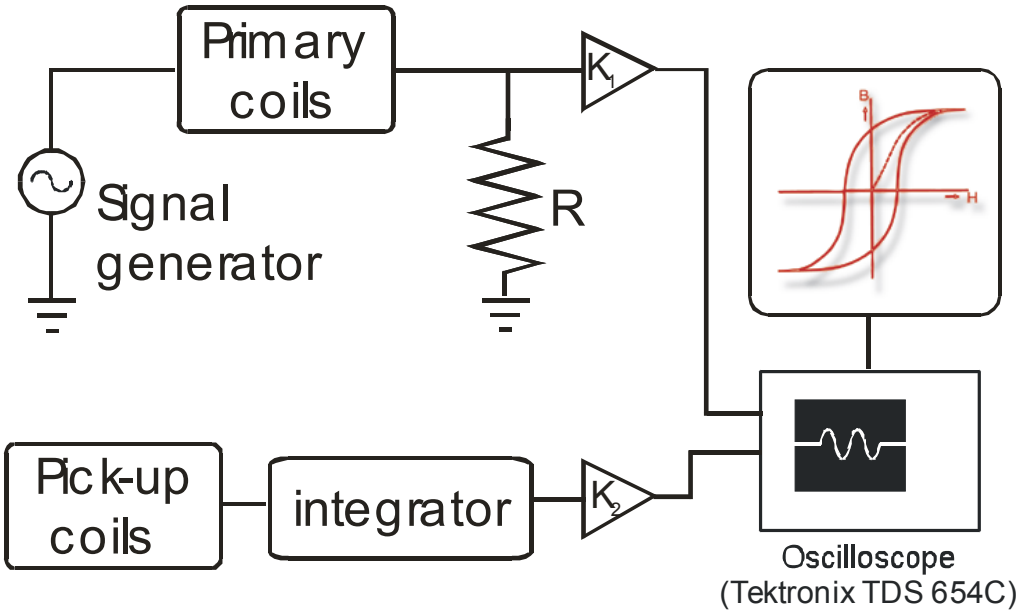

Figure 4-33 Block diagram of the characterization setup.

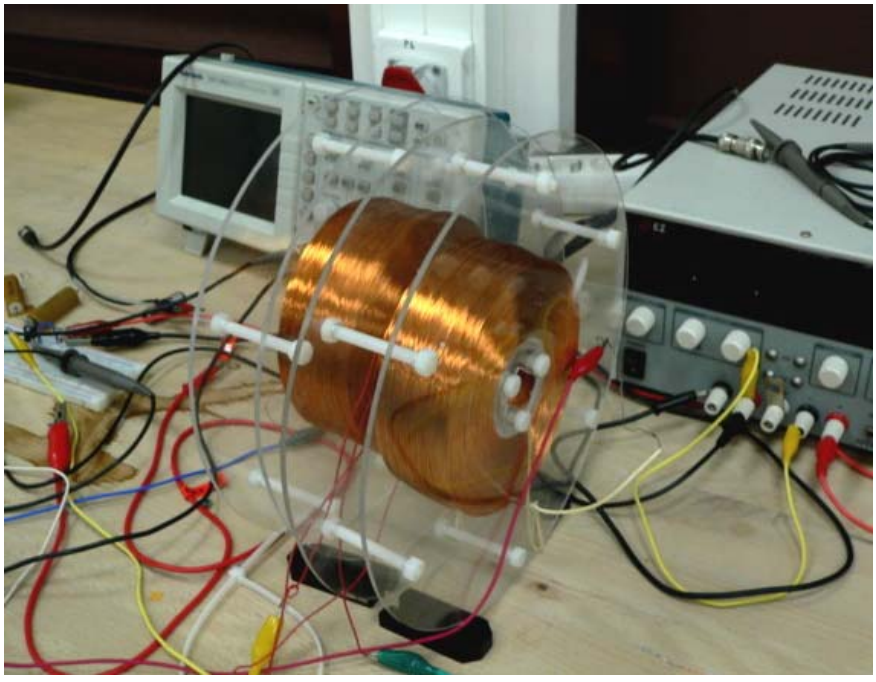

Figure 4-34 Photo of the characterization setup built in Optical Microsystems Laboratory.

5 TEST DEVICES AND EXPERIMENTAL RESULTS

Large angle static displacements for electromagnetically actuated structures for optical switching and other applications has been studied in a number of papers [19][23][24][25]. The work in this thesis focuses on the moving-magnetic material permalloy actuators in dynamic operation mode for small-angle deflections.

A number of prototype scanners are produced as described in Chapter 4 and the experimental results are compared with the analytical and FEM results. As an application, the microscanners developed in this research are applied to barcode scanning and has been demonstrated as a fully functional system.

5.1 introduces the test and characterization setups. The prototype scanners are examined in two sections. Static deflection measurements of the scanners are discussed in 5.2 and dynamic deflection measurements of the scanners are discussed in 5.3. In 5.4 a barcode reading setup is presented using the prototype scanners.

5.1 Static and Dynamic Characterization

Scanners described in this work are actuated with an external electromagnet. Modeling of electromagnets is discussed in detail in 3.4. In Figure 5-1 the cantilever beam scanner and the actuating external electromagnet is illustrated.

The produced scanners are tested with two methods:

- Static deflection measurements,
- Dynamic deflection measurements.

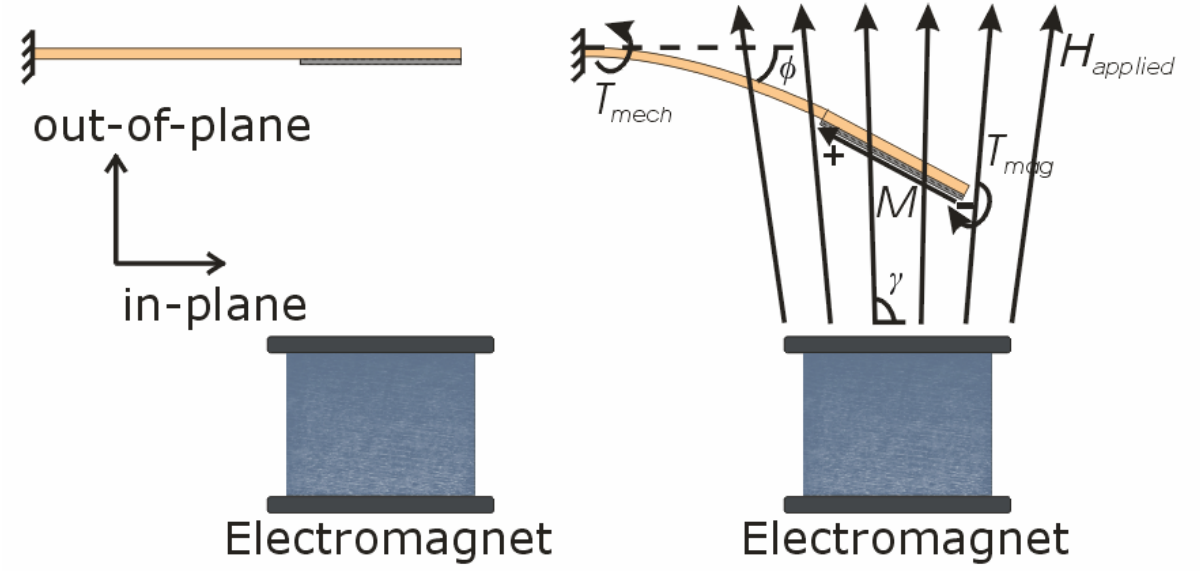

Figure 5-1 The cantilever beam scanner and the actuating external electromagnet. (a) When no current is applied to the electromagnet, (b) current is applied to the electromagnet.

Static Deflection Measurements:

Static deflection measurements provide information about the magnetic actuation mechanisms. The results are compared to the theoretical calculations to obtain better models of the devices. Furthermore, the maximum deflection can be obtained by optimizing the 3D positioning of the electromagnet underneath the scanner.

A distance measuring sensor (Selcom SLS 7000) is used for this purpose. Figure 5-2 illustrates the static deflection measurement setup and Figure 5-3 shows the setup pictures and test devices under test. The sensor sends a laser beam onto the device under test (i.e. scanner) and collects the reflection on a position sensitive detector (PSD). The scanner is actuated with the help of the electromagnet. When a DC current is applied to the electromagnet the scanner deflects and the centroid of the spot on the PSD moves. Using

triangulation the distance of the reflecting device is found. The distance measuring device has submicron sensitivity and it requires reflective surfaces for measurements.

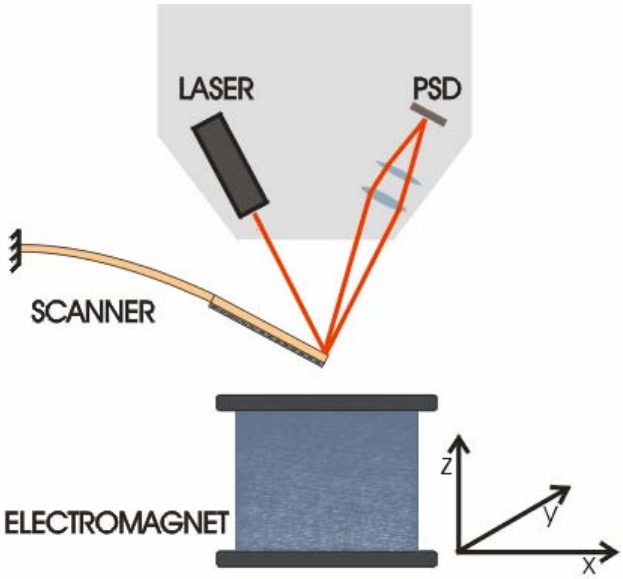

Figure 5-2 Illustration of the static deflection measurement setup using a position sensitive detector (PSD).

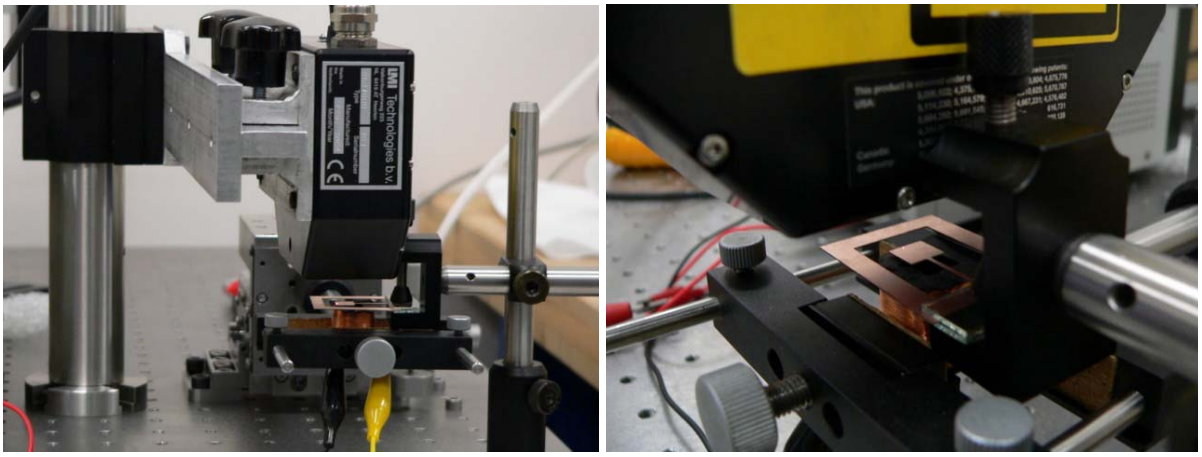

(a) (b)

Figure 5-3 Photos of the static deflection measurement setup.

Dynamic Deflection Measurements:

Dynamic deflection measurements were performed using a laser Doppler vibrometer (LDV, Polytec PDV 100). The dynamic response of the scanner is important as the scanners are operated at their resonance frequencies. Their frequency response characteristics are extracted using this setup. The electromagnet is excited by a function generator and the output of the LDV is displayed using an oscilloscope. The function generator and the oscilloscope are controlled by a computer using the GPIB interface. This enabled sweeping different parameters such as the frequency or the offset voltage and taking real time measurements using the oscilloscope while the parameters are swept. The response of the scanner at different locations relative to the electromagnet is also examined.

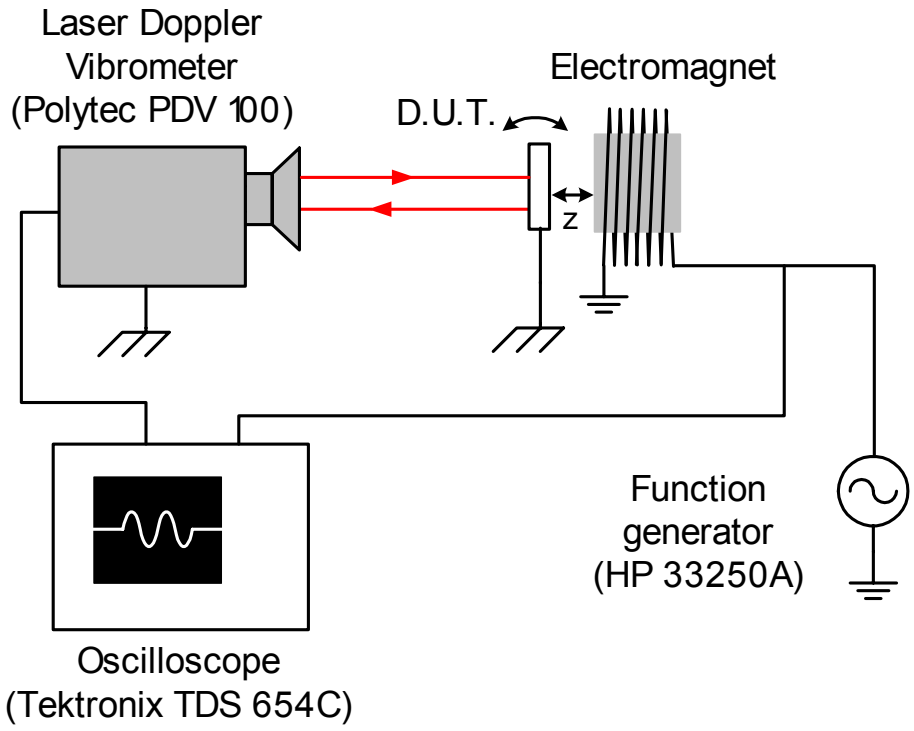

Figure 5-4 Illustration of the dynamic deflection measurement setup. LDV measures velocity which is converted to deflection by dividing with the angular frequency.

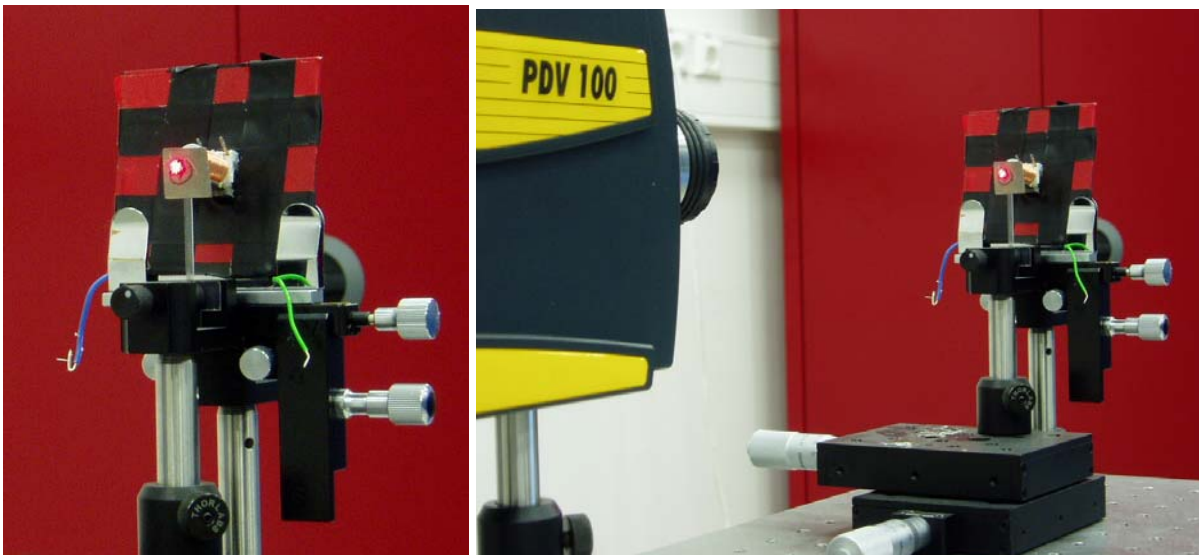

Figure 5-5 Photos of the dynamic deflection measurement setup.

5.2 Static Deflection Measurement Results

The first prototype device is an epoxy – glass fiber composite cantilever beam scanner. Copper is deposited as a seed layer for electroplating on both sides of the scanner. This increases the stiffness and the density of the structure. The suspension has dimensions of 1 mm x 15 mm x 0.26 mm and the rectangular plate has dimensions of 8 mm x 8 mm x 0.29 mm. It is anchored from the suspension end and an electromagnet is placed under the rectangular plate that supports the magnetic material and the scan mirror (Figure 5-1). The scanner is placed such that the rectangular plate is parallel to the top surface of the electromagnet with a distance of 1.5 mm. A magnetic field along the easy axis of the magnetic material is applied and removed prior to operation to induce a residual induction.

When the magnetic material (8 mm x 8 mm x 0.028 mm) is placed in a uniform magnetic field, it experiences only a torque. Since the rectangular plate is much wider, thicker and stiffer than the suspension we can assume it as mechanically rigid. Using (2-15) the mechanical deflection, x and the deflection angle, ϕ can be found using (2-7), (2-9) and (2-10). In the calculations an effective Young's modulus, E *(46.5 GPa)*, an effective density, ρ *(3450kg/m^3)* and a spring constant $k_\phi = 4{,}54 \times 10^{-3}$ are used.

As discussed in 3.3.4, due to thin magnetic film actuation, shape anisotropy effects are dominant and the other sources of anisotropy can be neglected. The shape anisotropy constant is calculated for the magnetic material using (3-16) and the plots are included in APPENDIX C. It has a length to thickness ratio of 285. Thus, the magnetization vector of the structure remains in the easy axis because of high shape anisotropy. The magnetic torque, T_{field} is then given by

$$T_{field} = VMH\sin(\gamma - \phi) \tag{5-1}$$

where V is the volume, M is the magnetization of the magnetic material, H is the applied magnetic field, γ is the angle between the magnetic field and the easy axis of the magnetic material at rest position. and ϕ is the mechanical deflection angle of the structure. If we neglect ϕ and take the vertical component of the magnetic field $H_z = Hsin(\gamma)$, (5-1) can be simplified to

$$T_{field} = VMH_z \tag{5-2}$$

The mechanical restoring torque, T_{mech} is given by

$$T_{mech} = -k_\phi \phi \tag{5-3}$$

At equilibrium $T_{field} + T_{mech} = 0$, and ϕ is given by

$$\phi = \frac{T_{field}}{k_\phi} \tag{5-4}$$

The maximum deflection angle is less than 6 degrees and the approximation error in magnetic force calculation due to small ϕ assumption is less than 0.75% even at the maximum deflection. Experimental results also demonstrate that neglecting ϕ for the magnetic force calculation is a good approximation.

Once *V, H, M* and k_ϕ are determined, equation (5-3) can be solved. The magnetization can be modeled as

$$M = \min(M_{residual} + \mu_r H_r, M_s) \tag{5-5}$$

where $M_{residual}$ is the residual magnetization, μ_r is the relative permeability, H_r is the radial component of the magnetic field and M_s is the saturation magnetization. The radial component of the magnetic field, H_r magnetizes the magnetic material as it is in the direction of the easy axis. $M_{residual}$, μ_r, and M_s are material properties and can be found experimentally. They are taken as $M_{residual} = 0.1\ T$, $\mu_r = 350$, and $M_s = 0.8\ T$ in the theoretical calculations.

However, the magnetic field supplied by the electromagnet is not uniform. Figure 3-14 and Figure 3-15 show the experimental and FEM results for H_z and H_r as a function of distance from the coil centre (r = 0 position) at the plane z = 1.5 mm above the coil surface. The measured values of H_z and H_r are used in the theoretical magnetic force calculations. Average values of the H_r and H_z along the length of the magnetic material are used in the formulas.

As the magnetic field is not uniform the forces on the charges of a magnet does not cancel out resulting in a net torque. As the magnetic field on one pole is different than the magnetic field on the other pole, the forces they generate on the north (N) and south (S) poles are also different.

$$F_N = \varphi H_N = MSH_N \tag{5-6}$$

$$F_S = \varphi H_S = MSH_S \tag{5-7}$$

A net force given by $F_{NET} = F_N - F_S$ is generated. To account for these forces generated throughout the sample because of the changing magnetic field relative to the displacement, the magnetic material is divided into sections with positive and negative poles. The forces on the magnetic charges of the poles are calculated and the net forces resulting from their differences are also found. These forces are multiplied by the corresponding distances from the anchor to obtain the corresponding torques. Lastly the torque due to each section are added together to find the total torque and the scanner deflection using (5-2).

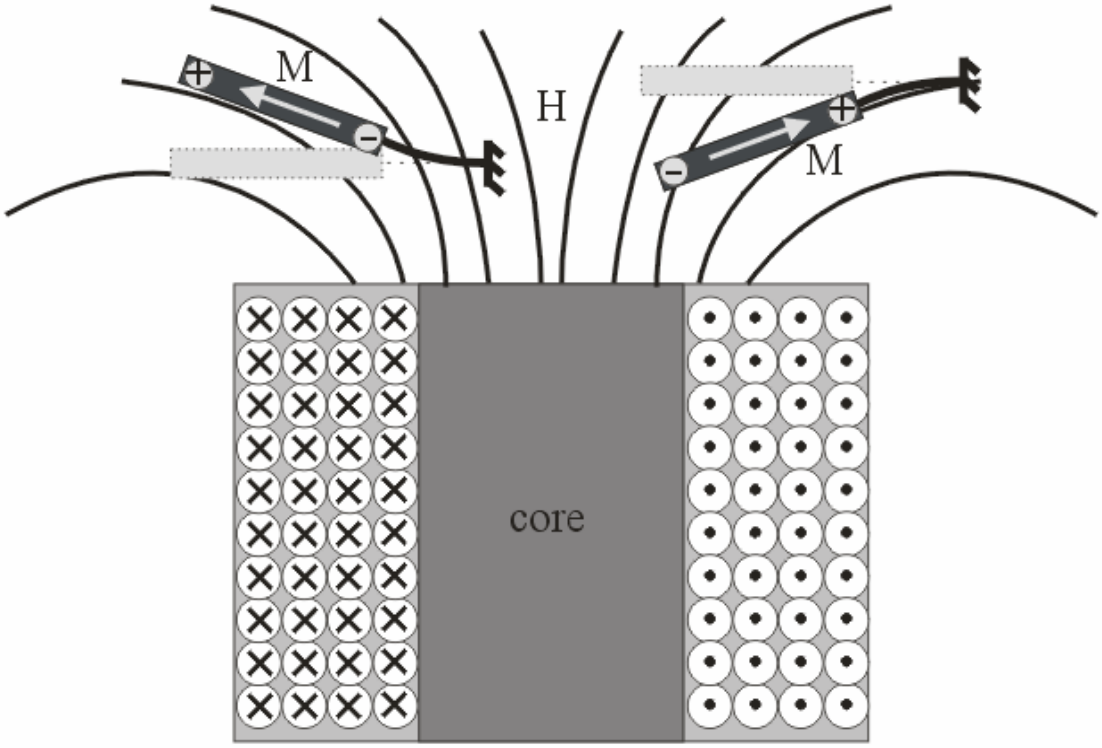

Figure 5-6 The magnetization vector tries to align with the magnetic field lines. On the left of the electromagnet the magnetization is leftward so the scanner deflects upward and on the right the magnetization is rightward so the scanner deflects downward.

Soft magnetic materials are known to be attracted towards magnets or electromagnets. As an example, a scissor is always attracted towards a magnet. However, as illustrated in 5.7, in thin magnetic films, the mechanical deflection can be bidirectional. Due to the high shape anisotropy, the magnetization doesn't rotate and remains in-plane and the entire structure experiences a torque, which can be bidirectional. The direction of the torque is determined by the direction of the magnetic flux lines and the anchor point of the structure. For the scissor example, the magnetization does not have a strong preferred direction and rotates to align itself with the external field. The translational magnetic force towards the magnet is then produced by the large field gradient to maximize the magnetostatic energy.

Figure 5-7 shows the theoretical and the experimental tip deflections as a function of the applied DC current at different radial distances, y as separate plots and Figure 5-8 shows them on the same plot. The static deflection measurement setup is used to obtain the experimental deflections.

Keep in mind that the magnetic torque is proportional to the product of H_z and M, and M increases with H_r until the material is saturated. For low current values, the material is not saturated and the torque increases quadratically with current. For large current values, the material is saturated (i.e., M is constant) and the torque increases linearly with current. Where the transition from quadratic to linear relationship occurs is determined not only by the applied current but also with the relative position of the electromagnet as illustrated in Figure 5-7. For large values of y (e.g., $|y|>4.5$mm), magnetic field lines that interact with the scanner are bent away from the vertical direction and H_r is larger than H_z, the magnetic material is saturated at lower current values and the torque current relationship is linear in the depicted current ranges . For small values of y, the radial component of the magnetic field is weaker and does not saturate the material until current is very large. Thus, the generated torque increases quadratically for small currents due to the linear increase in H_z and M until M gets close to saturation. Once M is saturated, the torque increases linearly.

At larger radial distances theoretical versus experimental data is in good agreement. But close to the center of the electromagnet the error between them increases as the magnetization changes direction near the centre. It is harder to model the magnetization in this region. We can see clearly from these plots changing the direction of the radial component of the magnetic field, H_r changes the direction of magnetization so the direction of the deflection.

Figure 5-9 shows the theoretical and the experimental tip deflections at various DC currents as a function of the radial (y) distance. Note that, the maximum deflection is obtained when the coil is moved in the $y<0$ direction. Magnetic force along the magnetic film is a distributed force and is a function of H_z along the magnetic material. As the electromagnet moves in the $y<0$ direction, the magnetic force gets larger towards the tip of the cantilever scanner, thereby producing a larger torque compared to moving in the other direction.

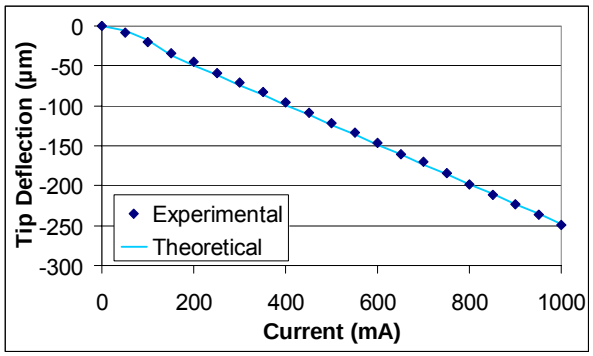

(a)y = -6.5 mm

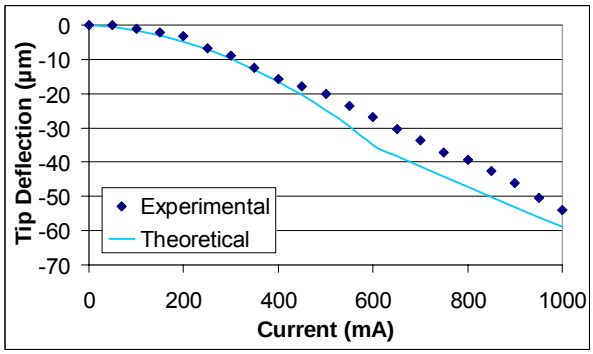

(b) y = -2.5 mm

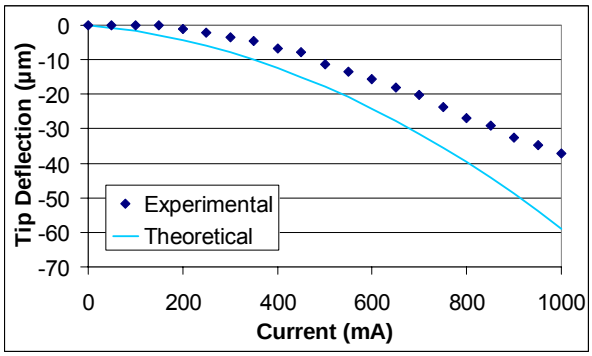

(c)y = -0.5 mm

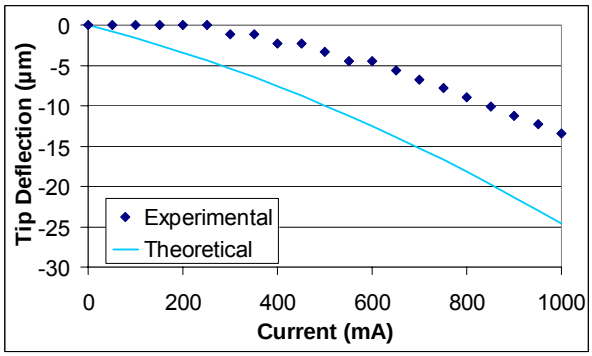

(d) y = 0.5 mm

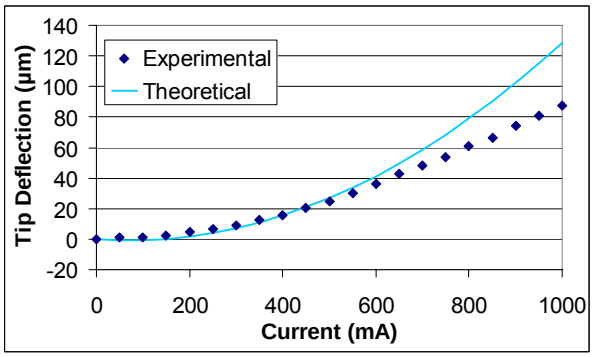

(e)y = 2.5 mm

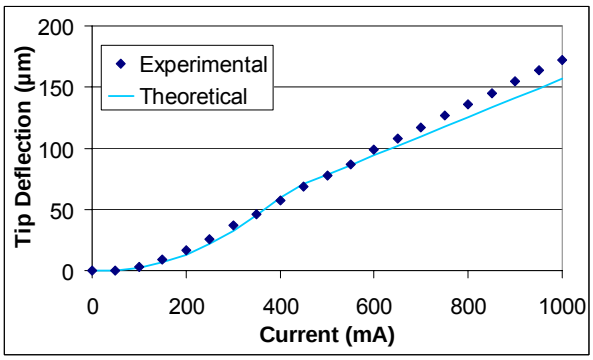

(f) y = 4.5 mm

Figure 5-7 Tip deflection as a function of the applied current. The scanner is placed at the center of the electromagnet and 1.5 mm away from its top surface. It is moved in the positive and negative directions along the y axis without changing the x and z displacement. The plots show the deflection at (a) y = -6.5 mm, (b) y = -2.5 mm, (c) y = -0.5 mm, (d) y = 0.5 mm, (e) y = 2.5 mm, (f) y = 4.5 mm

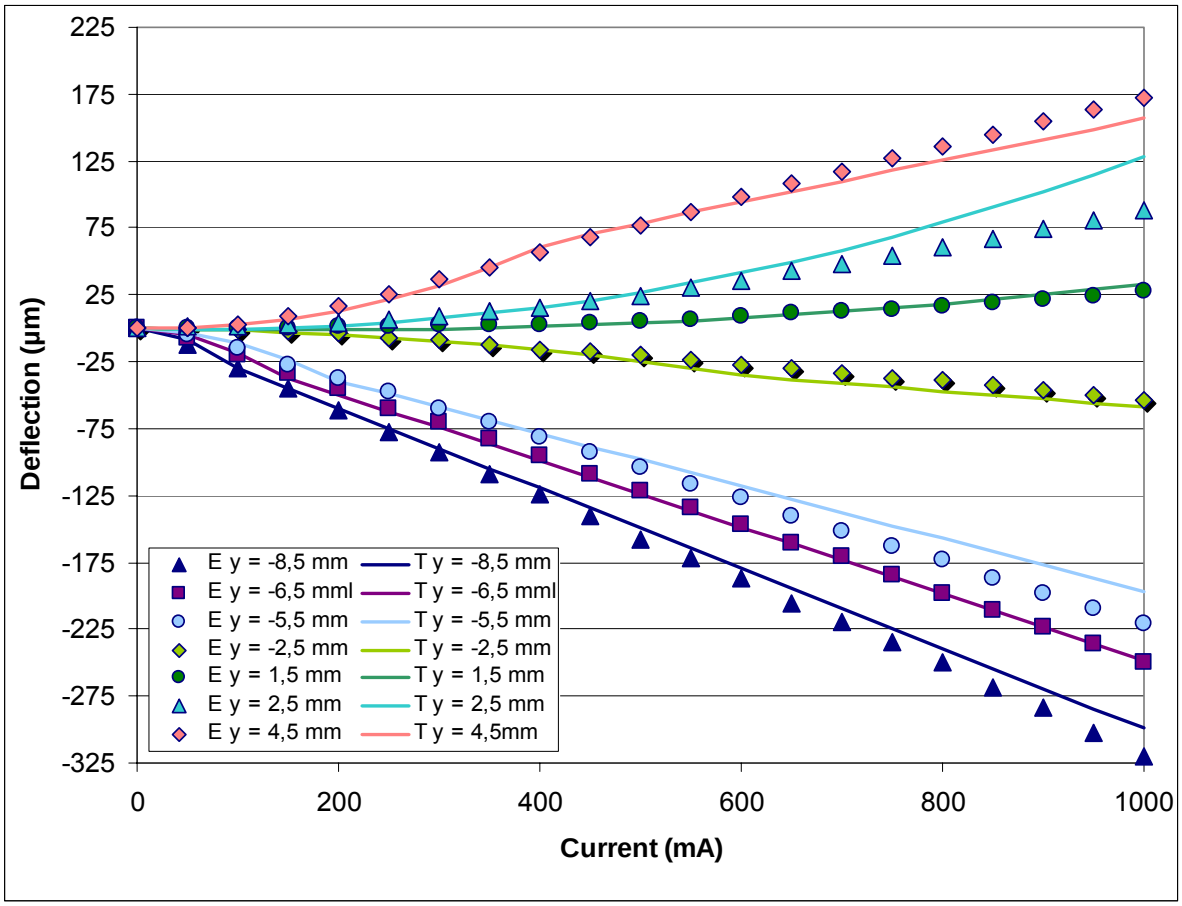

Figure 5-8 Tip deflection as a function of the applied current. The scanner is placed at the center of the electromagnet and 1.5 mm away from its top surface. It is moved in the positive and negative directions along the y axis without changing the x and z displacement. On the legend E means experimental result and T means theoretical result.

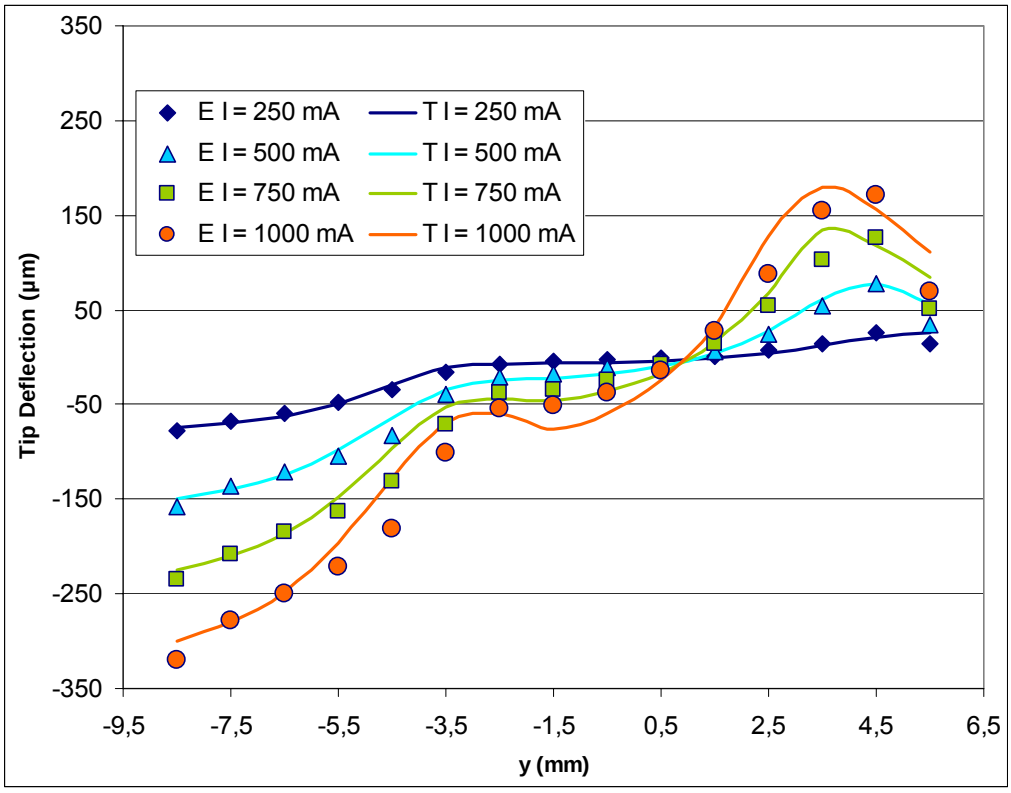

Figure 5-9 Tip deflection as a function of the radial (y) distance at different current values. The scanner is placed at the center of the electromagnet and 1.5 mm away from its top surface. It is moved in the positive and negative directions along the y axis without changing the x and z displacement. On the legend E means experimental result and T means theoretical result.

5.3 Dynamic Deflection Measurement Results

The prototype device used for dynamic deflection measurements is a polymer (RenShape SL5195) cantilever beam scanner. Polymer resin was molded and cured by UV light into the desired scanner shape. Mold defines both the flexure and the mirror dimensions. As illustrated in Figure 5-1, the cantilever beam is anchored from the left and the rectangular plate at the right supports the mirror and the magnetic material. A silicon wafer is coated with Aluminum and diced into square pieces and attached to the polymer plate from the top and the electroplated magnetic material (NiFe – permalloy)

is attached to the bottom side of the plate. The suspension has dimensions of 1 mm x 15 mm x 0.5 mm and the rectangular plate has dimensions of 8 mm x 8 mm x 1 mm. The scanner is placed such that the rectangular plate is parallel to the top surface of the electromagnet. A magnetic field along the easy axis of the magnetic material is applied and removed prior to operation.

The deflection of the scanner is modeled using the balance between the magnetic torque T_{field} and the mechanical restoring torque T_{mech} as described in the static deflection measurement section. The magnetic torque T_{field}, generated by the interaction of the permalloy sheet and the external magnetic field is given by (5-1). The deflection angle of the scanner for small deflections is given by (5-3).

The moment of inertia of the mirror is much greater than the moment of inertia of the suspension beam; therefore the bending of the mirror is negligible and is not considered. This assumption is verified with FEM simulations. Density and the Young's modulus for the material used are 1180 kg/m^3 and 1628 MPa.

The magnetization of the permalloy sheet is assumed to remain along the easy axis which is in-plane because of the high shape magnetic-anisotropy. When operated in small angular displacements the out-of-plane component of the magnetic field is not sufficient to magnetize the permalloy sheet. The in-plane magnetic field component becomes more important as the magnetization M is induced by this component.

The effect of the in-plane component of the magnetic field on the magnetization hence to the angular displacement, is observed by using the same electromagnet described in 3.4.

The magnetic field simulations are performed using finite element modeling software (FEMLAB 3.1). Figure 5-10 shows the in-plane (H_r) and out-of-plane (H_z) components of the magnetic field versus the distance between the coil and the permalloy sheet. Figure 5-11 shows the product of H_r and H_z as the electromagnetic torque depends on the $M \cdot H_z$ product and M is a nearly linear function of H_r. From Figure 5-11 the maximum torque can be achieved by placing the permalloy sheet about 3.5 mm from the coil. Also the product increases going away from the center axis. Figure 5-12 shows the experimental peak-to-peak deflection of the scanner placed at the center of the coil as a function of the distance between the coil and permalloy which is consistent with the FEM simulations. The coil was excited with a small biased-sinusoidal current waveform at the scanner's resonant frequency of 49 Hz.

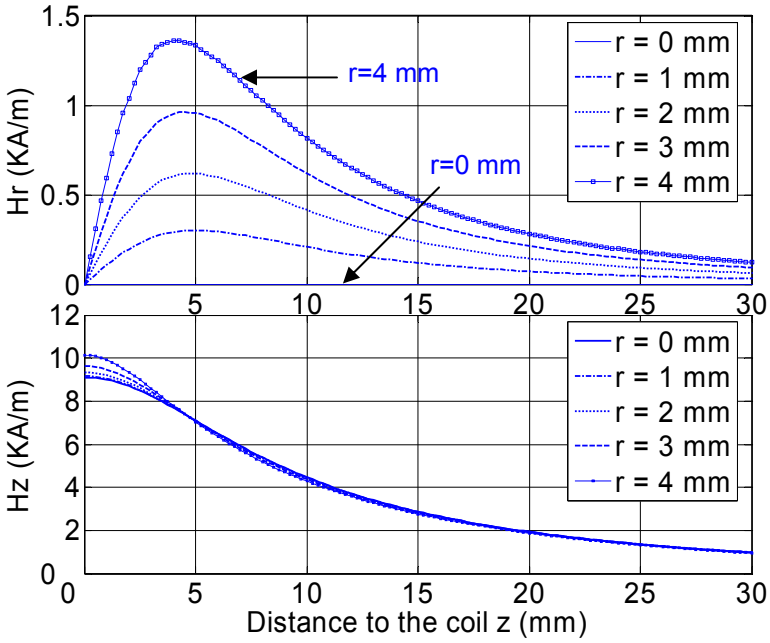

Figure 5-10 FEM simulations of the in-plane, H_r and out-of-plane, H_z component of the magnetic field H_a, plotted versus distance between the coil and permalloy sheet taken at different radial distances from the central axis.

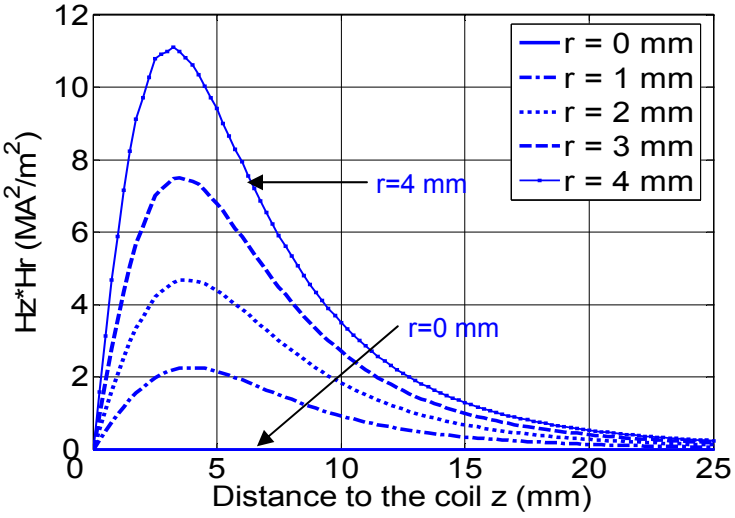

Figure 5-11 FEM simulations of the product of H_r and H_z versus the distance between the coil and the permalloy sheet. The product is proportional to the point magnetic force acting on the structure for small current excitation case.

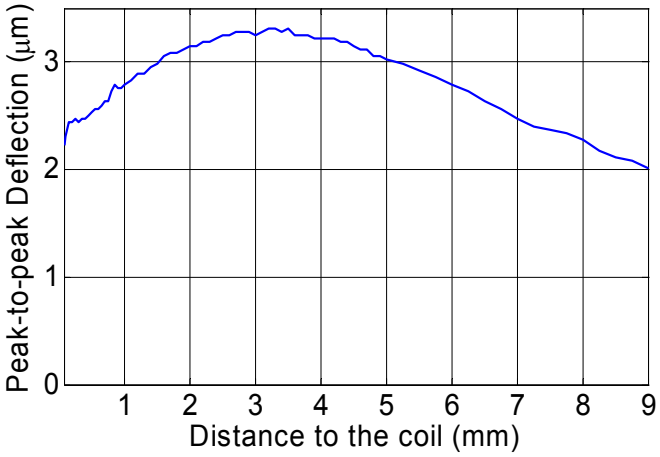

Figure 5-12 Measured dynamic peak-to-peak deflection of the scanner versus the distance between the coil and the permalloy sheet.

The dynamic deflection of the scanner was measured using the LDV (Figure 5-4, Figure 5-5). Figure 5-13 shows the peak-to-peak deflection of the scanner when an ac signal on top of a dc offset is applied. Out-of-plane flux density of 3.5 mT is generated by the DC current. DC field magnetizes the permalloy sheet and AC signal results in oscillation at the scanner resonant frequency. The difference between theory and experimental data at high AC currents originates from the change in magnetization, which is kept constant at its dc value in the theoretical calculations.

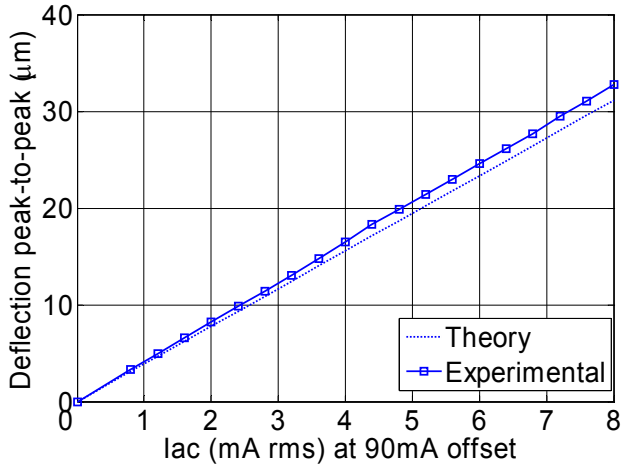

Figure 5-13 Tip deflection as a function of the ac drive current on top of a 90 mA DC current applied to a 1200 turn coil.

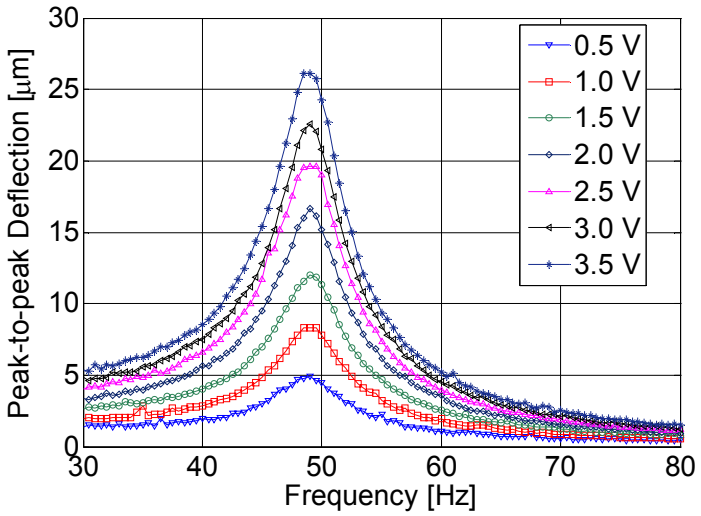

Figure 5-14 Offset voltage dependency of the scanner resonance.

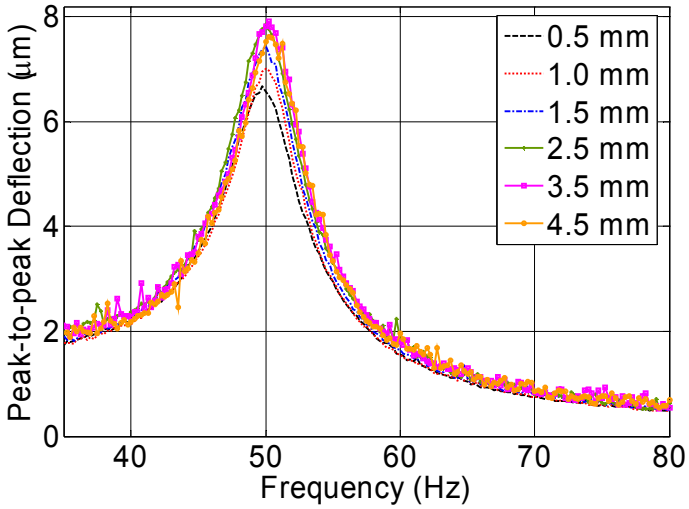

Figure 5-15 Dependency of the scanner resonance to the distance between the scanner and the coil.

Figure 5-14 shows the frequency response of the scanner for different offset values. Figure 5-15 shows the frequency response of the scanner for different coil distances. As the distance is decreased, a slight spring softening effect is observed due to larger deflections.

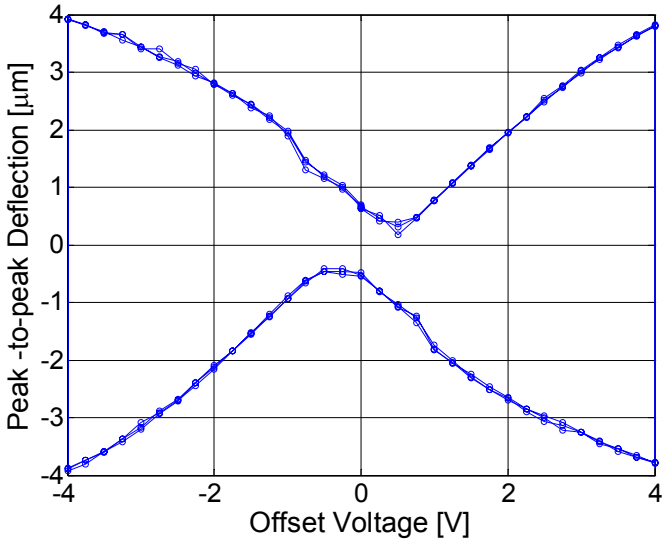

Figure 5-16 Peak-to-peak deflection of the scanner as a function of the offset voltage. The positive and negative values are used to indicate direction of offset voltage sweep.

Figure 5-16 shows the peak-to-peak deflection of the scanner as a function of the offset voltage in order to show the dependency of the scanner deflection to the offset magnetic field. The deflection is plotted positive for forward sweep of the offset voltage and plotted as negative for backward sweep of the bias voltage. Nonlinearity and the hysteresis in the curve are due to the typical BH curve of the materials. The minimum AC deflection is attained at a non-zero value of the offset, which is due to the magnetization that remains on the magnetic material even when the field is zero.

5.4 Barcode Scanner System

The scanners explained in this chapter are demonstrated in a barcode reading system. A smaller coil is used to actuate the scanner and generate high in-plane and out-of-plane magnetic fields. The coil is driven with a sinusoidal signal on a DC offset at the mechanical resonance of the scanner *(f_{res} = 55 Hz)* and mechanical deflections of ±7.5 degrees were observed.

The schematic representation of the system is illustrated in Figure 5-17. Light from a laser diode is incident on the scanner. The light is focused and scanned over the barcode with the necessary

optical elements. The scattered light is collected with a lens to the photo diode (PD) while the beam is scanned over the barcode. The output of the photo diode is processed with the necessary electronics to get the desired signal. Low resonant frequency of the scanner allowed using low-cost, widely available electronic components for data processing.

Using this test setup, different kinds of barcodes are read successfully. The cantilever scanner in operation and the output of the photo diode on the scope are shown in Figure 5-18 (a) and (b) respectively. The output shown on the scope is filtered, then digitized and processed with a microprocessor. Different width black and white stripes in the original barcode are reconstructed using the distance between subsequent peaks in the scope signal. The photo of the overall setup in operation is shown in Figure 5-19.

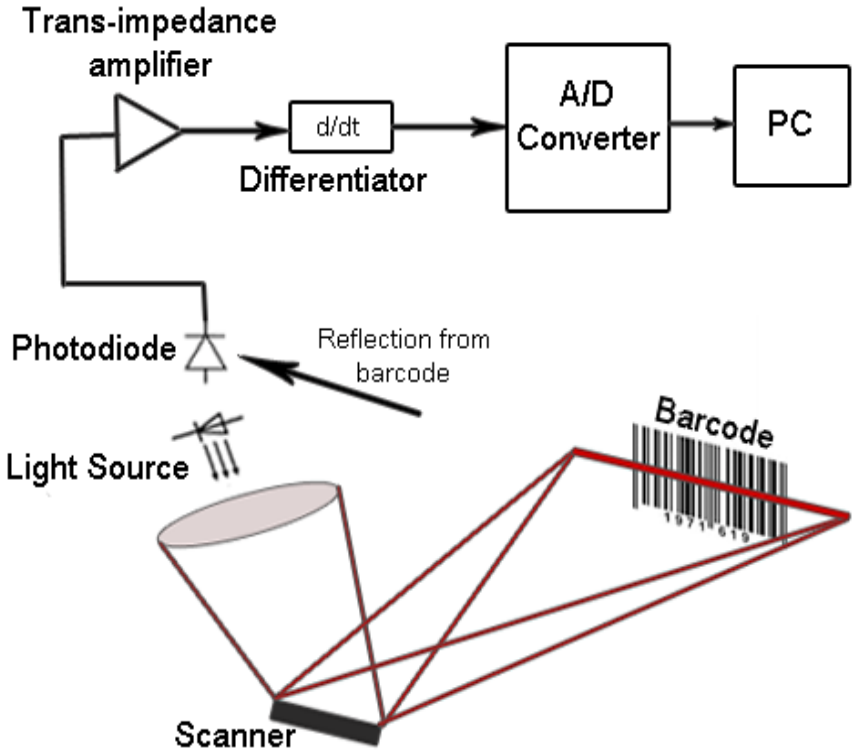

Figure 5-17 The schematic representation of the barcode reading system.

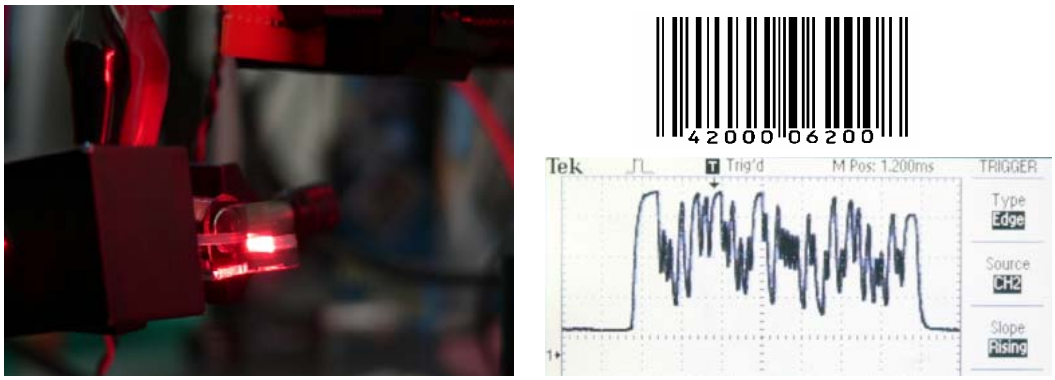

(a) (b)

Figure 5-18 (a) The cantilever scanner in operation. (b) The output of the photo diode on the scope. The valleys are the black stripes on the barcode.

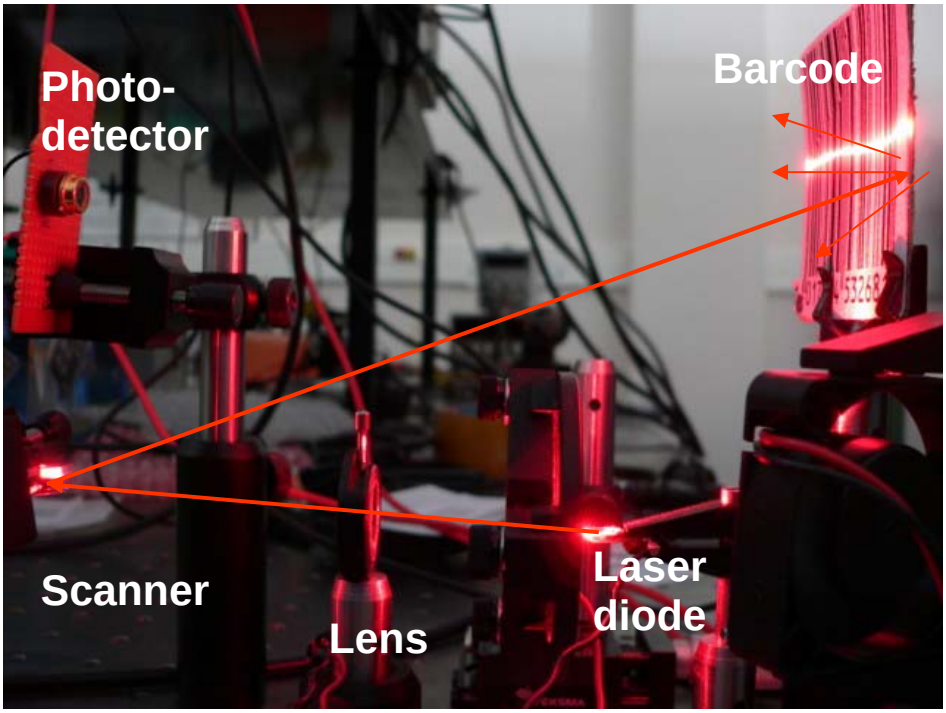

Figure 5-19 Photo of the overall setup in operation. Light from a laser diode is incident on the scanner. The light is focused and scanned over the barcode with the necessary optical elements. The scattered light is collected to the photo diode (PD) while the beam is scanned over the barcode. The output of the photo diode is processed with the necessary electronics to get the desired signal.

6 CONCLUSIONS

In this research, design and fabrication of polymer magnetic actuators for laser scanning have been performed. Very simple and low-cost fabrication processes using molded polymers and electroplated magnetic films for magnetic actuation have been developed. The developed scanner performance is adequate for barcode reading and various imaging applications.

Two types of scanners are studied: cantilever beam type scanners and torsional scanners. The devices are aimed to be operated at their resonant frequencies. For barcode reader applications, low resonance frequencies (<200Hz) are preferred because of electronics bandwidth requirements. Low resonant frequencies are easier to achieve with polymers due to low Young's modulus compared to Silicon MEMS scanners.

In the scanner system, polymers are used as the structural material, magnetic powder mixed with the polymer or electroplated permalloy films are used together with external coils for magnetic force generation, and aluminum coating layer or aluminum coated silicon mirrors embedded in or glued on the polymer are used to make the surface highly reflective.

Polymers are shaped by molding or epoxy-glass fiber composite boards are shaped using conventional machining. Both of them are simple and low cost processes and unlike Silicon micromachining, these processes do not require clean room and photolithography. The reliability and long term durability of the polymers used in this work are not investigated. Materials like epoxy and polyimide have been used by the industry and academia for a long time. As a future work they can be incorporated with the molding process described here.

Two methods of adding magnetic materials to the scanner are investigated. In the first method magnetic particles are mixed with polymer before curing. The other method involves electroplating permalloy films onto the scanner. Better results were obtained in terms of the magnetic actuation by the electroplating method.

An important advantage of using magnetic powder mixed into the polymer is that it does not require additional fabrication steps. The compatibility of such mixtures with the molding process

described here was shown. Other types of polymers such as different epoxy mixes and polyimide can be tried with different magnetic powders to improve the loading percentage of the magnetic material in the mixture. Several authors show that good hard magnetic properties can be obtained using such mixtures [39][40][41]. Different polymer-magnetic powder compositions and their optimization can be the subject of a future research. Some coatings can also be used for the magnetic particles to increase the loading concentration. In the future the coatings and concentrations can be optimized for a given polymer - magnetic powder mixture to obtain better magnetic composites. Experimenting with magnetization of the magnetic powder during or after the polymer curing process can potentially produce higher magnetization and larger magnetic force.

For obtaining good quality magnetic films, processes for electroplating permalloy have been developed. Effects of current density and other parameters on the material properties are investigated. The process was optimized for electroplating low stress films with good magnetic properties close to the intended composition percentage of 20 % iron 80% nickel.

Another contribution of this work was in modeling and optimization of the magnetic actuation using electroplated thin films in both saturated and unsaturated modes of operation. The regime of large angular displacement in DC magnetic field has been studied in a number of papers [19][23][24][25]. This work focuses on the permalloy actuator's dynamic small-angle rotations in AC field. It is concluded that the radial component of the magnetic field is important for small angular rotations as it magnetizes the material. The prototype devices are tested using static and dynamic methods and the experimental results are compared to the theoretical work. Good results were obtained showing that the experimental and theoretical results are consistent.

Lastly a barcode reading system is demonstrated using the developed scanners. The performance requirements were met and barcode reading was successfully demonstrated.

APPENDIX A

Cantilever Beam						
(mm)	**C - I**	**C - II**	**C - III**	**C - IV**	**C - V**	**C - VI**
w1	1	1	1	1	1	1
l1	15	12	15	15	10	20
h1	0,5	0,5	0,5	1	0,5	1
w2	8	5	6	8	5	8
l2	8	5	6	8	5	8
h2	1	1	1	1	1	1

Table A-1 Dimensions of the supporting beams and mirrors for the cantilever beam scanner prototypes.

Torsional Scanner				
(mm)	T - I	T – II	T - III	T - IV
w1	1	1	1	1
l1	8	7	8	7
t1	0,5	0,3	0,3	0,3
w2	10	10	12	10
l2	10	10	12	10
t2	1	1	1	1,5

Table A-2 Dimensions of the supporting beams and mirrors for the torsional scanner prototypes.

APPENDIX B

MATERIAL PROPERTIES OF RENSHAPE SL5195

LIQUID MATERIAL		
MEASUREMENT	CONDITION	VALUE
Appearance	Clear	Amber
Density	@ 25°C (77°F)	1.16 g/cc
Viscosity	@ 28°C (82°F)	220 cps
Viscosity	@ 30°C (86°F)	180 cps
Penetration depth (Dp)		5.2 mils
Critical exposure (Ec)		13.1 mJ/cm^2
POST CURED MATERIAL		
MEASUREMENT	TEST METHOD	VALUE
		90-minute UV post-cure
Hardness, Shore D	ASTM D 2240	83
Flexural modulus	ASTM D 790	1,628 MPa
Flexural strength	ASTM D 790	49.3 MPa
Tensile modulus	ASTM D 638	2,090 MPa
Tensile strength	ASTM D 638	46.5MPa
Elongation at break	ASTM D 638	0,11
Impact strength, notched Izod	ASTM D 256	54 J/m
Heat deflection temperature	ASTM D 648 @ 66 PSI @ 264 PSI	47°C (117°F) 43°C (109°F)
Glass transition, Tg	DMA, E" peak	67 - 82°C
Coefficient of thermal expansion	TMA (T<Tg) TMA (T>Tg)	108 x 10^{-6}/°C 189 x 10^{-6}/°C
Thermal conductivity		0.182 W/m °K 4.33 x 10^{-4} cal/sec.cm.°C
Density		1.18g/cm^3

APPENDIX C

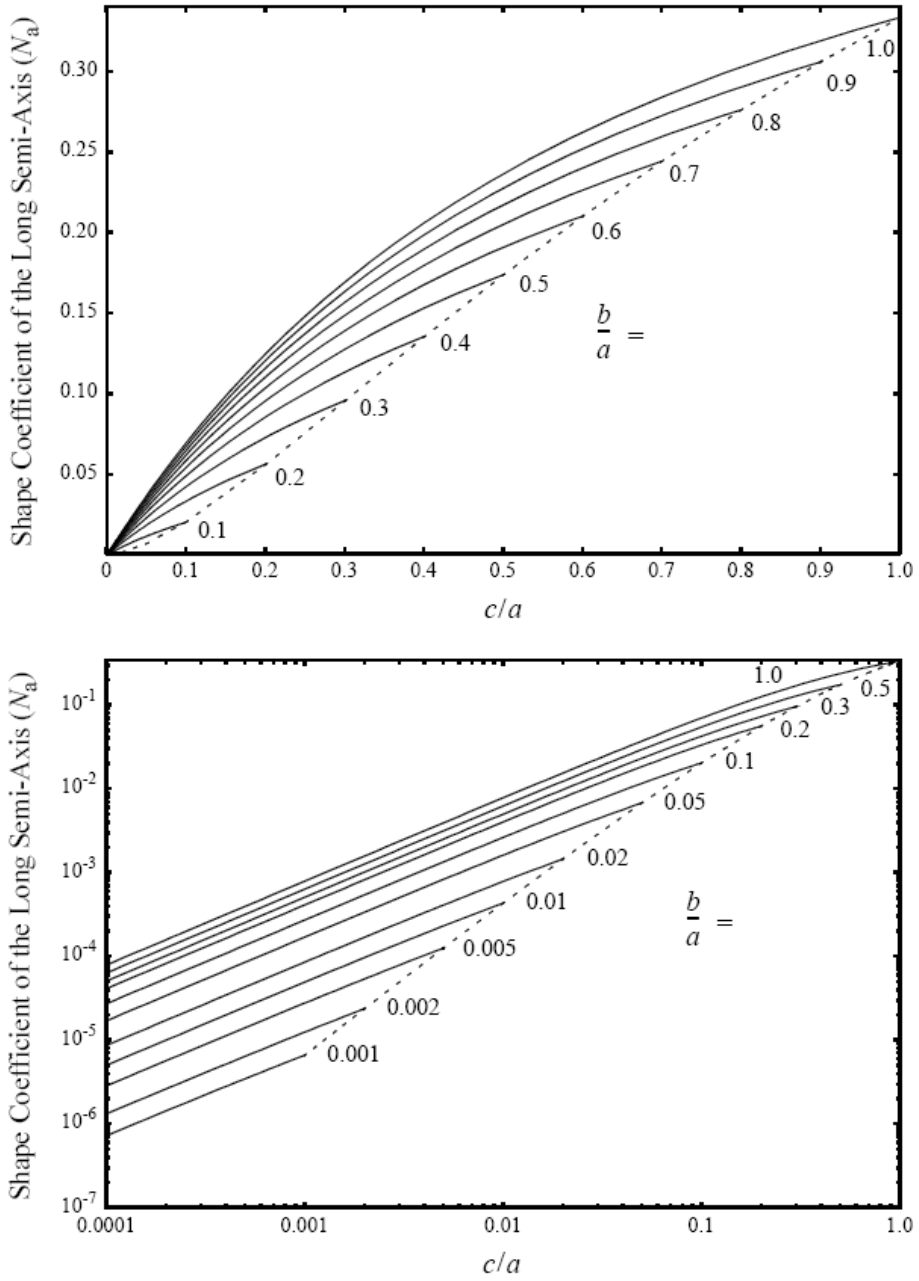

Table C-1 Shape coefficient of the general ellipsoid along the long axis N_a shown in a linear plot (up) and logarithmic plot (below) [19].

Appendix C

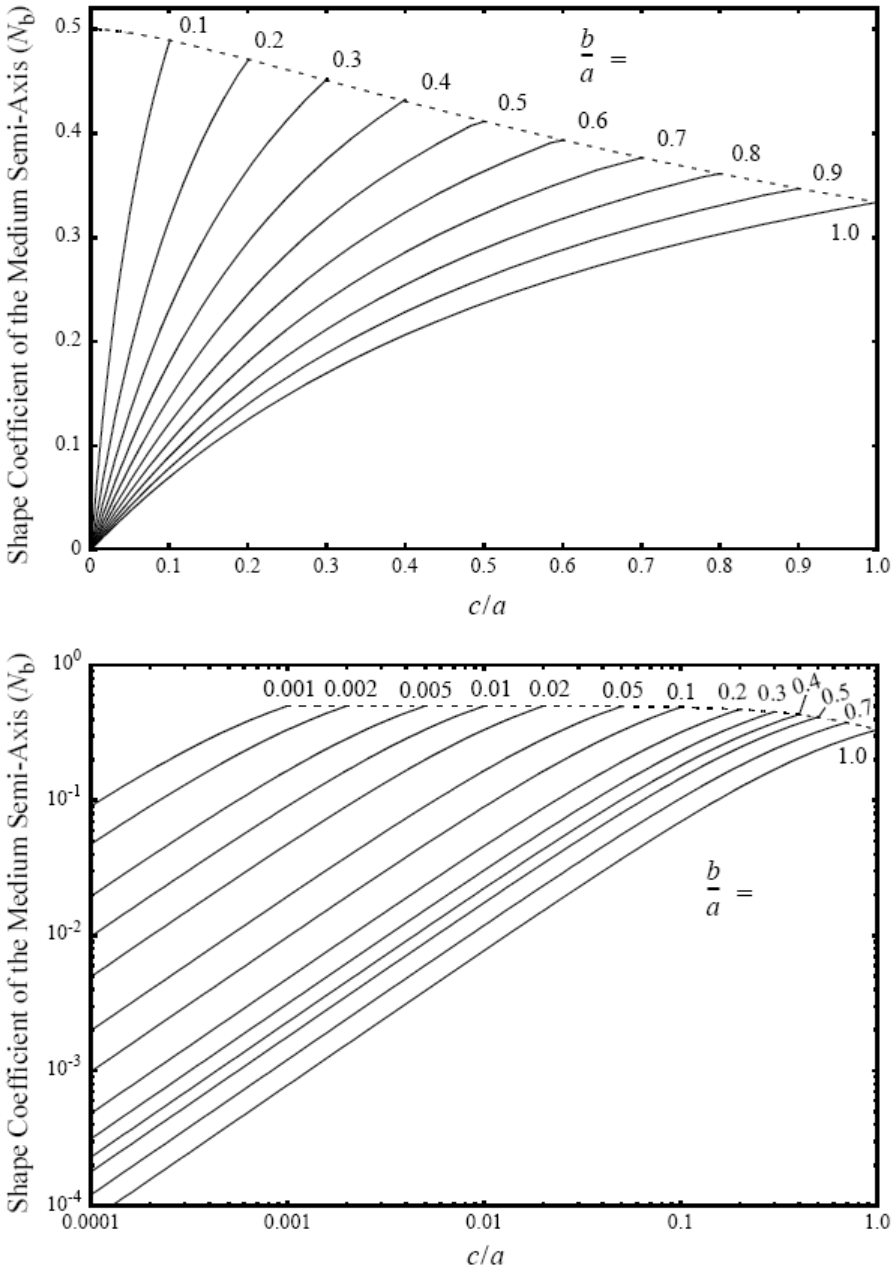

Table C-2 Shape coefficient of the general ellipsoid along the medium axis N_b shown in a linear plot (up) and logarithmic plot (below) [19].

Appendix C

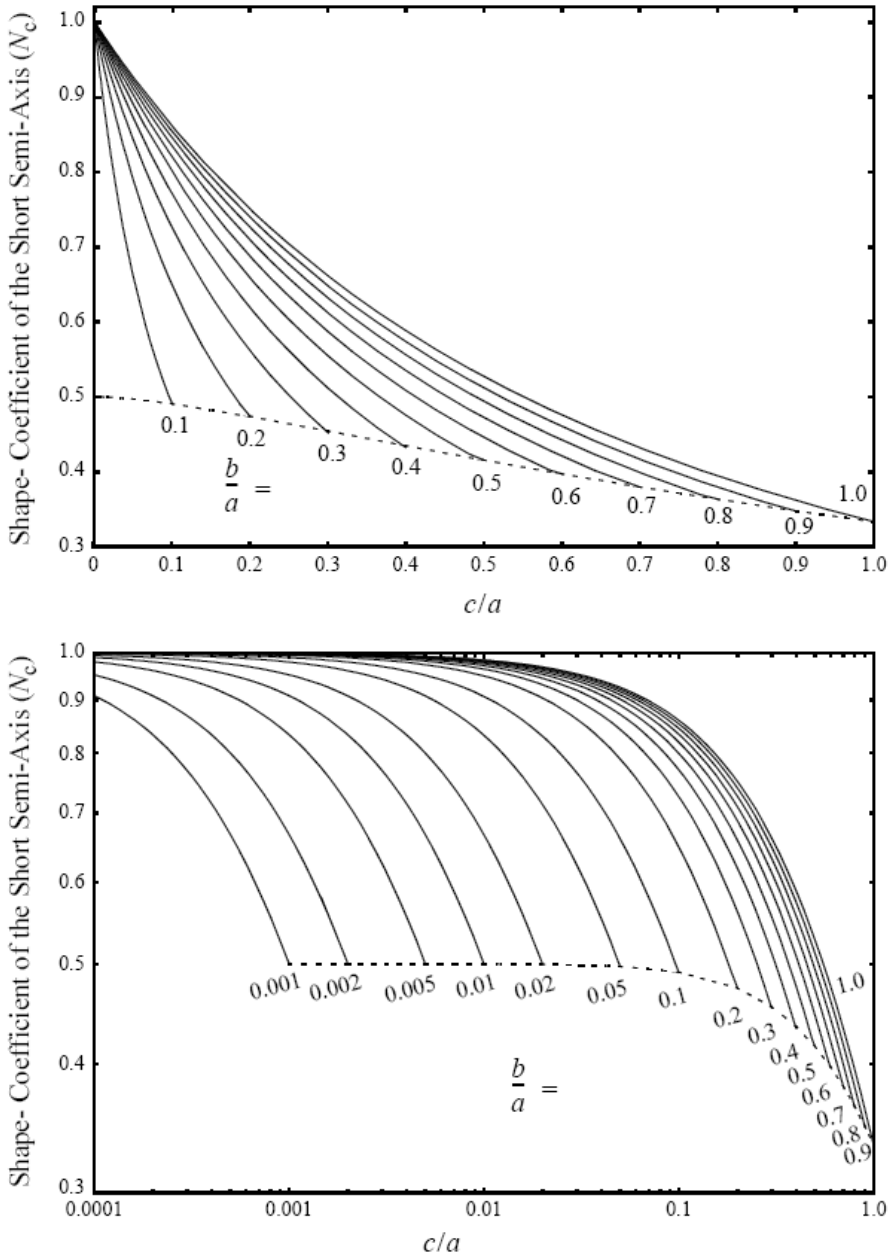

Table C-3 Shape coefficient of the general ellipsoid along the short axis N_c shown in a linear plot (up) and logarithmic plot (below) [19].

BIBLIOGRAPHY

[1] H. Urey, “Retinal Scanning Displays”, *Encyc. of Optical Engineering*, Marcel-Dekker, 2003.

[2] H. Urey, “MEMS Scanners for Display and Imaging Applications,” submitted to *Photonics East*, 2004.

[3] H. Urey, D.W. Wine, J. R. Lewis, “Scanner design and resolution tradeoffs for miniature scanning displays,” *SPIE Proc. of Conference on Flat Display Technology and Display Metrology*, vol. 3636, pp.60-68, 1999.

[4] H. Urey, D.W. Wine, J. R. Lewis, “MEMS Raster Correction Scanner for SXGA resolution Retinal Scanning Display,” *Proceedings of SPIE*, vol. 4985, pp.106-114, 2003.

[5] http://www.ipms.fraunhofer.de/publications/press/index.shtml?mirror050515.shtml

[6] Wolter, H. Schenk, E. Gaumont, H. Lakner**, “**MEMS microscanning mirror for barcode reading: from development to production,” *SPIE Proc. of MOEMS Display and Imaging Systems II*, vol. 5348, pp. 32-39, 2004.

[7] H. Schenk, U. Dauderstädt, P. Dürr, A. Gehner, A. Wolter, H. Lakner, “Light processing with electrostatically driven micro scanning mirrors and micro mirror arrays,” *SPIE Proc. of MOEMS Display and Imaging Systems II*, vol. , pp. , 2004.

[8] K. Roscher, H. Grätz, H. Schenk, A. Wolter, H. Lakner, “Low cost projection device with a 2D resonant microscanning mirror,” *SPIE Proc. of MOEMS Display and Imaging Systems II*, vol. 5348, pp. 22-31, 2004.

[9] R.A. Conant, P.M. Hagelin, U. Krishnamoorthy, O. Solgaard, K.Y. Lau, R.S. Muller, "A raster-scanning full-motion video display using polysilicon micromachined mirrors", *Proc. of the 1999 Int. Conf. on Solid-State Sensors and Actuators (Transducer ‘99)*, pp. 376-379, Sendai, Japan, June 7-10, 1999.

[10] J.H. Lee, Y. C. Ko, D.H. Kong, J.M. Kim, K. B. Lee, D. Y. Jeon, “ Design and fabrication of scanning mirror for laser display,” *Sensors and Actuators A*, vol. 96, p. 223–230, 2002.

[11] D.L. Dickensheets, G.S. Kino, “Silicon-micromachined scanning confocal optical microscope,” *Journal of Microelectromechanical Systems*, vol. 7, pp. 38-47, 1998.

[12] http://en.wikipedia.org/wiki/Barcode_reader

[13] R. C. Palmer, "The bar code book," Helmer Publishing Inc.,1995.

[14] C. Ataman, "Design, Modeling and Characterization of Electrostatically Actuated Microscanners," *M.S. thesis*, 2004.

[15] H.Y. Lin, W. Fang, "A rib-reinforced micro torsional mirror driven by electrostatic torque generators," *Sensors and Actuators A*, vol. 105, pp. 1-9, 2003.

[16] T.G. Bifano, J. Perreault, R.K. Mali, and M.N. Horenstein, "Microelectromechanical Deformable Mirrors," *IEEE Journal of Selected Topics in Quantum Electronics*, vol. 5, no. 1, pp. 83-89, 1999.

[17] S. Kwon, V. Milanovic, L.P. Lee, "A High Aspect Ratio 2D Gimbaled Microscanner with Large Static Rotation," *presented in IEEE/LEOS Optical MEMS 2002,* Lugano, Switzerland, Aug. 2002.

[18] D. Lee, U. Krishnamoorthy, K. Yu, O. Solgaard, "Single-crystalline silicon micromirrors actuated by self-aligned vertical electrostatic combdrives with piston-motion and rotation capability," *Sensors and Actuators A*, to be published.

[19] J. W. Judy, "Batch-fabricated ferromagnetic microactuators with silicon flexures," *PhD thesis*, 1996.

[20] J. J. Bernstein, P. Taylor, J. D. Brazzle, C. J. Corcoran, G. Kirkos, J. E. Odhner, A. Pareek, M. Waelti, M. Zai, "Electromagnetically Actuated Mirror Arrays for Use in 3-D Optical Switching Applications," *Journal of Microelectromechanical Systems*, vol. 13, no 3, pp. 526-535, 2004.

[21] B. Wagner, W. Benecke, "Microfabricated actuator with moving permanent magnet," *IEEE Proc.* (1991), pp.27-32.

[22] H. J. Cho, C. H. Ahn, "A bidirectional magnetic microactuator using electroplated permanent magnet arrays," *Journal of Microelectromechanical Systems*, vol. 11, no 1, pp. 78-84, 2002.

[23] J. W. Judy, R. S. Muller, H. H. Zappe, "Magnetic microactuation of polysilicon flexure structures," *Journal of Microelectromechanical Systems*, vol. 4, no 4, pp. 162-169, 1995.

[24] C. Liu, "Micromachined magnetic actuators using electroplated permalloy," *IEEE Transactions on Magnetics*, vol. 35, no. 3, pp 1976-1985, 1999.

Bibliography

[25] C. Liu, T. Tsao, G. Lee, J. T. S. Leu, Y. W. Yi, Y. Tai, C. Ho, "Out-of-plane magnetic actuators with electroplated permalloy for fluid dynamics control," *Sensors and Acuators*, vol 78, pp 190-197, 1999.

[26] S. Schweizer, S. Calmes, M. Laudon, Ph. Renaud, "Thermally actuated optical microscanner with large angle and low consumption", *Sensors and Actuators*, vol. 76, pp. 470-477, 1999.

[27] M. Sasaki, T. Yamaguchi, J. H. Song, K. Hane, M. Hara, and K. Hori, "Optical Scanner on a Three-Dimensional Microoptical Bench", *Journal of Lightwave Technology*, vol. 21, no. 3, pp. 602-608, March 2003.

[28] K.H. Chau, S. Dimitrijev, " Two-dimensional microscanner actuated by PZT thin film," *SPIE Proc. of Device and Process Technologies for MEMS and Microelectronics*, vol. 3892, pp. 133-140, October 1999.

[29] F. Filhol, E. Defaÿ, C. Divoux, C. Zinck and M-T. Delaye, "Piezoelectric micromirrors for fast optical scanning with large angular deflection," presented in *IEEE/LEOS International Conference on Optical MEMS and Their Applications*, Kagawa, Japan, 2004.

[30] H. Shenk, P. Dürr, T. Haase, D. Kunze, U. Sobe, H. Lakner, H. Kück, "Large deflection micromechanical scanning mirrors for linear scans and pattern generation," *Journal of Selected Topics in Quantum Electronics*, vol. 6, no. 5, pp.715-722 (2000).

[31] S. Timoshenko, *Strength of Materials,* New York: Van Nostrand, 1955.

[32] Warren C. Young, Richard G. Budynas, *Roark's Formulas for Stress and Strain,* New York: McGraw-Hill, 2002.

[33] H. Urey, C. Kan, W. O. Davis, "Vibration mode frequency formulae for micromechanical scanners," *Journal of Micromechanics and Microengineering,* vol. 15, pp. 1713-1721, 2005.

[34] Stephen D. Senturia, *Microsystem Design*, Boston: Kluwer Academic Publishers, 2001.

[35] D. K. Cheng, *Fundamentals of Engineering Electromagnetics,* Massachusetts, Addison-Wesley Publishing, 1993.

[36] N. Spaldin, *Magnetic Materials: fundamentals and device applications,* Cambridge, Cambridge University Press, 2003.

[37] R. C. O'Handley, *Modern Magnetic Materials Principle and Applications,* New York, John Wiley & Sons, 2000.

[38] S. O. Kasap, *Principles of Electronic Materials and Devices,* New York, McGraw-Hill, 2002.

[39] K. Vollmers, R. Anderson, B. J. Nelson, J. Pepin, "High Strength Rare Earth-Iron-Boron Printed Magnets Used In A Long Throw-High Force Electromagnetic Actuator With Microfabricated Coils," *Proc. IEEE MEMS 2003*, Kyoto, Japan, pp. 60-63.

[40] L.K. Lagorce and M.G. Allen, "Magnetic and Mechanical Properties of Micromachined Strontium Ferrite/Polyimide Composites, " *J. Microelectromechanical* Sys., 6(4), pp. 307-3 12, 1997.

[41] L.K. Lagorce. 0.Brand and M.G. Allen. "Magnetic Microactuators Based on Polymer Magnets." *J. Microelectromechanical* Sys.. 8(I), pp. 2-9, 1969.

[42] C. H. Ahn, Y. J. Kim, M. G. Allen, "A planar variable reluctance magnetic micromotor with fully integrated stator and wrapped coils," *IEEE Micro Electro Mechanical Systems Workshop Proceedings (MEMS '93),* IEEE Catalog #93CH3265-6, Fort Lauderdale, FL (February 7-10, 1993), pp. 1-6.

[43] W. P. Taylor, M. Schneider, H. Baltes, M. G. Allen, "Electroplated soft magnetic materials for microsensors and microactuators," *1997 International Conference on Solid-State Sensors and Actuators (Transducers '97),* Chicago, June 16-19, pp. 1445-1448, 1997.

[44] J. M. Quemper, S. Nicolas, J. P. Gilles, J. P. Grandchamp, A. Bosseboeuf, T. Bourouina, E. Dufour-Gergam, "Permalloy electroplating through photoresist molds," *Sensors and Actuators*, vol. 74, 1999.

VITA

Olgaç Ergeneman was born in Ankara, Turkey in 1981. He completed the high school in TED Ankara College in 1999. He received his B. Sc. degree from the Department of Electrical and Electronics Engineering, Middle East Technical University, Ankara in 2003. Same year, he joined Optical Microsystems Laboratory (OML) of Koç University, Department of Electrical Engineering as an M.Sc candidate. Olgaç Ergeneman is a student member of SPIE and IEEE.